Approaches to improving pulsed EDMR spectroscopy in organic electronic devices using adiabatic pulses

Author:
Alhazani, Tamader

Publication Date:
2021

DOI:
https://doi.org/10.26190/unsworks/1972

License:
https://creativecommons.org/licenses/by/4.0/
Link to license to see what you are allowed to do with this resource.

The University of New South Wales
School of Physics
Faculty of Science

Approaches to improving pulsed EDMR spectroscopy in organic electronic devices using adiabatic pulses

Tamader Alhazani

Supervisor:

Professor Dane McCamey

A thesis submitted in fulfilment of the requirements

for the degree of Doctor of Philosophy

(September) 2021

Originality Statement

I hereby declare that this submission is my own work and to the best of my knowledge it contains no materials previously published or written by another person, or substantial proportions of material which have been accepted for the award of any other degree or diploma at UNSW or any other educational institution, except where due acknowledgement is made in the thesis. Any contribution made to the research by others, with whom I have worked at UNSW or elsewhere, is explicitly acknowledged in the thesis. I also declare that the intellectual content of this thesis is the product of my own work, except to the extent that assistance from others in the project's design and conception or in style, presentation and linguistic expression is acknowledged.

Signed: ....

Date:..........03/10/2021................

INCLUSION OF PUBLICATIONS STATEMENT

> UNSW is supportive of candidates publishing their research results during their candidature as detailed in the UNSW Thesis Examination Procedure.
>
> **Publications can be used in their thesis in lieu of a Chapter if:**
> - The student contributed greater than 50% of the content in the publication and is the "primary author", ie. the student was responsible primarily for the planning, execution and preparation of the work for publication
> - The student has approval to include the publication in their thesis in lieu of a Chapter from their supervisor and Postgraduate Coordinator.
> - The publication is not subject to any obligations or contractual agreements with a third party that would constrain its inclusion in the thesis

Please indicate whether this thesis contains published material or not.

☒ *This thesis contains no publications, either published or submitted for publication (if this box is checked, you may delete all the material on page 2)*

☐ *Some of the work described in this thesis has been published and it has been documented in the relevant Chapters with acknowledgement (if this box is checked, you may delete all the material on page 2)*

☐ *This thesis has publications (either published or submitted for publication) incorporated into it in lieu of a chapter and the details are presented below*

CANDIDATE'S DECLARATION

I declare that:

- I have complied with the Thesis Examination Procedure

- where I have used a publication in lieu of a Chapter, the listed publication(s) below meet(s) the requirements to be included in the thesis.

Name Tamader Alhazani	Signature	Date (3/10/2021)

Postgraduate Coordinator's Declaration (to be filled in where publications are used in lieu of Chapters)

I declare that:

- the information below is accurate
- where listed publication(s) have been used in lieu of Chapter(s), their use complies with the Thesis Examination Procedure
- the minimum requirements for the format of the thesis have been met.

PGC's Name	PGC's Signature	Date (dd/mm/yy)

For each publication incorporated into the thesis in lieu of a Chapter, provide all of the requested details and signatures required

Details of publication #1:						
Full title:						
Authors:						
Journal or book name:						
Volume/page numbers:						
Date accepted/ published:						
Status	*Published*		*Accepted and In press*		*In progress (submitted)*	
The Candidate's Contribution to the Work Insert text describing how the candidate has contributed to the work						
Location of the work in the thesis and/or how the work is incorporated in the thesis: Insert text						
Primary Supervisor's Declaration I declare that: • the information above is accurate • this has been discussed with the PGC and it is agreed that this publication can be included in this thesis in lieu of a Chapter • All of the co-authors of the publication have reviewed the above information and have agreed to its veracity by signing a 'Co-Author Authorisation' form.						
Supervisor's name		*Supervisor's signature*		*Date (dd/mm/yy)*		

Details of publication #2:						
Full title:						
Authors:						
Journal or book name:						
Volume/page numbers:						
Date accepted/ published:						
Status	*Published*		*Accepted and In press*		*In progress (submitted)*	
The Candidate's Contribution to the Work Insert text describing how the candidate has contributed to the work						
Location of the work in the thesis and/or how the work is incorporated in the thesis: Insert text						
Primary Supervisor's Declaration I declare that: • the information above is accurate • this has been discussed with the PGC and it is agreed that this publication can be included in this thesis in lieu of a Chapter • All of the co-authors of the publication have reviewed the above information and have agreed to its veracity by signing a 'Co-Author Authorisation' form.						
Supervisor's name		*Supervisor's signature*		*Date (dd/mm/yy)*		

Add further boxes if required. You may delete any boxes not used

Thesis/Dissertation Sheet

Surname/Family Name	:	**Tamader Alhazani**
Given Name/s	:	**Tammy**
Abbreviation for degree as give in the University calendar	:	**PhD**
Faculty	:	**Faculty of Science**
School	:	**School of Physics**
Thesis Title	:	**Improving pulsed EDMR spectroscopy in organic electronic devices using adiabatic pulses**

Abstract 350 words maximum: (PLEASE TYPE)

Exploiting organic electronic material in optoelectronic devices requires us to understand the generation, mobility, and recombination of charge carriers. In these materials, the quantum mechanical property of spin has a considerable effect on these processes. Due to weak spin-orbit coupling, spin is a good quantum number, and spin-dependent processes play a significant role in conductivity and recombination. Consequently, spin-based probes such as electron spin resonance are effective ways to understand the underlying electronic properties in these materials. The long-lived spin states also point toward applications in sensing, using either magnetoresistive or resonant effects to provide new functionality. A useful technique for this is electrical detection of magnetic resonance (EDMR), which uses electron spin resonance for spin manipulation and conductivity measurements to detect the resulting changes in transport properties. For example, the change in the current through an organic light-emitting diode (OLED) due to EDMR allows us to determine spin lifetimes and spin-dependent recombination rates of polaron pairs. A number of proposals have been shown that OLEDs can be used as magnetometers via phase-sensitive electron spin resonance approaches. Owing to the disorder inherent in these materials, a challenge applying these techniques to organic devices is the inhomogeneous broadening of polaron spin resonances due to interactions with nuclear spins in the organic materials. Previous work shows that adiabatic pulse schemes can improve both fidelity and sensitivity of EDMR in organic devices under ideal conditions. Here, I extend these results to include simulations with realistic spin lifetimes and recombination rates. I experimentally determine the spin and carrier lifetimes for MEH-PPV-based devices and use these parameters to model the impact of adiabatic pulse schemes using these parameters in a stochastic Liouville framework, expanding on previous work by explicitly including Redfield terms. I show theoretically that chirp pulses increase the fidelity of operation in a Hahn echo sequence compared to square pulses, and that the trajectories of spin pairs under adiabatic excitation schemes has a more complex impact on the resulting fidelity than two independent spins. This work is important for applications which exploit the properties of organic semiconductors such as spin-based sensing.

FOR OFFICE USE ONLY   Date of completion of requirements for Award:

Abstract

Exploiting organic electronic material in optoelectronic devices requires us to understand the generation, mobility, and recombination of charge carriers. In these materials, the quantum mechanical property of spin has a considerable effect on these processes. Due to weak spin-orbit coupling, spin is a good quantum number, and spin-dependent processes play a significant role in conductivity and recombination. Consequently, spin-based probes such as electron spin resonance are effective ways to understand the underlying electronic properties in these materials. The long-lived spin states also point toward applications in sensing, using either magnetoresistive or resonant effects to provide new functionality. A useful technique for this is electrical detection of magnetic resonance (EDMR), which uses electron spin resonance for spin manipulation and conductivity measurements to detect the resulting changes in transport properties. For example, the change in the current through an organic light-emitting diode (OLED) due to EDMR allows us to determine spin lifetimes and spin-dependent recombination rates of polaron pairs. A number of proposals have been shown that OLEDs can be used as magnetometers via phase-sensitive electron spin resonance approaches. Owing to the disorder inherent in these materials, a challenge applying these techniques to organic devices is the inhomogeneous broadening of polaron spin resonances due to interactions with nuclear spins in the organic materials. Previous work shows that adiabatic pulse schemes can improve both fidelity and sensitivity of EDMR in organic devices under ideal conditions. Here, I extend these results to include simulations with realistic spin lifetimes and recombination rates. I experimentally determine the spin and carrier lifetimes for MEH-PPV-based devices and use these parameters to model the impact of adiabatic pulse schemes using these parameters in a stochastic Liouville framework, expanding on previous work by explicitly including Redfield terms. I show theoretically that chirp pulses increase the fidelity of operation in a Hahn echo sequence compared to square pulses, and that the trajectories of spin pairs under adiabatic excitation schemes have a more complex impact on the resulting fidelity than two independent spins. This work is important for applications which exploit the properties of organic semiconductors such as spin-based sensing.

Acknowledgement

During my PhD, I had learned a wide range of new experimental techniques, related to device design, fabrication, characterization, optimization, and measurements. I also designed and built a new measurement apparatus that are crucial for the EDMR experiment development.

At first, it is my pleasure to be supervised by Prof. Dane McCamey, so I would like to thank him for allowing me to have a great experience during my research and supporting me with his great knowledge and advice all the time.

In addition to my advisor, I would like to thank McCamey group for being helpful and supportive all the time. Especially, I would like to thank Joanna and Amir for their assistance during our collaboration work and for the effective comments that help me to expand my research field. Triet, my colleague, thank you for your time and thank you for being a positive and fun friend during our discussion on our projects or life in general.

A special thanks to Dr. Richard Newbury, the professional officer Gary Keenan, and the laboratory assistant Neil Lawrence for providing the necessary assistance that supports my research, and for being around when I need you.

Great thanks to my parents, sisters, and brothers for encouraging and supporting me all the time. Thanks from my heart to my husband for being with me during my PhD and for supporting me, thank you for everything. My children, Hams, Rand, Ali, and Omar thank you, my angels, for your love, happiness, and patient all the time. Thank you for providing me happiness, strength, and positive energy when I was about to give up.

And finally, a special thanks to my country for giving me this opportunity and providing me with everything I need to achieve my aim and complete my PhD studying.

Table of Contents

List of Figures

List of Tables

Abbreviations

EDMR   Electrically Detected Magnetic Resonance

EPR   Electron Paramagnetic Resonance

ESR   Electron Spin Resonance

ITO   Indium-Tin Oxide

MEH-PPV   Poly[2-methoxy-5-(2-ethylhexyloxy)-1,4-phenylenevinylene]

OLED   Organic light-emitting diode

PEDOT   Poly(3,4-ethylenedioxythiophene)

PP   Polaron pair

PSS   Poly(styrene-sulfonate)

Chapter 1

Introduction

Organic semiconductors have become an important and promising material with which to develop a variety of optoelectronic technologies, in particular organic light-emitting diodes (OLEDs) [1] and organic solar cells [2]. The critical need to develop organic solar cells, with low cost, flexibility, and environmentally friendly, is fundamentally related to producing green energy [3]. In addition, flexibility, lightweight, efficiency and lifetimes are some of the driving factors in the increasing use of organic device over devices based on inorganic materials [4, 5]. However, organic devices face some challenges related to their lower efficiency and stability issues. For example, organic solar cells have demonstrated 17.3% [3] as a maximum efficiency while the inorganic ones 46% [6]. Furthermore, instability and fast degradation is the main concern in organic devices [7, 8]. Therefore, most researchers in the field have been focused on solving these issues and investigating spin processes to understand underlying physics in organic materials. However, the development of organic devices has some limitations due to the experimental difficulties when investigating spin phenomena, spin randomization, and the impact of magnetic field effects [9].

Investigations on organic electronic materials have shown that weak spin-orbit interactions occur in these materials which leads to spin-conservation and has an influence on many electronic processes such as generation, charge carrier recombination and transport. This thesis is based on the premise that explicitly understanding these properties by using spin-based probes is important for improving device efficiency and performance, and thus developed new technological applications [4]. One of the most remarkable development applications is using OLEDs for magnetic field sensing due to the sensitivity of spin-dependent processes to small changes in the magnetic field in organic materials. Ref. [10] demonstrated the first organic spintronic device achieved 30% magnetoresistance at room temperature. Ref. [11] presented the organic magnetic resonance magnetometer, which allowed the accurate measurement to the small length of intermediate fields. The utilization of a suitable technique of influence on OLED, such as pulsed electrically detected magnetic resonance, would lead to the spin coherence spectroscopy [11]. Therefore, OLED-based sensors provide a new conception for accurate magnetometry measurement.

1.1 Quantum systems spin and control

Quantum mechanics is an important concept for describing our understanding of nature. In general, quantum mechanics is necessary to describe the structure, properties, and behavior of atoms and molecules such as intrinsic randomness, interference phenomena, and entanglement between physical systems, which are all common and classical mechanics failed with [12].

Controlling quantum mechanical system is by using the interaction between a quantum system and a classical control field to allow its dynamics to reach the required result [13, 14]. In organic electronics, the quantum mechanical property of spin has an effect on many processes such as charge carrier recombination and transport owing to weak spin-orbit coupling in these materials. Therefore, implicitly understanding of the electronic properties of these materials by using spin-based probes leads to develop magnetoresistance and sensor applications and new technological applications [4, 15, 16].

In order to analyze a quantum system, a spin Hamiltonian, which describes both the time-independent environmental interactions and the interaction between the electron spins and the driving field, should be determined [16, 17]. Furthermore, the concept of the Hamiltonian is used for describing the spectroscopy of electron spin resonance (ESR). ESR spectroscopy is a magnetic resonance technique, and its fundamental principle is absorption of the electromagnetic radiation by electrons in the presence of an external magnetic field [18, 19, 20, 21]. Although there are many ESR modalities (continuous wave ESR (cw-ESR), electron nuclear double resonance (ENDOR), and electron spin echo envelope modulation (ESEEM), etc), ESR measurements have some limitations due to sensitivity to charge n polarization and ESR spectroscopy is described by long electron interactions [18]. To overcome these limitations, electrical detection of magnetic resonance (EDMR) and optical detection of magnetic resonance (ODMR) have been used [4].

1.2. Spins in organic systems

Understanding the processes occurring inside organic materials such as recombination, dissociation, spin relaxation, and spin decoherence is needed to exploit organic materials for developing new technologies especially optoelectronic devices [5]. Within appropriate properties such as weak spin-orbit coupling, long coherence times, and large magnetic field effects at room temperature, therefore, spin manipulation is important to understand the underlying electronic properties in these materials [15, 16].

Defining spin dependent and independent processes in organic devices would be more possible with spin control [5]. In order to investigate spin dependent transitions which are affected by static magnetic fields and magnetic resonance, the observation of spins and their interaction is required. Electron paramagnetic resonance (EPR) or ESR and nuclear magnetic resonance (NMR) have been used to

observe spin-spin and spin-environment interactions, and spin relaxation. However, these methods have some limitations such as the measurements are sensitive to change in polarization, and limited spins detection due to little information about electronic transitions between paramagnetic levels, which caused by magnetic resonance spectroscopy. Therefore, using electrical detection of magnetic resonance (EDMR) and optical detection of magnetic resonance (ODMR) is required to reduce EPR and NMR limitations especially given the enhanced sensitivity of EDMR and ODMR which allows a very small sample to be detected [11].

In 1959 [22, 23], the first ODMR experiments were performed on chromium ions in an aluminum oxide host matrix. The first EDMR was demonstrated in 1966 by both Maxwell and Honig and Schmidt and Solomon [24, 25]. Both EDMR and ODMR manipulate spin with magnetic resonance, but EDMR is measuring via sample conductivity while ODMR is measuring via spin-controlled radiative emission or absorption, as opposed to the inductive detection usually employed in ESR. In addition to the detection of single spins, EDMR and ODMR allow the influence of spin on a range of rates to be measured. In contrast of EPR, EDMR and ODMR meet the requirements of conditional experiments with even high temperature or low magnetic field due to the dependence of spin selection principles. Since most of the EDMR and ODMR are achieved by continuous wave (cw) experiments which applied microwave radiation within magnetic field which reveal limited data such as Landé g factors, coupling, and electron lifetime, thus developing the coherent, pulsed EDMR and ODMR (pEDMR/pODMR) is needed [4]. Organic materials dynamics information such as recombination, dissociation, spin relaxation times, and spin coherence times can be determined by using pulsed electrically and optically detected magnetic resonance (pEDMR and pODMR) [5]. The first pEDMR was observed in 2002, while pODMR and pEPR have been used since 1970s [4]. These methods are strongly used in short pulsed excitation resonance duration which lead to spin coherent manipulation to be investigated, and during that charge carrier spins state change and then the observation of the current enhancement or extinguish is recorded [4, 26]. The system returns back to its steady state, which is before applying any pulses and with constant current, at longer time scales that include spin relaxation time, charge carrier lifetimes, and detection system constants time [26].Therefore, it is clear that applying pEDMR/pODMR to organic materials has fundamental benefits to access to spin dynamic information, thus new technologies and discoveries can exist [4, 5, 26].

1.3. Organic devices

Organic materials have been used to develop technology, which is now widespread, and found in applications such as mobile phone, digital cameras, TVs and computers screens. The benefit of using organic over inorganic materials in many applications is due to features such as flexibility, foldability, low material cost, low density and potentially high throughput and low-cost processing. Considering

organic materials, especially organic semiconductors for developing optoelectronic technologies is appropriate because of the interest properties such as weak spin-orbit coupling, long spin coherence times and large magnetic field effects at room temperature [5].

Since organic semiconductors have very weak spin-orbit interaction, the consequence would be long spin coherence times which could be increased by replacing the hydrogen with deuterium in order to extinguish the strong interaction between free charge carriers and the hydrogen spins on the carbon. Integrating long spin coherence times with large magnetic field effects would produce favorable semiconductor that can be used to improve quantum technologies due to the effective of magnetic field on the device conductivity and luminosity. Moreover, organic spin valves, which transfer spins to certain direction, have been influenced by magnetic field. It should be noted that spin valves measurement is one of the most used processes for describing organic systems [5].

1.4. Aim of Thesis

The aim of this thesis is to investigate the application of adiabatic pulse schemes to improve both the sensitivity and fidelity of electrically detected magnetic resonance in organic devices [17]. Whilst the application of these schemes (which have traditionally been limited to nuclear magnetic resonance (NMR)) is emerging in electron spin resonance, their application to electrically detected spin resonance has been limited. We will report on the fidelity improvements which can be gained using these techniques in pulse schemes applied to systems with intrinsic disorder, and in particular benchmark the improvement they provide for phase sensitive organic magnetic field sensors with realistic dephasing mechanisms and carrier lifetimes.

1.5. Thesis outline

This thesis is structured as follows:

Chapter 2 discusses the theoretical basics of the quantum mechanics system, spin processes in organic semiconductors, and the coherent and incoherent spin motion resulting from electron spin resonance. Also demonstrates EDMR and the historical development of p-EDMR method, and theory of Magnetic field sensing.

Chapter 3 discusses the development of organic device fabrication processes, device characterization, device optimization, and stability measurements.

Chapter 4 demonstrates p-EDMR experimental results on MEH-PPV diodes, which are undertaken to provide parameters for modeling in chapter 5.

Chapter 5 describes theoretical investigations of magnetic resonance on OLED with adiabatic pulses, pulse sequences and predicted improvements.

Chapter 6 provides conclusions and suggestions for future work.

Chapter 2. Theory and Background

2.1 Quantum systems, spin and control

Quantum mechanics is a fundamental and important theory to understand and explain the properties and the behavior of solids, atoms, and elementary particles. With many applications such as conductivity, magnetism, semiconductors, lasers, light emitting diodes and furthermore in many natural, biological and physical phenomena, quantum mechanics is central to our understanding of the physical world. [12].

In organic electronics, the quantum mechanical property of spin has an effect on many processes such as charge carrier recombination, generation, and mobility owing to weak spin-orbit coupling, which results in Pauli blockade that affects conductivity and long coherence times that affects recombination these materials. Therefore, utilization of spin-based probes in order to understand the underlying of the electronic properties of these materials is critical if we are to utilize spin to develop magnetoresistance and sensor applications and new technological applications [15, 16].

The conception of the spin Hamiltonian is critical for describing ESR spectroscopy. A system with magnetic interactions and lowest electronic state in the basic form of Schrödinger wave equation can be described as:

$$\widehat{H}_s \psi_s \tag{2.1}$$

where $\widehat{H}_s$ the spin Hamiltonian, ψ_s the spin wavefunction and E is the energy of the state s.

An isolated system with only Zeeman interaction and without hyperfine interactions can be described as

$$\widehat{H}_s = \mu_B B \cdot g \cdot S \tag{2.2}$$

with solution

$$hv = \sqrt{g_x^2 l_x^2 + g_y^2 l_y^2 + g_z^2 l_z^2} \mu_B B \tag{2.3}$$

where h is Planck's constant, v is the frequency of the radiation, g is Landé g-factor, is spin operator, μ_B is a physical constant called the Bohr magneton and B is the applied magnetic field, and

$$g \cdot S = g_x l_x + g_y l_y + g_z l_z \;,$$

A more detailed description of ESR and different forms of the relevant spin Hamiltonian will be explained in next chapters [20, 21].

2.1.1 Spin and the Spin Hamiltonian

2.1.1.1 Spin-dependent processes in organic semiconductors:

The bulk properties of organic semiconductors such as photoconductivity, photo- and electro-luminescence and photo-absorption are influenced by spin dependent transitions [27, 28, 29]. These transitions also underly magnetoresistance [30] and magnetoluminescence effects in organic materials [31]. Although the physical causes for these phenomena are different, there is significant overlap between the theoretical models that describe them.

2.1.1.2 Exciton generation:

The formation of an exciton a strongly coupled electron-hole pair [5], is a significant spin dependent process in organic semiconductors. The generation of the exciton takes place following the collision of positive and negative charge carries. The exciton decay, which proceeds via radiative recombination, generates light in OLEDs. The exciton, which formed from two fermions (electron and hole) with spin s=1/2, is a boson with s=1 and can exist in one singlet state and three triplet states [4].
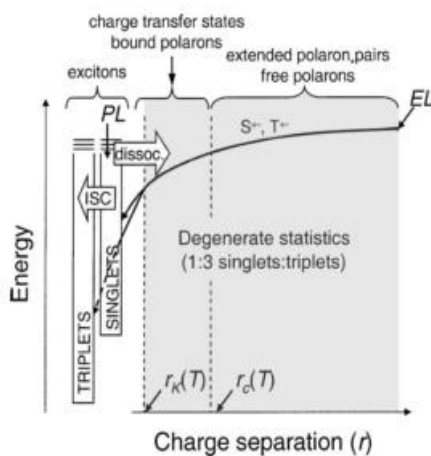
Figure 2.1: Binding energy of electrons and holes as a function of spatial separation. Figure is reproduced from [32]. Reprinted figure with permission from [M. Segal, M. A. Baldo, R. J. Holmes, S. R. Forrest, & Z. G. Soos,"Excitonic singlet-triplet ratios in molecular and polymeric organic materials", Physical Review B, 075211 (2003)] Copyright (2003) by the American Physical Society.

Figure 2.1 demonstrates the mechanism of exciton formation using the charge carrier pair's binding energy dependence on the spatial separation distance. The whole formation process includes several steps involving different interactions at each of the stages. First, when the separation distances are large,

the two spin states of polarons (charge carriers) are degenerate. However, as the separation decreases, Coulomb attraction becomes relevant and affects the polarons, thus bringing them closer to each other [4, 32]. During this stage, the polarons are bonding coulombically leading to the formation of a charge transfer state which leads to the population of a molecular excitation. The spin interaction is still negligible since it is weaker than the Coulomb energy. When the separation distance reaches a non-spin dependent Coulomb attraction the exchange interaction becomes much stronger leading to the formation of the strongly exchange-coupled singlet and triplet states of the exciton. Because of spin conservation rule, the transition from strong Coulomb coupled to strong exchange coupled exciton determines the spin multiplicity of the exciton. Therefore, the spin dynamics in this stage is critical to define the recombination type (radiative or nonradiative) which ultimately occurs [4, 32].

2.1.1.3 Spin Hamiltonian:

In general, the spin Hamiltonian can describe both the time-independent environmental interactions and the interaction between the electron spins and any applied driving field. It can be written as:

$$\widehat{H}(t) = \widehat{H}_0 + \widehat{H}_1(t) \tag{2.4}$$

where $\widehat{H}_0$ is a static component, $\widehat{H}_1(t)$ is a dynamic component, with often given by

$$\widehat{H}_1(t) = \sum_i \mu_B g_e \hat{S}_i . B_1(t) \tag{2.5}$$

Here, μ_B is the Bohr magneton, g_e is the electron Landé g-factor, $\widehat{S}$ is the Pauli operator for a spin-½ particle, and $B_1(t)$ is a time dependent magnetic field [5, 17].

In order to describe the behavior and the interaction of systems of spin-½ particles, it would be necessary to use the following generalized spin Hamiltonian which describes the energy structure and spin-spin couplings in the system. It has terms that include description of: individual spin-pair action, interaction between two spins pairs, and interaction with any other spins surrounding the pair [4, 5, 17, 33, 34].

$$\widehat{H}_0 = \widehat{H}_{Zeeman} + \widehat{H}_{exchange} + \widehat{H}_{hyperfine} + \widehat{H}_{dipolar} + \widehat{H}_{orbit} \tag{2.6}$$

2.1.1.4 Zeeman Interaction

The Zeeman Hamiltonian describes the interactions between a spin and an applied magnetic field. It can be written as:

$$\hat{H}_{Zeeman} = \mu_B g_e \hat{S}_i . B_0 \tag{2.7}$$

where μ_B is the Bohr magneton, g_e the electron g-factor, $\hat{S}$ the Pauli operator for a spin ½ particle, and B_0 the static magnetic field.

The Zeeman Hamiltonian can be simplified into a term corresponding to the Pauli spinors z_i of the spin i due to the B_0 field in the z-direction. In the experiment, Zeeman expression can be modified in order to control the whole Hamiltonian contributions [4, 17, 33, 34].

2.1.1.5 Exchange Interaction

The exchange coupling between the two spins within the pair is due to the Pauli principle, and it is in general anisotropic.

$$\hat{H}_{exchange} = -J\hat{S}_a . \hat{S}_b \tag{2.8}$$

where J is the exchange integral between the two spin pair wave-functions [4, 33, 34, 35].

If $J \gg (g_a - g_b)\mu_B B_0$, then the spin-pairs become strongly coupled and the rate of spin-dependent transitions cannot be influence by either magnetic resonance or strong magnetic fields. On the other hand, with low J, the spin-dependent rates become constant. However, if $J \approx (g_a - g_b)\mu_B B_0$, then magnetic field and polarization strongly influence the rate of spin-dependent [4].

2.1.1.6 Hyperfine Interaction

The hyperfine interaction describes the interactions between an electron spin and a nuclear spin. It can be written as:

$$\hat{H}_{hyperfine} = \hat{H}_{isoHF} + \hat{H}_{anisoHF} \tag{2.9}$$

where $\hat{H}_{isoHF}$ is the isotropic hyperfine interaction, which takes the form:

$$\hat{H}_{isoHF} = \sum_{j \in \{a,b\}} \sum_{i=1}^{n} A_{ij} \hat{S}_j . \hat{I}_i \tag{2.10}$$

with

$$A_{ij} = \frac{2\mu_0}{3\hbar^2} g_j g_i \mu_B \mu_N \mid \Psi_j(r_i) \mid^2 \tag{2.11}$$

Here, $\hat{I}_i$ is the nuclear spin operator of the ith nucleus (if the electron is interacting with an ensemble of nuclear spins), μ_0 the vacuum permeability, μ_N the nuclear magneton, and $|\Psi_j(r_i)|^2$ the probability of finding pair partner j at the position r_i of the ith nuclear r_i.

And $\hat{H}_{anisoHF}$ is the anisotropic hyperfine interaction, which describes the dipole interaction between electrons and nuclei. It can be written as:

$$\hat{H}_{anisoHF} = \sum_{j\in\{a,b\}} \sum_{i=1}^{n} \hat{S}_j^\dagger \tilde{D} \hat{I}_i \tag{2.12}$$

$$(\tilde{D})_{kl} = \frac{g_j g_i \mu_0 \mu_B \mu_N}{4\Pi r^5 \hbar^2} (r^2 \delta_{kl} - 3r_k r_l) \tag{2.13}$$

The anisotropic hyperfine interaction has a strong effect on spin relaxation, and thus spin mixing and magnetoresistance [4, 17].

2.1.1.7 Dipolar Interaction

Dipolar interaction-induced zero- field splitting:

From the hyperfine interaction between electron and nuclear spins previous equations, using zero-field splitting can describe the intrapair dipolar interaction as:

$$\hat{H}_{dipolar} = \hat{S}_a^\dagger \tilde{D}_d \hat{S}_b \tag{2.14}$$

where $\tilde{D}_d$ is zero-field splitting matrix form as:

$$(\tilde{D}_d)_{ij} = \frac{g_a g_b \mu_0 \mu_B}{4\Pi r^5 \hbar^2} (r^2 \delta_{ij} - 3r_i r_j) \tag{2.15}$$

Dipolar interactions depend on the pair size extremely, and compared to the hyperfine coupling for instance, in distant pairs is usually very weak [4, 5, 17].

2.1.1.8 Spin-Orbit Coupling

Zero-Field Splitting and Spin-Orbit Coupling:

Dipolar coupling interaction between electron and nuclear spins can induce similar equation to 2.14 including zero-field splitting equation (2.16) below at the remarkable existent of spin-orbit-coupling. This can often be ignored in the characterization of organic semiconductors based carbon [4, 5].

$$\hat{H}_{orbit} = \hat{S}_a^\dagger \tilde{D}_d \hat{S}_b \qquad (2.16)$$

2.1.2 Spin in a Magnetic Field

For an arbitrary system, the total magnetic field experienced can be determined by the static field B_0, the microwave pulse B_1, and a detuning B_Δ (due for example to variation in the total hyperfine interaction with the ensemble of nuclear spins, known as the Overhauser field) where , $B_1 = [B_{x_1}, B_{y_1}, 0]$, and (for conventional EPR implementations), $B_\Delta = [0, 0, B_\Delta]$.

Considering the application of a microwave pulse as an operation that rotates a spin coherently from one state to another around the Bloch sphere by producing a magnetic field, the resonance frequency is $\omega_0 = \gamma B_0$ and the static field equal to zero as seen in figure 2.2 taken from ref [36]. The spin will examine the magnetic field for only the microwave pulses (driving field) when the spin resonance with the external field, while it will examine the driving field and the detuning together when the spin off-resonance [36].

$$B_{eff} = B_1 \qquad \text{for spin resonance (on-resonance)} \qquad (2.17)$$
$$B_{eff} = B_1 + B_\Delta \qquad \text{for spins detuned from resonance (off-resonance)} \qquad (2.18)$$
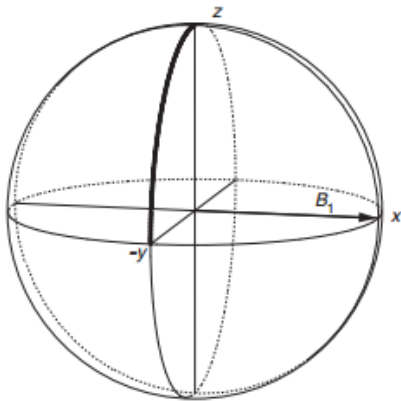
Figure 2.2: The magnetization vector during on-resonance with pulse angle 90^0 [36].

Lost fidelity due to the detuning in the spins from resonance can be reduced by using a variety of pulse schemes [36].

2.1.3 Spin Relaxation

2.1.3.1 Relaxation theory

In order to observe magnetic resonance absorption, spin relaxation is required. In EPR or NMR, the variation of signals with time can be described by spin relaxation. That variation relates to the increase of the population of an excited state, which called a non-equilibrium state. Spin relaxation is caused by the interaction between a spin and its environment. The transient behavior of spin-dependent recombination rates can be affected by both spin-lattice and spin-spin relaxation [35, 37].

Spin-lattice relaxation enables the spin system to return to its balanced 'equilibrium' state along the static magnetic field direction where a component of a magnetization vector would reach the thermal equilibrium with the spins surrounding it. In this type of relaxation, the equilibrium system provides the transition energy, therefore the spin system returns back to its equilibrium state. In general, the spin-lattice relaxation time (T_1) is used to describe the characteristic time for that transition, while it refers to the sample z-magnetization reaching its equilibrium value in magnetic resonance spectroscopy [35].

Spin-spin relaxation refers to the decay of the transverse component of the magnetization vector wards its equilibrium value. The characteristic time that generally describes this type is spin-spin relaxation time is conventionally labeled (T_2). The contribution of the spin-spin relaxation time can be divided into two parts, adiabatic and non-adiabatic. One is due to the limitation of the spin states lifetimes, therefore T_2 contribute as T_1 and called a non-adiabatic contribution. The other is due to the random disorder in the spin system, the energy differences of the states fluctuates [35].

The fact that the relaxation results from the fluctuating interactions between spins has extended the observation of magnetic resonance spectra. In order to solve these fluctuating interactions and therefore the impact on the spin system, there are two methods which can be applied to treat stochastic and dynamic processes [35].

For the spin system in the stochastic method, considering the random modulations which are caused by the perturbation as a stochastic process, and the effective Hamiltonian would be a function of stochastic variables $\Omega(t)$, written as:

$$\hat{H}(t) = \hat{H}_0 + \hat{H}_1(\Omega(t)) \tag{2.19}$$

where $\hat{H}_0$ is the unperturbed Hamiltonian, and $\hat{H}_1(\Omega(t))$ is the stochastic perturbation [9], with spin variables following the quantum Liouville-von Neumann equation [35, 38]:

$$\frac{d\rho}{dt} = -i[\hat{H}(t), \rho(t)] \tag{2.20}$$

In the dynamic process, describing the lattice by classical or quantum mechanics is possible, but only the quantum mechanics solves the spin systems. The Hamiltonian in the quantum mechanical description of the lattice can be written as:

$$\hat{H} = \hat{H}_I + \hat{H}_{IF} + \hat{H}_F \tag{2.21}$$

where $\hat{H}_I$ is the Hamiltonian in the spin system, $\hat{H}_F$ is the Hamiltonian in the lattice, and $\hat{H}_{IF}$ is spin-lattice coupling Hamiltonian [35], and the time evolution of the density matrix is given [35, 38] by equation 2.20

In the semi-classical mechanics, depending on the underlying stochastic processes formalism of the motion, the lattice is described by random functions, and the Hamiltonian contains time-dependent and time-independent terms [35] as shown in equation 2.19.

2.1.3.2 Redfield Theory

For a quantum system weakly coupled to an environment, using Redfield approach gives a clear description to the time evolution for density operator, which would give more explanation to the relaxation. Considering that, then the Hamiltonian of this system would be:

$$\hat{H} = \hat{H}_s + \hat{H}_\varepsilon + \hat{H}_I \tag{2.22}$$

where $\hat{H}_s$ describes the Hamiltonian of system S, and $\hat{H}_\varepsilon$ of the environment, while $\hat{H}_I$ describes the interaction between the system and the environment, with A interaction acting on the system and B on the environment:

$$\hat{H}_I = \sum_k A_k \otimes B_k(t) \tag{2.23}$$

The dynamic of the total system (S and ε) is coherent, and the state of the total system at time t, which performing the density matrix interaction is:

$$\rho(t) = \hat{U}(t)\rho'\hat{U}(t)^\dagger \tag{2.24}$$

And the interaction picture for $\hat{H}_I$ is:

$$\hat{H}_I(t) = \hat{U}^\dagger(t)\hat{H}_I\hat{U}(t) \tag{2.25}$$

with a unitary transformation:

$$\hat{U}(t) = exp\left[-\frac{i}{\hbar}(\hat{H}_s + \hat{H}_\varepsilon)t\right] \tag{2.26}$$

Now, the Liouville-von Neumann equation in eq.-2.20 has the solution:

$$\rho(t) = \rho(0) - i\int_0^t ds[H_I(s), \rho(s)] \tag{2.27}$$

By tracing the density matrix interaction picture over the environment, the evolution would be:

$$\rho_s = Tr_\varepsilon\{\rho(t)\} \tag{2.28}$$

After inserting in (2.27) and differentiating, we obtain:

$$\frac{d}{dt}\rho_s(t) = -\int_0^t ds Tr_\varepsilon\{[H_I(t), [H_I(s), \rho(s)]]\} \tag{2.29}$$

By assuming a weak interaction between the system and the environment, the total density operator is:

$$\rho(t) = \rho_s(t) \otimes \rho_\varepsilon \tag{2.30}$$

Which introduce the closed equation of motion for ρ_s called the Redfield master equation:

$$\frac{d}{dt}\rho_s(t) = -\int_0^t ds Tr_\varepsilon\{[H_I(t), [H_I(s), \rho_s(s) \otimes \rho_\varepsilon]]\} \tag{2.31}$$

[39, 40].

2.1.3.3 Spin Dynamics

Due to the invalid expectation of rapidly decaying correlations in the environment in some cases, the complete dynamic system cannot be described by a Markovian master equation [40].

In order to treat the statistical ensemble spin dynamics, generation, recombination, dissociation and relaxation effects have to be considered. Thus, the stochastic-Liouville equation is used to describe the

dynamics of a statistical ensemble of quantum systems whose time evolutions depend on the relevant Hamiltonian.

$$\frac{d\hat{\rho}}{dt} = -\frac{i}{\hbar}[\hat{\rho}, \hat{H}] + \hat{S}[\hat{\rho}] + \hat{R}\{\hat{\rho} - \hat{\rho}_0\}$$ (2.32)

where $\hat{\rho} = \hat{\rho}(t)$ is the density matrix operator, $\hat{S}$ is the stochastic operator and refers to the external changes the ensemble due to generation, spin-dependent recombination, and dissociation of spin pairs, $\hat{R}$ describes the influence of the spin relaxation, and the Hamiltonian $\hat{H}$ has time-dependent and time-independent terms [4, 5, 17, 37] can be written as in equation 2.4.

For two spin ½ systems in Hilbert space, the density operator is represented as a 4x4 matrix [33, 34]:

$$|\Psi\rangle = |\Psi_1\rangle |\Psi_2\rangle = \begin{pmatrix} 1 \\ 0 \end{pmatrix} \otimes \begin{pmatrix} 1 \\ 0 \end{pmatrix} = C$$ (2.33)

then

$$\rho_0 = C'C$$ (2.34)

where $C' = (1\ 0\ 0\ 0\ )$, and the Hamiltonian can be written as [5]:

$$\hat{H}_0 = \mu_B g_e B_0 S_e^z$$ (2.35)

$$\hat{H}_1 = \mu_B g_1 [\hat{S}_{x1} B_x(t) + \hat{S}_{y1} B_y(t)] + \mu_B g_2 [\hat{S}_{x2} B_x(t) + \hat{S}_{y2} B_y(t)].$$ (2.36)

By diagonalized $\hat{H}$ using a unitary transformation in order to clarify the underlying physics:

$$\hat{H}_{energy} = \hat{U}^\dagger_{energy} (\hat{H}_0 + \hat{H}_1(t))\hat{U}_{energy}$$ (2.37)

where $\hat{U}_{energy} = \begin{bmatrix} 1 & 0 & 0 & 0 \\ 0 & \cos\theta & \sin\theta & 0 \\ 0 & -\sin\theta & \cos\theta & 0 \\ 0 & 0 & 0 & 1 \end{bmatrix}$ (2.38)

with $\tan 2\theta = \frac{J - 2D/3}{\Delta w}$ (2.39)

Here J is the exchange interaction, D the dipolar interaction, $\Delta w = w_e - w_h/2$, and θ is the spin mixing angle.

The recombination operator is given by:

$$\hat{S} = -r_s . \hat{S}_s - r_t . \hat{T}_s \tag{2.40}$$

where $\hat{S}_s$ is the singlet subspace:

$$\hat{S}_s = \begin{bmatrix} 0 & 0 & 0 & 0 \\ 0 & 1/2 & -1/2 & 0 \\ 0 & -1/2 & 1/2 & 0 \\ 0 & 0 & 0 & 0 \end{bmatrix} \tag{2.41}$$

and $\hat{T}_s$ is the triplet subspace:

$$\hat{T}_s = \begin{bmatrix} 1 & 0 & 0 & 0 \\ 0 & 1/2 & 1/2 & 0 \\ 0 & 1/2 & 1/2 & 0 \\ 0 & 0 & 0 & 1 \end{bmatrix} \tag{2.42}$$

and r_s and r_t are singlet and triplet recombination rate respectively.

By transforming the recombination matrix into the energy eigenbasis:

$$\hat{S}_{energy} = \hat{U}^{\dagger}_{energy} \, \hat{S} \, \hat{U}_{energy} \tag{2.43}$$

The relaxation term can be written as:

$$\hat{R}\{\hat{\rho}(t) - \hat{\rho}_0\} = \hat{R}_{e/h} \otimes \hat{I} + \hat{I} \otimes \hat{R}_{e/h} \tag{2.44}$$

where $\hat{R}_e$, $\hat{R}_h$ are the electron and hole relaxation term respectively and calculated separately by:

$$[\hat{R}_{e/h}\{\hat{\rho}(t) - \hat{\rho}_0\}]_{ij} = \sum_{k=1}^{4} \sum_{l=1}^{4} \hat{R}_{e/h_{ijkl}}\{\hat{\rho}_{kl}(t) - \hat{\rho}_{0_{kl}}\} \tag{2.45}$$

This would present a Redfield matrix with coefficients:

$$\hat{R}_{e/h_{ijkl}} = \begin{cases} \dfrac{1}{T_{1_{e/h}}}, & \text{if} \quad i = j = k = l \\[2ex] \dfrac{-1}{T_{1_{e/h}}}, & \text{if } i = j, k = l, i \neq k \\[2ex] \dfrac{1}{T_{2_{e/h}}}, & \text{if } i \neq j, k \neq l \\[2ex] 0 & \text{otherwise} \end{cases} \tag{2.46}$$

16

where T_1 is the spin-lattice relaxation time, and T_2 is the spin-spin relaxation time.

Redfield matrix here is called a relaxation superoperator ($\hat{R}_{super}$) and it is in the superoperator formalism which is used to transform the matrix from Hilbert space ($n \times n$) to Liouville space ($n^2 \times n^2$) in order to have accuracy and speed improvement. Therefore, transforming the total Hamiltonian, recombination operator, and density matrices is required.

The recombination (stochastic) superoperator is given by:

$$\hat{S}_{super} = \hat{S}_{energy} \otimes \hat{I} + \hat{I} \otimes \hat{S}_{energy} \tag{2.47}$$

The super Hamiltonian can be written as:

$$\hat{H}_{super} = i\hat{H}_{energy} \otimes \hat{I} - i\hat{I} \otimes \hat{H}_{energy} \tag{2.48}$$

where the super observable is:
$$\hat{O}_{super} = Trace(\hat{O}^{\dagger}\hat{\rho}(t)) \tag{2.49}$$

The density matrix would be transformed as shown below [5, 37]:

$$\hat{\rho} = \begin{bmatrix} a_{1,1} & a_{1,2} & \cdots & a_{1,n} \\ a_{2,1} & a_{2,3} & \cdots & a_{2,n} \\ \vdots & \vdots & \ddots & \vdots \\ a_{m,1} & a_{m,2} & \cdots & a_{m,n} \end{bmatrix} \rightarrow \begin{bmatrix} a_{1,1} \\ a_{1,2} \\ a_{1,3} \\ \vdots \\ a_{m,n} \end{bmatrix} \tag{2.50}$$

2.2 Electron spin resonance

2.2.1 ESR

EPR (also often referred to as ESR) is a technique used to manipulate spin in materials with unpaired electrons such as organic semiconductors. The principle of EPR/ESR is the absorption of electromagnetic radiation by electrons, usually in the presence of a strong magnetic field. The spins for these unpaired electrons have either same or opposite directions that leads to have different energies levels, primarily due to the interaction between unpaired electrons and the magnetic field [20, 21]. Such a technique has many useful applications in physics, Chemistry, Materials Research, Biology and Medicine.

In 1946, NMR had improved in theoretical time domain area by Felix Bloch, with experimental demonstrations by Torrey and Hahn. During 1960s, the rise of Fourier transform had led to enhancement in NMR accuracy and resolution, which produced to exploit time domain to improve series of pulses and analysis framework. EPR/ESR and NMR have similar techniques; however, NMR concentrated on time domain area while EPR/ESR investigated electron spin with strong magnetic field which delayed the utilization of EPR till 1980s [5].

In 1993, EPR with high frequency and pulse EPR has been developed. The g-factor values with high resolution are one of the benefits of that development, which is useful to determine spectrum range for systems at the lower field. Moreover, improving the sensitivity of EPR measurements, which is important for systems with lower coherent paramagnetic species. Detecting NMR has been effective due to the development of pulse EPR through the investigating of hyperfine techniques of Electron Nuclear Double Resonance (ENDOR), Electron Spin Echo Envelope Modulation (ESEEM), and Electron Electron Double Resonance (ELDOR) [41].

The utilization of amplitude and frequency to include pulses has developed the sensitivity of pulsed NMR technique [42]. Although the developing techniques in NMR and ESR are similar, however, the applications to use short microwave frequency pulse are limited [17, 42].

As mentioned previously, in order to understand the dynamics of the materials, measuring the differences of the energy level in the molecular is needed, and Zeeman effect is the main responsible for that difference in ESR/EPR spectroscopy. In EPR experiment, often the frequency stayed constant while the magnetic field is changed, and the transition exists when the applied frequency is about 2.8 MHz per Gauss of magnetic field. Although, it is about 9-10 GHz per 3400 Gauss of magnetic field in organic radicals [41]. In fact, Rabi frequency spectroscopy is appropriate to examine spin with high system, therefore using Rabi technique to motivate transition through microwave field would lead to clearly define spin multiplicity of different spin types [42].

However, EPR/ESR measurements are sensitive to charge in polarization [5], and since the excitation time is longer than phase coherent time in quasi continues microwave fields, this leads to limited use of EPR/ESR because the effective of coherent observation has been forbidden [42].

The principle of ESR spectroscopy is the absorption of the electromagnetic radiation that leads to a change in the spin state of the electron [20, 21].

Measuring the energy differences of these levels in atoms or molecular leads to understand the dynamics and the processes of the materials. In ESR spectroscopy, the main cause for these differences is the interaction between unpaired electrons and the magnetic field B_0, which called the Zeeman Effect. The energies differences level for such a system is given by:

$$E = \pm \frac{1}{2} g_e \mu_B B_0 \qquad (2.51)$$

where g is the electron g-factor, μ_B is Bohr magneton, and B_0 is external magnetic field strength which causes the positive and negative signs by creating two energy levels for the magnetic moment of the electron; up (same direction with magnetic field) and down (against the magnetic field).

The diagram shows energy levels splitting in a magnetic field:

$m_s = -\frac{1}{2} : E = -\frac{1}{2} g_e \mu_B B_0$

$\Delta E = g_e \mu_B B_0$

$m_s = +\frac{1}{2} : E = +\frac{1}{2} g_e \mu_B B_0$

$B_0 = 0$ $B_0 \neq 0$ Magnetic field
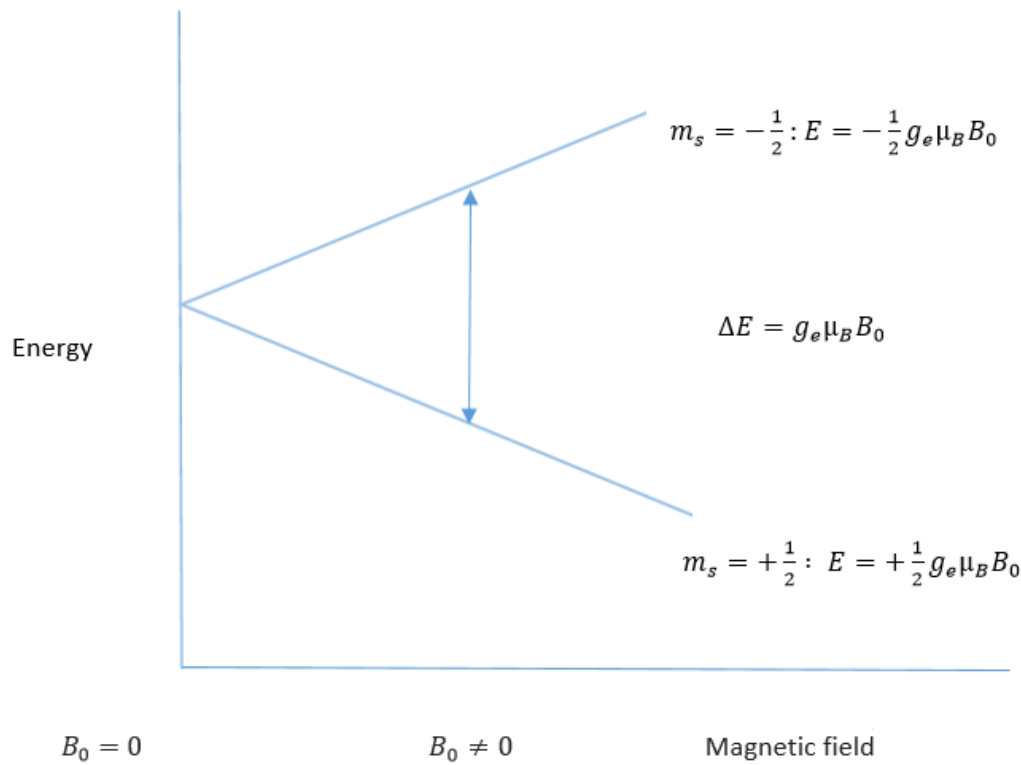
Figure 2.3 : The energy levels of a spin 1/2 state (e.g. electron) in a magnetic field [20, 21].

A transition from lower to higher energy states resultes from applied energy into the frequency v

$$v = g \mu_b B_0 / h \qquad (2.52)$$

which leads to define the resonance condition by corresponding to Planck's law:

$$\Delta E = hv \qquad (2.53)$$

where h is Planck's constant, and v is the radiation frequency [20, 21].

2.2.2 Modelling ESR

Applying microwave radiation at fixed frequency (driving field) along with an external magnetic field (B_0) which is swept adiabatically would lead to perform ESR and EDMR as continuous wave experiments (cw) [4, 5]. However, these experiments have limitations in their ability to provide information from beyond those seen in spectra such as g factor, hyperfine coupling constant, and spin relaxation. Therefore, using pulsed-ESR (p-ESR) in order to define spin coherence times and dynamic information about organic semiconductors would be extremely effective [4]. Performing ESR in the time domain (p-ESR) would be achieved by applying short and powerful pulses of radiation effects, spin coherence manipulation, and excitation bandwidth supply. Thus, measuring spin relaxation times and producing higher spectral and time resolution can be provided by p-ESR due to the ability of p-ESR to examine and treat the particular interactions. Defining ESR as a continuous wave experiment (cw) refers to the pulse length which should be longer than any relevant incoherent process while it refers to the faster excitation for a p-ESR experiment [5]. Replacing the quasi-static changes of polarization in cw experiments with transition frequency and amplitude at each field position would lead to p-ESR experiments [4, 5].

2.2.3 Pulsed ESR

Pulsed ESR (p-ESR) spectroscopy is a technique that has been used for over 50 years for studying the spin characteristics of materials. However, focusing on organic thin-film devices, p-ESR has some limitation which can be overcome by electrical rather than inductive detection [5].

Electrical detection of magnetic resonance, which uses electron spin resonance to manipulate spins and conductivity measurements to look at the resulting changes in transport properties, is particularly well suited to this challenge. Applying EPR to organic light emitting diodes (OLEDs) for example, has been shown to result in significant changes in the current through the device (ie electrical detection), enabling the spin dependent recombination rates of polaron pairs (exciton precursors) to be determined [15].

The spin polarization is determined in p-ESR experiments via the timescales of either spin echo or free induction decay. However, since the ESR experiments are sensitive to the polarization changes, performing high fidelity operations is effective for increasing the sensitivity in p-ESR [5].

2.2.4 Adiabatic Pulses for ESR

In order to improve the fidelity and excitation bandwidth to overcome inhomogeneous linewidths issue and to increase the signal amplitude in such experiments, pulse-EPR is been used. Various types of shaped pulses have been used to improve EPR and NMR techniques, such as Band-selective pulses, pulse trains, and adiabatic pulses [42].

The limitation of pulse EPR lies on limited excitation bandwidth of pulses due to microwave resonator and pulse power. However, that excitation bandwidth is often not sufficient to enable high fidelity electron spin control in the presence of realistic broadening of the resonance linewidth. Recently, arbitrary waveform generators (AWGs) are used to create (apply) and integrate pulses in EPR techniques. The spectra lines in some materials, organic semiconductors, for example, are greater than pulse bandwidth, therefore, increasing the excitation bandwidth and the sensitivity of pulse EPR is necessary, and can be achieve by adiabatic pulses. Practically, using adiabatic pulses has led to increased fidelity and sensitivity of ESR measurements [42].

Since the adiabatic pulse is a point-to-point rotation pulse, which basically offers reversal proceeds for all spins within specified pulse bandwidth, using the pulse power leads to detect spin rotation within defined bandwidth without effected the excitation shape pulse. B_1 can be performed to reversal insensitivity by the influence of adiabatic pulses when the critical adiabaticity equation satisfied, then the rotation angle θ and B_1^{max} are dissociated [42].

In order to preform high fidelity operations (high fidelity spin rotation), adiabatic pulses are needed. The application of adiabatic pulse schemes to improve both the sensitivity and fidelity of electrically detected magnetic resonance in organic devices is the main investigation of this thesis [43]. Whilst the application of these schemes (which have traditionally been limited to NMR) is emerging in electron spin resonance, their application to electrically detected spin resonance has been limited [44].

Adiabatic pulses are much more insensitive to inhomogeneity (B_1) and resonance offsets, and spins would have various manipulations resonance frequencies at different times [17, 45, 46]. Having specific absorption rate with sample heat decreasing would be an additional feature to adiabatic pulses [45, 46].

During the adiabatic passage, an adiabatic sweep which is the magnetization M follows the effective magnetic field ω_{eff} occur under the condition:

$$Q = \frac{\omega_{eff}}{|d\theta/dt|} \gg 1 \tag{2.54}$$

Where $\omega_{eff} = \gamma B_{eff}$ which is given by the summation of the microwave field (RF field) and the detuning (off-resonance) in the rotating frame at the Lamor frequency as:

$$\omega_{eff} = \omega_1 + \omega_\Delta(t) \tag{2.55}$$

$$\omega_1 = \gamma B_1 \hat{x} \tag{2.56}$$

$$\omega_\Delta(t) = [\omega_0 - \omega_{RF}(t)]\hat{z} \tag{2.57}$$

where ω_0 is the Lamor frequency, $\omega_{RF}(t)$ is the frequency of the pulse, and $d\theta/dt$ is the instantaneous rate of ω_{eff} [17, 42, 43, 45, 46].
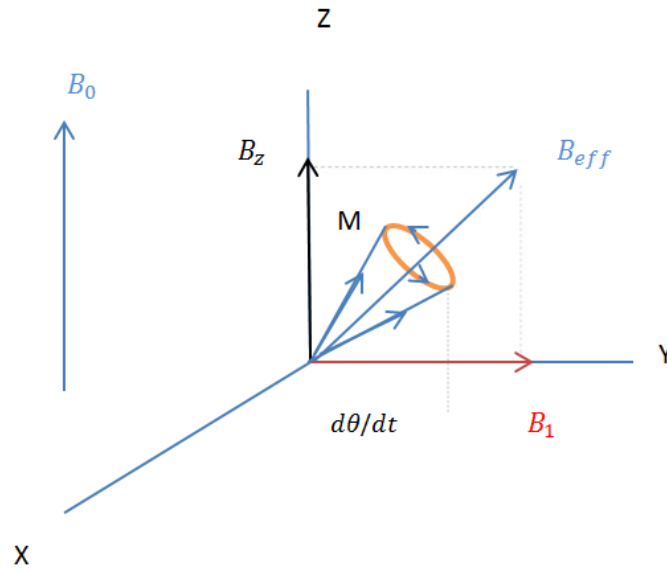
Figure 2.4: Visualization of the effective field and its components in the frames rotating at the RF ($\omega_{RF}(t)$ frequency.

Offset Independent Adiabatic Pulses (OIA):

 Offset independent adiabatic pulses (OIA) are one example of adiabatic pulses that tend to have circumstance adiabatically constant with known bandwidth [42]. Keeping the power constant over the required bandwidth is fundamental to preform uniform rotations over a large detuning ($\Delta\Omega$) by applying a pulse with amplitude and frequency combined modulation. The resulted energy from the pulse would be expanded sequentially in time over the bandwidth. This can be satisfied by adiabatic pulses which are defined by amplitude modulated AM and frequency modulated FM functions:

$$B_1(t) = \gamma B_1^{max} F_1(t)\hat{x} \tag{2.58}$$

$$\omega_\Delta(t) = [\omega_c - \omega_{RF}(t)] = [\omega_c - \omega^{max} F_2(t)]\hat{z} \qquad (2.59)$$

where γ is the gyromagnetic ratio, ω_c is the carrier wave frequency, B_1^{max} and ω^{max} are amplitude and frequency modulation respectively, and F_1 and F_2 driving function which define the modulation.

Using equations (2.59) above at each point in time $t < t_{pulse}$ leads to introduce the adiabatic ratio (adiabaticity) K:

$$K(t) = \frac{|\gamma B_1^{max} F_1(t)|^2}{\omega^{max} \dot{F}_2(t)} \gg 1 \qquad (2.60)$$

which can be written as:

$$K(t)\omega^{max} \dot{F}_2(t) = |\gamma B_1^{max} F_1(t)|^2 \qquad (2.61)$$

For all spins resonance frequency within the excitation bandwidth, must be larger than the frequency sweep changing rate ($\omega^{max} \dot{F}_2(t)$) by the same factor K [45, 46].

And the critical adiabaticity (Q_{crit}) is used for linear frequency sweep in FM pulses:

$$Q_{crit} = \frac{t_{pulse} \ (\gamma \ B_1^{max})^2}{2\Pi \ BW} \qquad (2.62)$$

where t_{pulse} is the pulse length, and the pulse bandwidth $BW = 2f_{max}$, f_{max} is the total sweep width [17, 42].

2.3 Electrical Detection of Magnetic Resonance (EDMR):

2.3.1 Background

Electrical and optical detection of magnetic resonance (EDMR /ODMR) are spectroscopy techniques which use ESR to manipulate spins and conductivity or luminescence measurements to look at resulting changes in transport or optical properties in inorganic and organic semiconductors. Usually, these methods applied for the materials characterization and detecting the impurities and defects in the solid samples [15, 19].

Traditionally, to investigate paramagnetic states in semiconductors magnetic resonance spectroscopies such as ESR or NMR have been used. The main idea of magnetic resonance techniques consists in the determination of the effective Landé factor (g-factor), which realises on the district fields and, based on the surrounding microscopic of a particular paramagnetic centre. In other words, the magnetic resonance methods allow detecting the impurities in the semiconductor as well as understanding the

processes that occur with these defects. Past years, different techniques used for these purposes. One of the first such methods was the traditional continuous wave (CW) magnetic resonance, realised on spectroscopy of adiabatic magnetic field. After that, it changed the spectroscopy of coherent magnetic resonance, which called pulsed ESR/NMR.

However, the application of ESR/NMR to semiconductor characterization faced some sensitivity limits, mostly about the orders of 10^{11} and 10^{15} spins, respectively. Therefore, the samples containing two- or fewer-dimensional structures (quantum wells, quantum dots or quantum wires) were hard to characterize. In order to overcome with this limitation, electrical and optical detection of magnetic resonance (EDMR/ODMR) have been used. Combining the magnetic resonance with conductivity in EDMR or photoluminescence in ODMR, has led to taking benefit of the spin-selection-rules of transitions in semiconductors [22, 23, 47, 48, 49].

The first EDMR experiment with the measurements of the bolometric effect was reported by Guéron and Solomon in 1965, while the first EDMR measurement depended on controlling electronic transitions by spin-selection rule was demonstrated by Hirose et al. and Maxwell in 1966 [24, 25]. The first cw-EDMR measurements exploiting a spin-dependent recombination mechanism were conducted in 1972 by Lepine and Prejean on a crystalline silicon sample [50]. After that, many cw-EDMR researches have been done to various semiconductor materials [51, 52, 53, 54] and devices [55, 56]. During the almost four decades, great amount of the experimental and theoretical work on the absorption of cw-EDMR experiments as well as the underlying processes has been implemented. However, transient EDMR experiments and coherent pEDMR experiments have been presented only at the end of the century [57, 58, 59]. The main challenge for transient EDMR measurement is related to the detection of small current changes on the background of comparatively large constant current offsets at a high time resolution. In most cases, it is hardly possible to conduct electrical measurements with a time resolution sensitive enough to detect the small signal currents and which will be within the coherence time of the spin systems. However, this was solved by means of an indirect detection scheme of the coherent dynamics during the excitation [37, 57, 58, 60, 61].

There are many different physical mechanisms which can cause EDMR signals, however, the most common focused on the transport of spin-dependent among two paramagnetic states of the electron. Spin conversion can be determined by weak spin orbit coupling, and the transition probability between singlet and triplet by spin permutation symmetry [26]. As it can be seen from fig 2.5 a) the transition probability reaches its maximum value if there is a state of spin-pair and a significant of high singlet created by the two spins. The basis to select spin, which is Pauli blockade, means the transitions in the states of spin-pair where higher singlet are probably extra than in pairs with higher triplet content.
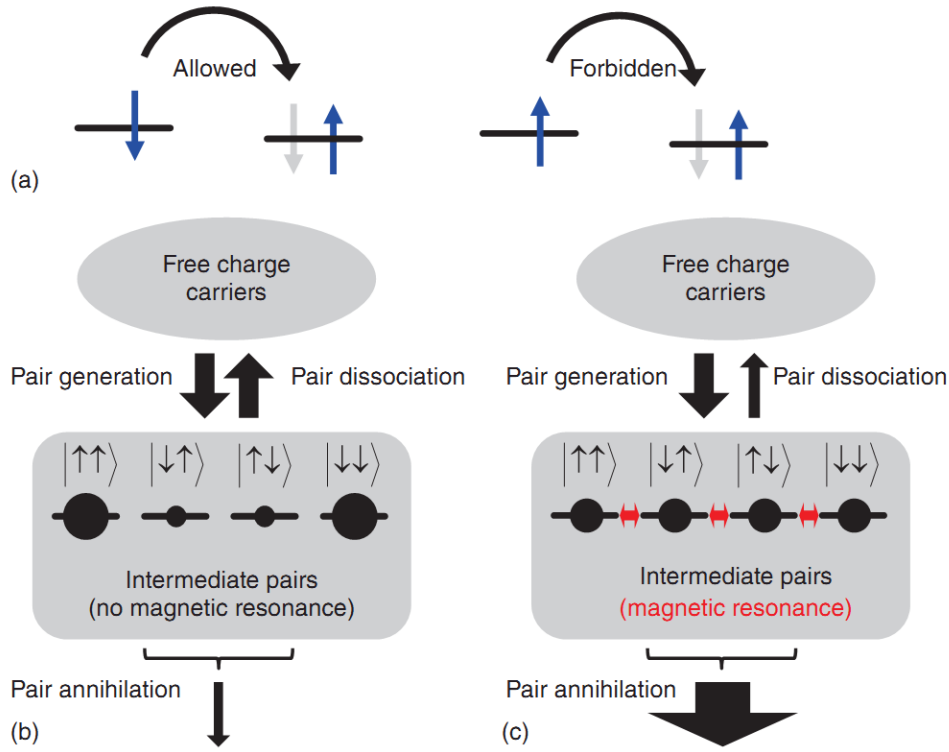
Figure 2.5: a) shows the electron transport of spin-dependent between two states of electron (S=1/2). b) & c) shows the rate- transport according to Kaplan, Solomon, and Mott description in the absent and the presence of magnetic resonance respectively [26]. Reprinted figure with permission from [C. Boehme, H. Malissa, "Electrically Detected Magnetic Resonance Spectroscopy", eMagRes, 83-100.13 (2017)] Copyright (2017).

Pauli blockade in Lepine's recombination model means when encounter happened between electron and hole, the probability is almost same, and the change of recombination rate will be defined when the charge carrier occurs. Therefore, the charge carrier changes from equilibrium to lower polarization state, then the transition rate changes due to magnetic resonance [26, 57].

Kaplan, Solomon and Mott (KSM) developed another recombination model, reported first in the case of Shockley-Read-Hall recombination, which differs from Lepine's model by considering the intermediate-pair states. This mechanism seen in in Fig. 2.5 b and c shows two electronic states, which can transform to singlet state or dissociate into free charge carrier. While the middle pair represents a weak system of 1/2 spin pairs, the formed during a spin-dependent transition singlet state composes the two strongly exchange-coupled electrons [25, 28, 62, 63, 64].

25

Furthermore, one can find also the examples of EDMR signals, whose origin has no connection to spin-pair processes . These cannot be explained by the middle-pair-based EDMR theories thus need other theories [62, 65, 66, 67, 68, 69, 70, 71].

2.3.2 Continuous-wave EDMR

The bulk of this research has been done using the basic continuous wave EDMR, where a spin spectrum is created by a steady sweep of magnetic field in presence of continuously irradiated electromagnetic radiation with constant frequency and intensity [72, 73, 74, 75]. Strong cw EDMR signals can be reached when the electronic processes transition times are smaller than the times of spin decoherence related to the mechanical processes of the electrons. Also, the frequencies modulations in cw EDMR are minimum than in EPR spectroscopy [68, 76]. An adiabatic frequency sweep experiment within a static magnetic field B_0 is other process to conduct cw EDMR spectroscopy. The ability to do this kind of the experiments is related to the wide frequency bandwidth of EDMR which is different than EPR experiments, but technically still not simple so it is not common in the literature [77, 78].

A typical cw EDMR experiment includes two electric circuits: one is used for spin excitation while the other is for detection. The setup for spin excitation is usually very similar to that used in conventional EPR. The easiest application of an MW magnetic field B1 to the sample requires only having a radiofrequency or MW with an attenuator, a waveguide, and a resonant or non-resonant framework. [78]. Since the components required are not necessarily narrowband, EDMR is inherently suitable for multi frequency applications. Magnetic resonance in EDMR experiments is electrically discovered by measuring a sample-conductivity change. Thus, the observations preform through a sensitive measurement of sample resistivity, and realize by applying a constant voltage with the simultaneous recording of the device current with a sufficiently fast current amplifier. Such measurements often require separate electrical circuit than the circuit of the MW excitation as well as the minimization of the crosstalk between the two circuits [79, 80].

In addition to these components, almost all the preparations of the laboratory for cw EDMR configuration are prepared by a lock-in amplifier, additional Helmholtz coils, and cryostat facilities. cw EDMR spectroscopy is suitable when the highest sensitivities are needed. cw EDMR/ODMR experiments allow high spin sensitivity up to the level of single-spin sensitivity compared with standard EPR techniques, due to intermediate-pair mechanisms under non-equilibrium conditions [79, 80]. Although, cw EDMR experiments have some advantages in contrast with cw EPR, for instance, in the magnetic field and frequency dependence and high sensitivity, both experiments have been limited due to polarization-controlled mechanisms. Moreover, EDMR cannot be applied to any paramagnetic centre since this method requires that a paramagnetic state to be involved into a spin-dependent process in

order to allow multiple spin to control electronic transitions. Furthermore, EDMR spectra are determined by the parameters of spin-coupling, the spin-relaxation time of paramagnetic centres observation, and by electronic transitions dynamics. Therefore, EDMR spectra need much more parameters than EPR spectra, and for convoluted spectra, this feature has the ability lead to the important ambiguities for the analysis EDMR signals; quantitative as well as qualitative interpretation [47, 50, 79, 80].

2.3.3 Pulse EDMR

Mobility low-charge carrier has been noticed in a large number of materials which included spin-selection rules. Thus, dielectric relaxation of such materials is limited by having longer time compared to spin coherent time occurs. Practically, the ability to solve this problem is in the isolation of the two processes which prepare and detect the state of spin coherent during a pulse EDMR experiment. By looking to figure 2.6 below (taken from [26]), it shows the timeline of the experiment on a logarithmic time scale. Spin coherent manipulation is needed to excite pulsed EDMR in order to prepare a spin state charge carrier which relies on the length τ, the amplitude B1 and the frequency ω of the excitation pulse. The excitation occur time is much shorter than spin relaxation time. The detection of the pEDMR occurs by integration of the current for a long time, within a consideration of an identical charge Q with resonant motivation changes in conductivity. Through these changes, the experimenter counts the transports of charge which affected by the transitions of spin-dependent because of the excited magnetic-resonant. The detection of charge Q relies on both the state of spin σ following the excitation pulse and the excitation pulse parameters, and the detection should be done on timescales longer than the dielectric relaxation time of the examined material to avoid the filtering by the the material's electrical signals which caused by spin.

The current of a spin-dependent is managed by a certain group spin, the integration of transient current induced by the charge excitation of a spin-resonant is directly proportional to the singlet content of the probed spin manifold at the end of the spin-excitation sequence as seen in fig.2.6 [26]. Therefore, repeating "spin resonant excitation pulse pumping/integral of charge-examination" leads to spin coherent observation to be determined. During that experiment, the sequence of spin excitation is performed frequently, while little changes are noticed in some parameters, this leads to increase the duration of measurements during the pEDMR experiments compared with pEPR experiments. However, this allows to solve the problem of an essential limited time resolution, which is caused by dielectric relaxation. Therefore, this experiment introduced the new possibilities for the same area of spectroscopy tools that is realized from classical pEPR spectroscopy [26, 37, 81].
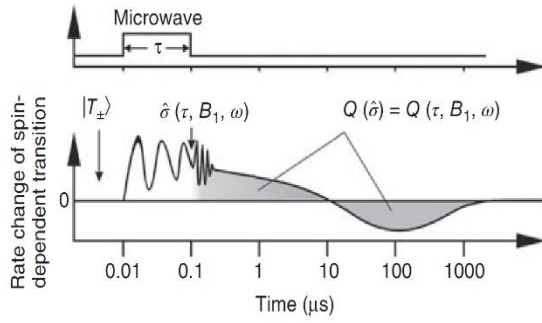
Figure 2.6: shows pEDMR experiment time using logarithmic time scale [26]. Reprinted figure with permission from [C. Boehme, H. Malissa,"Electrically Detected Magnetic Resonance Spectroscopy", eMagRes, 83-100.13 (2017)] Copyright (2017).

The first and the simplest scheme for pulsed EDMR measurements was implemented by C. Boehme and K. Lips. In 2002, C. Boehme has presented the experimental setup for pEDMR in [57].
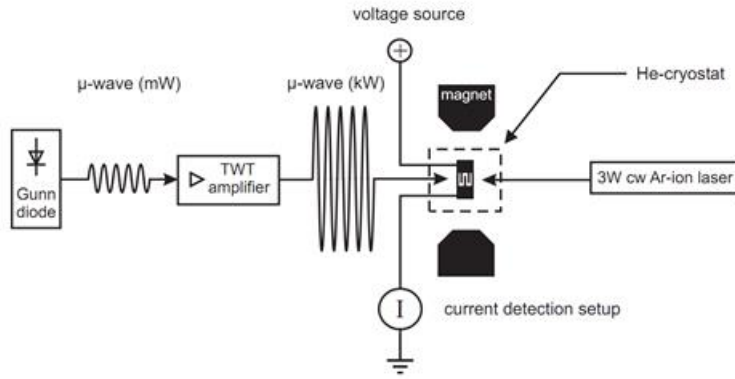
Figure 2.7: The standard setup of pEDMR [57]. Reproduced from C. Bohme, "Dynamics of spin-dependent charge carrier recombination", (2002).

This experiment was implemented by using microcrystalline silicon (μcSi:H). However, the pEDMR method can be applied for other semiconductors like organic based carbon semiconductors which was presented in ref. [15]. In contrast to the silicon-based samples, the results of pEDMR with organic carbon-based faces some challenges. Firstly, the contact to the sample should be in a careful way that the contacts do not distort and inhomogenize the B1 fields that is necessary for the spin manipulation. In addition, preparing the sample of pEDMR must be in fast and simple way and well encapsulated because a lot of semiconductors with carbon-based are sensitiv to ambient air. However, in the previous mentioned thesis [82], the special production method for pEDMR compatible thin film templates was presented in order to overcome these limitations [44, 83, 84, 85].

The presence of spin-dependent transitions is the most important applicability of pEDMR. Due to the weak spin orbit coupling which leads to spin conservation, spin selection rules produced which make pEDMR consonant with IV materials. Moreover, the transition in pEDMR experiments needs to be sufficiently slow in order to be investigated. Rabi frequencies of the order of 100 MHz can be produced at these frequencies ranges, thus, if the coherence decay time scales is more than 10 ns, then spin-coherent movement is possibly clear with pEDMR. For faster transitions, the detection of magnetic resonant changes in spin-dependent transition rates is possible, but not the effects of coherent spin-motion. The investigating of materials with fast decay approaches is resticted to the limited time resolution. The implementation of pEDMR can be done just on spin-dependent transitions where the mutual spin-spin couplings within the pairs are in an average domain. However, if the coupling is weak, then the chance of transition is small, and then the current signal is not interest. [5, 15, 26, 57, 82].

2.4 Magnetic field sensing

2.4.1 Magnetic resonance based sensing

Magnetic resonance (MR) based sensors have the ability to bring electromagnetic radiation into resonance with paramagnetic centres to determine a magnetic field if the Landé factor of the material is known, and using Planck's fundamental relationship between the frequency of the radiation and the its energy. Also, MR- based sensors allow to determine the shift and offset of magnetic field for intermediate to strong fields [16].

There are a large number of techniques available for magnetic sensing. These include, for instance, scanning superconducting quantum interference device (SQUID) microscopy, scanning semiconductor-based Hall probe microscopy, magnetic force microscopy [86], and optical magnetometry [87], which can provide the micron-scale resolution in sensing. More interesting and promising are the new experimental methods for magnetic sensing in nanoscale region: spin-polarized scanning tunneling microscopy [88]. However, most of them face a lot of challenges when measuring the small magnetic fields. One of the problems, for example, is the fact that magnetic fields decay rapidly with distance, by the $1/r^3$ law. Using slow quantum systems as a detector is critical to overcome this issue and measure such small fields. The principle of that is to manipulate spin 1/2 quantum states directly which can be very sensitive to small magnetic field changes.

2.4.2 Spin resonance magnetic field sensing

The simplest way to measure a magnetic field using a spin is to look at the position of the resonance.

From Planck's law:

$$\Delta E = hv \tag{2.63}$$

$$\Delta E = g\beta B_0 \tag{2.64}$$

Where $\beta = 9.274 \times 10^{-28}$ J.G^{-1}, B_0 is external magnetic field, and g is g-factor.

In order to calculate g, the value of the energy between the two spin levels should be determined by illumination with microwave radiations with a known frequency and magnetic field sweeps on the sample.

Therefore:

$$g = \frac{hv}{\beta B_0} \tag{2.65}$$

$$g = 0.7145 \frac{v(MHz)}{B_0(Gauss)} \tag{2.66}$$

As a result from that and previous discussion in section (2.2.1), the energy difference between two spin eigenstates is related to the magnetic field felt by the spin.

Changing the magnetic field strength leads to change the energy differences between two spin levels. Therefore, the spectrum is acquired by applying a constant magnetic field and scanning the microwave radiation of the frequency or by remaining the frequency stable and scanning the magnetic field [20, 21]. Note that, different magnetic field strength would require different magnetic sensors [86].

By looking at the resonance position, this approach is limited by the inhomogeneous broadening of spin resonances which limits sensing capability.

2.4.3 Coherent approaches to spin sensing

Techniques exist for reducing the impact of disorder, which can be applied to improve the sensitivity with which a spin 1/2 can be used to measure a magnetc field.

In particular, it is the presence of long spin phase coherence times (> 0.5 µs) at room temperature that is of particular interest [11]. Phase sensitive approaches to field sensing allow greater sensitivity [89], and have been effectively used in other materials (such as NV centers in diamond [19]). The challenge in applying such techniques to organic devices is related to the disorder that is inherent in the material, which leads to inhomogeneous broadening of spin resonances [16].
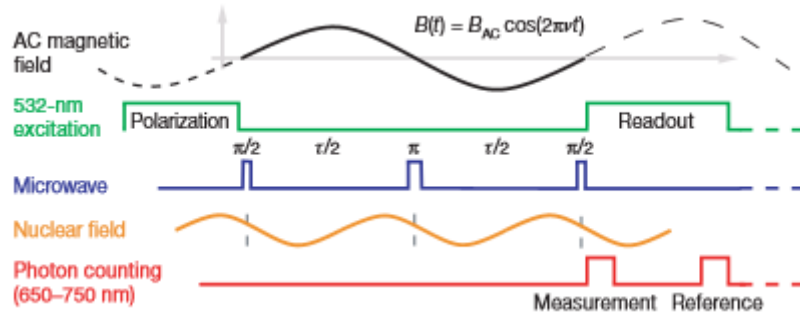
Figure 2.8: Optical and microwave spin-echo pulse sequence used for AC magnetic field sensing, taken from [19]. Reprinted by permission from [J.R. Maze, P.L. Stanwix, J.S. Hodges, S. Hong, J.M. Taylor, P. Cappellaro, L. Jiang, M.G. Dutt, E. Togan, A.S. Zibrov, and A. Yacoby, "Nanoscale magnetic sensing with an individual electronic spin in diamond", Nature 455, 644-647 (2008)., [COPYRIGHT] (2008).

Fig 2.8 shows the standard method to detect a Zeeman shift.

The application of $\pi/2$ phased pulse to a spin-½ particle placed into external field B generates a superposition of two Zeeman levels. During the free interval evolution time τ, these levels obtain the relative phase

$$\phi \propto (g\mu_B/\hbar)B\tau \tag{2.67}$$

Where $g \approx 2$ for nitrogen vacancies, μ_B is the Bohr magneton and $\hbar$ is the reduced Planck constant. Changing the relative phase to the different population energy level is implemented by a $\pi/2$ pulse, and the population difference can be measured optically in order to obtain the value of the Zeeman shift. The linear dependency between the magnetometer signal and relative phases values occurs when the relative phases are small. The measurements are repeated several times in order to increase the sensitivity and exclude the fluctuations, and that called averaging interval T. With consideration of shot-noise-limited sensitivity the minimum detectable field is given by the expression:

$$B_{min} \equiv \eta/\sqrt{T} = \frac{\hbar}{g\mu_B\sqrt{\tau T}} \tag{2.68}$$

Changing the time of interrogation τ, one can control the sensitivity of experiment. However, at some point, the τ increasing will result in the sensitivity decreasing due to random perturbations affecting the measurements. Thus, the optimal sensitivity for this type of magnetometry will be achieved, when the

interrogation time is approximately equal to the time T_2^* of dephasing caused by the interactions of the spin ½.

$$\eta_{d.c.} \approx \hbar / \, g\mu_B C \sqrt{T_2^*} \qquad\qquad\qquad (2.69)$$

where $C \leq 1$ is the constant parameter, which depends on the experimental setup features [89].

Although magnetometry with single electronic spin manipulation opens new possibilities for the detection of very small magnetic fields, this method faces some challenges, especially connected with the high impact of spin projection noise and spin coherence time on the sensitivity of the proposed magnetometers. Special quantum coherent control techniques have used in order to overcome these issues. For instance, the application of various types of sequences such as modified by extra pulses Ramsey sequence, Carr-Purcell-Meiboom-Gill (CPMG) sequence [90], as well as a simple idea of the many sensing spins utilization, was proposed [89]. All these modifications affect the sensitivity and are important for specific experiments.

However, MR magnetometers are large and expensive, limiting relevant applications. We could, however, use spin-dependent electronic transition in an organic diode in order to overcome with these limitations by having electrical (EDMR) or optical (ODMR) detection of MR. With an extremely low magnetic field, the sensitivity of EDMR and ODMR is higher because the signal is independent of spin polarization [16].

This has been implemented in diamond see section 2.4.4, and it is also, implemented in OLED's see section 2.4.5. This thesis is focusing on developing a technique that approaches these devices. The main investigation of this thesis is to improve both the sensitivity and fidelity of electrically detected magnetic resonance in organic devices by using adiabatic pulses. However, these approaches is appearing in ESR and have been traditionally limited to NMR , and their application to electrically detected spin resonance has been limited.

2.4.4 Magnetic resonance-based sensor in diamond

 The first successful realization of this idea was made using a nitrogen-doped nanoscale diamond [89]. Adding one N atom to the carbon structure (diamond), along with a neighbouring vacancy, results in an additional unbound electron occurring, which can be excited by a laser pulse, causing the electron to emit radiation. According to the Zeeman law, the energy levels of one electron placed in a magnetic field will split into Zeeman sublevels Thus, analyzing the frequencies of emitted radiation and detecting the mentioned energy splitting allows small magnetic fields to be determined.
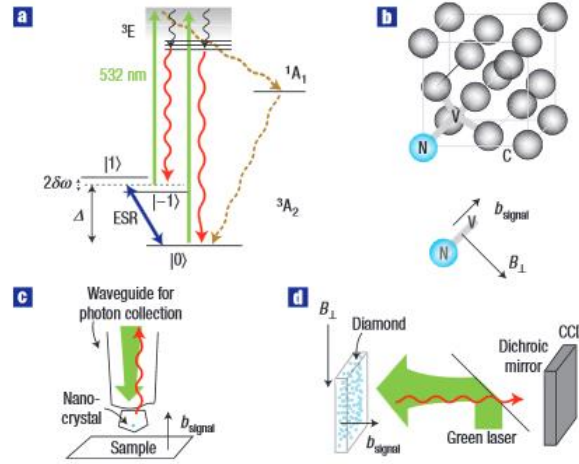
Figure 2.9: The experimental setup by Taylor, et al., 2008 [89]. Reprinted by permission from J. M. Taylor, P. Cappellaro, L. Childress, L. Jiang, D. Budker, P. R. Hemmer, A. Yacoby, R. Walsworth, and M. D. Lukin, "High-sensitivity diamond magnetometer with nanoscale resolution", Nature Physics **4,** 810-816 (2008). [COPYRIGHT] (2008).

Figure 2.9 a shows the principal scheme of the single nitrogen-vacancy center energy level structure including the Δ = 2.87 GHz crystal field splitting and a Zeeman shift $\delta\omega$, the nitrogen-vancy-center's ground state is spin triplet. The green laser light applied to this center (at room temperature) stimulates spin-dependent photoluminescence, which allows to optically detect the electron spin resonance. The continuous illumination of the nitrogen-vacancy spin in diamond leads to its pumping into the ground state m_s=0. Figure 2.9 b reveals the crystal structure of the diamond detector with a (111) nitrogen-vacancy center. When the static bias field $B\perp$ is applied to the 111 axis, the signals of small magnetic fields aligned with the 111 axis are detected. Figures 1c and 1d demonstrate two principal schemes of the measurement device. The diamond nanocrystal with nitrogen vacancy placed at the end of the detecting probe containing a waveguide for photon collection (Fig. 2.9 c). The second scheme includes a macroscopic diamond sample with several vacancies, dichroic mirror and the charged-coupled device, which measures the spin-dependent photoluminescence produced through the green laser light impact on the diamond sample. The magnetic field resolution of the scheme on Fig. 2.9 c is limited by the size of the nanocrystal while on Fig. 2.9 d the resolution limitations are related to optical reasons.

The highly sensitive magnetometer based on the ensemble of nitrogen-vacancy centers in diamond was determined in [91]. Its deviation of the magnetic field for 100 s measurements reached 100 fT, while the photon-shot-noise-limited magnetic-field sensitivity for 20 kHz ac (alternating current) signals was

equal to 0.9 pT/$Hz^{1/2}$. Another scheme for the similar detector placed in the optical resonator and having the sensitivity around 20 pT/$Hz^{1/2}$ was reported in [92]. The ensemble of nitrogen-vacancy centers in a single-crystal diamond was also used in order to create the vector magnetometer capable to produce the continuous measurements of all Cartesian components for a dynamically altering magnetic field [93]. This device can be used in a broad range of frequencies (from 5 Hz to 1.5 kHz) and achieve 50 pT/$Hz^{1/2}$ magnetic-field sensitivity for each Cartesian component.

2.4.5 Magnetic field sensing in an organic light emitting diode (OLED)

Due to their ability to transduce spin information into both optical and electrical signals, a number of proposals have emerged to utilise OLEDs as magnetometers [16]. This is motivated by a number of perceived advantages – the physical properties of organic devices, particularly their flexibility, allows a range of unique uses, a spin resonance based sensor allows calibration free operation, and the ability to operate at room temperature opens up applications in biology [11].

Organic semiconductors and other electronic devices such as organic light emitting diodes (OLEDs) [94, 95] organic solar cells [96, 97] and organic field effect transistors [98, 99] have been widely studied for more than three decades. Recently, OLEDs have been attractive in display industries as they have better features compared to displays made of liquid crystals, such as better response time, lower cost, higher efficiency, and better picture quality and flexibility [1].

A regular OLED is made with an organic semiconductor layer placed between two non-magnetic electrodes and placed on top of a glass substrate (see Fig. 2.10 a). The highest occupied and lowest unoccupied molecular orbital (HOMO and LUMO, respectively) energy levels of the active layer (polyfluorene) and the principle work of common materials are presented in Fig. 2.10 b. After applying the voltage to the OLED the recombination and excitation of polaron pairs occur and the device produces light, which leads to the formation of singlet and triplet polaron-pair states (pp_s, pp_T). The steady-state density of the Polaron pair relies on the various factors such as dissociation and recombination rate constants, and on the spin mixing between the singlet and triplet manifolds. If $k_s \neq k_T$, then the change of singlet and triplet mixing rate leads to a non-equilibrium steady state and changing the efficiency emission and polaron density. The change of singlet and triplet mixing rate can be caused by triplet-triplet annihilation, hyperfine interaction from adjacent hydrogens, triplet-polaron inter-action, or an applied magnetic field B [1].
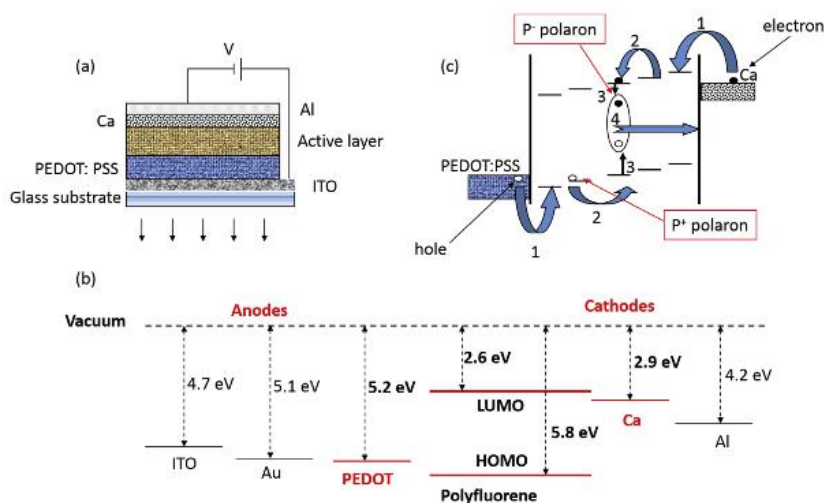
Figure 2.10: a) Typical OLED device. b) Principal work of some common metals of which electrodes are made and HOMO and LUMO energies of polyfluorene organic semiconductors. The materials on the left and right sides are playing the role of the charge injection electrodes. c) The OLED work structure shown in four fundamental processes: (1) charge injection; (2) charge transporting; (3) the P+ and P- polarons recombination; and (4) exciton formation and light emission. Figure is taken from [1]. Reproduced from R. Geng, T. T. Daugherty, K. Do, H. M. Luong, & T. D. Nguyen, "A review on organic spintronic materials and devices: I. Magnetic field effect on organic light emitting diodes", Journal of Science: Advanced Materials and Devices, 1(2), 128-140, (2016).

Fundamentally, applying an external magnetic field to OLED and changing the emission efficiency can be used for magnetometry measurements. The OLEDs made of Alq3 showed the modulation of the current density and electroluminescence by applying magnetic field around 100 mT [100]. In addition, increasing the magnetoresistance up to 30% in polyfluorene -based OLEDs for the same magnetic fields was demonstrated later [101]. In order to explain theoretically the organic magnetoresistive effect in OLEDs at magnetic fields <100 mT, there have been different models proposed: (i) the bipolaron mechanism (BP) [102, 103, 104], (ii) the loosely-bound polaron pair model (PP) [100, 105, 106], (iii) the triplet-exciton polaron quenching model (TPQ) [107, 108], and (iv) the different gyromagnetic factor mechanism [109, 110].

Although there have been different models, explaining the whole cases of organic magnetoresistive response uniformly has to date not been achieved within a single model.

2.4.5.1 Magnetic field sensing using MEH-PPV

Poly[2-methoxy, 5-(2'-ethyl-hexyloxy)-p-phenylene-vinylene] (MEH-PPV) is an inflexible conjugated polymer and soluble in some organic solvents such as toluene and hexane, and a popular conducting semiconductor, which is used in many optoelectronic devices including LEDs, organic solar cells and for the optical-magnetic information transduction [111, 112, 113].

Moreover, MEH-PPV with low cost is interesting to organic-based magnetometers industries, thus can be used for magnetic field measurements. W. Baker in ref. [16] proposed device of thin MEH-PPV layer (200 nm) between PEDOT with 50 nm thickness as a hole injection layer and cathode layer consists of 25 nm Ca and 50 nm Al. the conductivity of this device can be determined when the spin polaron pair decay into excitons in the organic layer, and that allows magnetic resonance in an electron or hole to be detected.
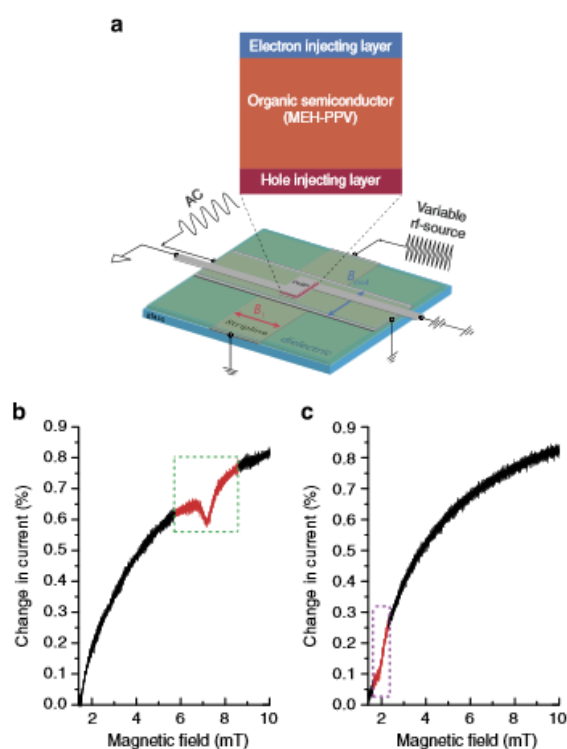
Figure 2.11: Device concept of the magnetic resonance-based magnetometer of an organic semiconductor, taken from [16]. Reproduced from W. J. Baker, K. Ambal, D. P. Waters, R. Baarda, H. Morishita, K. van Schooten, D. R. McCamey, J. M. Lupton, and C. Boehme, "Robust absolute magnetometry with organic thin-film devices", Nature Communications 3, 898 (2012).

Figure 2.11 reveals the principal scheme (case a) of the device proposed in ref. [16] and shows the response of the magnetic field to a DC current without modulation in the presented bipolar MEH-PPV diode as a function of magnetic field with radio frequencies equal to 200 MHz in the case b, and to 50 MHz in the case c). The relative current changes in the highlighted rectangles correspond to the MR-induced charge change, when the spin dynamics of the charge carrier ensembles is changing, too.

Since the method allows one to measure the MR-induced spin-mixing rate changes, the limitations of these measurements will affect the magnetic detection. Therefore, the lower limit of the magnetic field B_0, which can be measured by the proposed device is determined by the simple condition – B_0, should exceed the local hyperfine field of the π-conjugated polymer. Conversely, when B_0 is smaller than the hyperfine field, the spin mixing is too fast to be detected by MR and the EDMR signal from that mixing disappears [16].

The application of the MEH-PPV for the organic-based MR magnetometry strongly reduces the cost of the experimental setup. Moreover, this device does not require calibration, temperature changes, can be used over large magnetic field and temperature ranges, and has high precision and absolute sensitivity values (for the fields less than 100 mT, the resolution is equal to 50 nT $Hz^{-1/2}$). However, this organic magnetometer can detect only the fields larger than 1 mT, has less sensitivity than SQUIDs, and meet some challenges mostly connected with the increased time of MR reference frequency searching [16].

Since the organic semiconductors have promising applications for the OLED-based magnetometers production, the research of spin-orbit coupling effects [114] as well as other spin-based phenomena [115] in them, continue to attract attention.

2.5 Spins in organic systems

Spin quantum mechanical properties are significantly impacting organic electronic materials due to the generation, mobility, and recombination of charge carriers. The significant interest in spin manipulation based probe, due to the week spin-orbit coupling, which leads to Pauli blockade (which impacts conductivity) and long coherence times (which impacts recombination),is to understand the underlying electronic features in these materials and develop new technological applications [15, 16].

Magnetic field effects are related to polaron pairs, biplarons, triplet-exciton polaron complexes, and triplet-triplet complexes, although the spin dynamics explanations still complicated in organic materials. In order to understand that, it is important to define spin-dependent and independent processes in organic devices [5].

Next sections will provide a brief explanation of the main excitations processes in organic devices.

2.5.1 Excitations processes in organic devices

2.5.1.1 Polarons

The strong interaction between charge carriers and the nuclei surrounding in the organic materials introduces polarons with spin ½ and unit charge. The mobility and the conductivity of the charge carriers are reduced due to that strong interaction.

The Hamiltonian below can be used to describe electron and hole polarons:

$$H_{SSH} = \sum_{n,\sigma} [-t_0 + \alpha(u_{n+1} - u_n)][c^+_{n+1,\sigma} c_{n,\sigma} + c^+_{n,\sigma} c_{n+1,\sigma}]$$

$$+ \sum_n \frac{p_n^2}{2m} + \frac{1}{2} K \sum_n (u_{n+1} - u_n)^2 \tag{2.70}$$

Here the first term represents: electron hopping, the second term: nuclear kinetic energy, and the last term: nuclear potential energy, where t_0 is the transfer integral, α and K are spring constants, u, p and m are the nuclei position, momentum and mass, and c and c^+ are the annihilation and creation operators for the polarons. The first summation refers to the electron hopping, the second one is nuclear kinetic energy, the last term is nuclear potential energy.

Describing the formation and dissociation of higher spin particles like excitons, polaron pairs, and solitons is achieved with the SSH Hamiltonian models, while latest models for p-EDMR and p-ODMR concentrate on uncoupled spins [5].

2.5.1.2 Polaron pairs

Polaron pairs with bounded state and weak spin interaction are formed by two polarons with opposite charges.

$$e + h \rightarrow [e + h] \tag{2.71}$$

where e and h are the polarons electron and hole respectively, and $[e + h]$ refers to a coulombically bound state.

Polaron pairs can dissociate back to a free electron and hole as in:

$$[e + h] \rightarrow e + h \tag{2.72}$$

or create a strongly-bound exciton which recombines quickly as:

$$[e + h] \rightarrow S \qquad \text{or} \qquad [e + h] \rightarrow T \qquad\qquad (2.73)$$

where S and T is singlet and triplet exciton respectively.

An external magnetic field has the ability to influence transitions or spin mixing between the singlet and triplet manifolds before spin-dependent recombination or dissociation. The bases of the transition rate are the strength of the magnetic field, the weak coupling (exchange and dipolar) between polarons pair, and moreover, strong coupling to the external environment.

From spin mixing rate, spin dependent current contribution is provided by spin dependent reaction yield, where the singlet and triplet are different in the probabilities of dissociation and recombination. It can be provided also by spin dependent reaction rate where the singlet and triplet have the same probabilities, while the constant rates are different [5].

2.5.1.3.Exciton

When an electron-hole (exchange-coupled) pair is strongly bounded, it is called an exciton [5]. Producing excitons in organic devices occurs when positive and negative charge carriers encounter each other, while the decay to the uncharged ground state results from radiative recombination [4].
The recombination of singlet excitons occurs on nanosecond timescales, and the separation of them would be around 5-20 nm during that time. However, triplet excitons stay to milliseconds and separate between 10 to 250 nm [4, 5].

2.5.1.4 Bipolarons

Two polarons with the same polarity can combine to create a bipolaron, which has similar position and weakly spin coupled charges.

$$p + p \rightarrow [p + p] \qquad\qquad (2.74)$$

where p is either a positive or negative polaron, and can integrate to a singlet bipolaron only because of great exchange interaction as:

$$[p + p] \rightarrow S^{++/--} \qquad\qquad (2.75)$$

Although they have short lifetimes [5], bipolarons still generate magnetic field effects and have action like polaron pairs [5].

2.5.1.5 Triplet-exciton polaron complex

A triplet-exciton polaron complex can occur when a triplet-exciton is coupled to a polaron, which then will have three spin ½ particles.

$$T + p \rightarrow [T + p] \qquad (2.76)$$
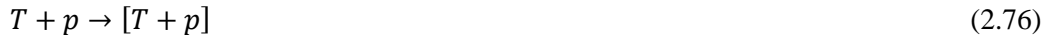
And when the complex is dissociated, it can be written as:

$$[T + p] \rightarrow T + p \qquad (2.77)$$

Unless there is a doublet content in the spin state which result in destroy the complex and provide polaron in excited state [5]. The conductivity can change after the exciton reaches the ground state and transfer its energy to the polaron.

$$T + p] \rightarrow S_0 + p^* \qquad (2.78)$$

2.5.1.6 Triplet-triplet complex

T. Keevers presented in his thesis [5] the two triplet- excitons combine, which gives a triplet-triplet complex.

$$T + T \rightarrow [T + T] \qquad (2.79)$$

And when the complex is dissociated into a pair of triplets, it can be written as:

$$[T + T] \rightarrow T + T \qquad (2.80)$$

Unless the total wavefunction is spin 0, then the complex annihilates and provides a two singlet excitons [5]

$$[T + T] \rightarrow S_0 + S_1 \qquad (2.81)$$

2.5.2 Spin dependent processes

In organic materials, static magnetic field and magnetic resonance impact on spin states and then spin dependent rates which lead to have magnetoresistance and magneto luminescence [4].

From the excitations processes discussed above, exciton is the most important spin dependent states in organic materials. Exciton provides a spin 1 system (from electron spin =1/2 and hole spin =1/2), which come out with four possible spin eigenstates, one singlet and three triplet states. Singlet decay is mainly

cause of producing light in organic materials because radiative triplet decay is negligible for some reasons. Therefore, the spin of the charge carriers is fundamental for the internal quantum efficiency in organic devices because of the conservation of electronic spin in exciton formation and decay. Thus, polaron pair formation model is principle of many electrical and optical applications in organic semiconductors, since it has the ability to manipulate spins with magnetic resonance which resulted in conductivity and fluorescence impacts, and through EDMR and ODMR experiments, obtaining the physical parameters of the spin states [4].

Next is the bipolaron pair model, which as explained previously is formed from either electron-electron or hole-hole pairs only. Spin-dependent conductivity "which is obtained due to the pair formation leads to increase hopping mobility of the charge carriers" [4] and magnetoresistance contribution have been effective by bipolaron pairs.

In short, polaron pair formation and bipolaron pair models are different in fundamental physics but have similar behavior. Importantly, using EDMR and ODMR experiments to analyze some spin dependent processes such as spin-dependent scattering, spin trapping, spin polarization, and intermediate pair processes showed that signals of all pair processes are strongly spin-polarization dependent, thus the observation of these processes under some condition is complex. However, the intermediate pair processes are spin polarization independent, and polaron pair formation and bipolaron pair models are important examples [4].

2.5.3 Spin independent processes

Detecting and analyzing spin independent processes are impossible with magnetoconductance or EDMR spectroscopy because the overall reaction yield will not be affected by changing spin mixing rate. Therefore, these processes would be determined by device design or condition operation. The demand for spin independent processes is concentrated in developing an accurate microscopic picture. Changing the charge carrier density, or providing a compatible/ competitive pathway by spin independent processes would lead to effect spin dependent processes certainly.

Next sections will provide a brief explanation of the main spin independent processes in organic materials [5].

2.5.3.1 Singlet-exciton polaron quenching

A singlet-exciton annihilation or polaron dissociation would be consisted in this process. Both annihilation and dissociation lead to expand the sample conductivity by increasing the mobility (annihilation process) and the density (dissociation process) of the average charge carriers.

$$S_1 + p^{+/-} \rightarrow S_0 + p^{+/-*} + phonon \tag{2.82}$$

$$S_1 + p^{+/-} \rightarrow p^{+/-} + p^+ + p^- + phonon \tag{2.83}$$

where S_1 is the first singlet exciton state, S_0 is the ground singlet exciton state, $p^{+/-}$ is a positive/negative polaron, and * refers to excited state [5].

2.5.3.2 Singlet –singlet annihilation

In this process two singlet-exciton annihilations would be involved producing a singlet-exciton in the second excited state (S_2).

$$S_1 + S_1 \rightarrow S_0 + S_2 \tag{2.84}$$

The sample conductivity would not be impact in this process, while some other relative processes might increase [5].

2.5.3.3 Singlet-exciton triplet-exciton annihilation

This process produces singlet-exciton annihilation and triplet-exciton excitation.

$$S_1 + T_0 \rightarrow S_0 + T_1 + phonon \tag{2.85}$$

where S and T refer to singlet and triplet exciton respectively [5].

2.5.3.4 Singlet-exciton bipolaron quenching

Recombining and transferring a singlet-exciton's energy to bipolaron is the basement of this process.

$$S_1 + bp^{++/--} \rightarrow S_0 + bp^{++/--*} + phonon \tag{2.86}$$
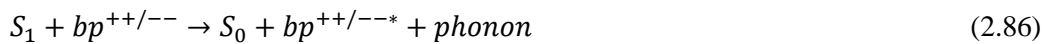
where bp is the bipolaron state.

The sample conductivity here is expanding due to increasing the mobility of the average charge carriers [5].

2.5.3.5 Singlet fission

In this process, as T. Keevers presented, recombination of two singlet states would provide two triplet-excitons, which is basically the inverse process of triplet-triplet annihilation mentioned in section 2.5.1.6

$$S_0 + S_1 \rightarrow T_1 + T_1 \tag{2.87}$$

Increasing the sample conductivity in this process would be occurred by increasing in some relative processes such as triplet exciton polaron quenching and triplet-triplet annihilation [5].

2.6 Organic devices

Low cost, flexibility, low density and potentially high throughput, and the low cost of processing organic materials have led to a range of organic electronics technologies. Due to the intriguing properties of organic materials, especially organic semiconductors, these materials have been identified as suitable for developing optoelectronic technologies which require properties such weak spin-orbit coupling, long spin coherence times and large magnetic field effects at room temperature [5].

The next following sections will introduce organic light-emitting diodes (OLED), concentrating on OLED design and structure, operation and measuring the efficiency of OLED, and some challenges and applications of OLED [116].

2.6.1 OLED design and structure

The first OLEDs with a luminance of over $1000 \frac{Cd}{m^2}$ at voltages $\approx 10 \, Volt$ were developed by Tang and Van Slyke in 1987. Using two-layers with a separate hole and an electron transporting layers was the basic format of the diode, where increasing the efficiency and decreasing the voltage were the effects [3, 26]. Between 1990s and 2000s, the OLEDs have become the future technology because of improved understanding of phosphorescent OLEDs (PHOLEDs) with power efficiency over $100 \, lm/W$ [116].
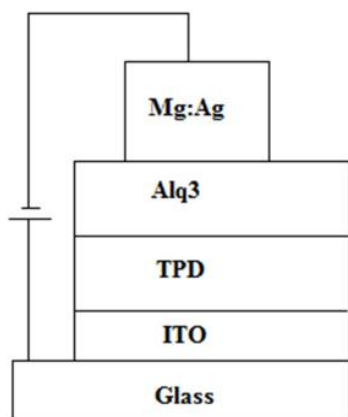
Figure 2.12: First OLED's device structure by Tang and Van Slyke [116]. Reproduced from M.Cai, "Organic Light-Emitting Diodes (OLEDs) and Optically-Detected Magnetic Resonance (ODMR) studies on organic materials", (2011).

There are two types of OLEDs based on small molecules (with low "molecular weights") and polymers ("large molecules with repeating structural unit"): small molecule OLEDs (SMOLEDs) and polymer OLEDs (PLEDs).

The thermal evaporation in a vacuum is required in order to fabricate SMOLEDs. The ability of the vacuum deposition process leads to preform high flexible multilayer with well controlled and homogeneous films, thus charge transporting and blocking layers would be performed and high efficiency provided. The limitations of this process refer to the difficulty and high cost.

Fabrication of PLEDs can exploit potentially cheaper and simpler techniques like spin-coating, inkjet printing, and screen printing. The production efficiency is small compared to that in SMOLED [116].

The development of OLED technology leads to increase the complexity of OLEDs structure. Given SMOLEDs as an example to discuss OLEDs structure, the multilayers here have seven different organic layers (the total thickness of the layers in the OLEDs usually is $\sim 100\ nm$) between two electrons as it shown in fig. 2.13. [37].
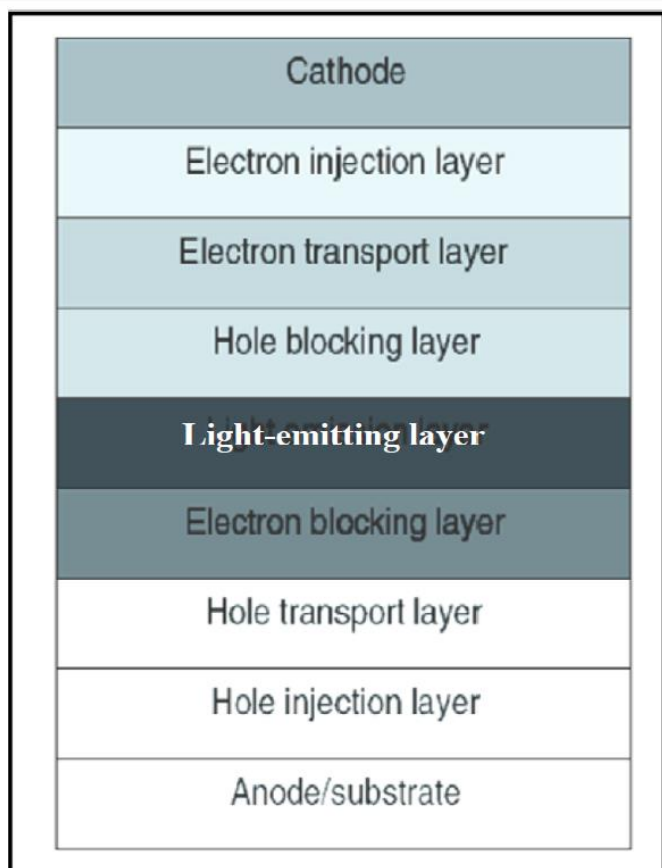
Figure 2.13: The structure of SMOLEDs (seven multilayers) [116]. Reproduced from M.Cai, "Organic Light-Emitting Diodes (OLEDs) and Optically-Detected Magnetic Resonance (ODMR) studies on organic materials", (2011).

The electron/hole transport layer (ETL/HTL) transfers the injected electron/hole to the light emitting layer (EML) "recombination area" by decreasing barrier and charge injection. In the electron/hole blocking layer (EBL/HBL), the electron/hole charges are preventing from being extended to the other electrode, and then holding to light emitting layer (EML). In the light emitting layer (EML), light is produced due to the electron and hole recombination, which is happened because the length of the exciton diffusion is $\sim 10 \ nm$. It is possible to have different color of OLEDs by replacing the emitter materials. Most of classical OLEDs are bottom-emitting, emitting light from substrate and bottom electrode which are transparent or semi- transparent. However, Top-emitting OLEDs will be emitting light through the transparent or semi-transparent top electrode. In addition, transparent or semi-transparent top electrode in OLEDs would have significant effects on increasing contrast and providing clear image. Moreover, connecting some OLEDs as a series will improve the efficiency which leads to increase lifetime, while an expensive cost keeps it limited [116, 117].

2.6.2 OLED operation

The operation of the OLEDs is basically providing the process of electrons and holes movement separately from cathode to anode after applying a voltage, then transforming them into each OLEDs layers [116]. Note that the operating lifetime is an important feature of OLEDs performance [118]. In the EML, where the exciton occurred, the spin wavefunction can be either singlet (S=0) or triplet (S=1), then the difference of the energy level between singlet and triplet would be big. The light emission (fluorescence) is produced only by singlet excitons, while triplet excitons do not [119]. Importantly, light emitting is controlled by charge (electron) injection, transport, and recombination. Since there is no free charge carriers, device efficiency would be effective by incapable injection and extraction of charge [116]. The internal quantum efficiency is given by:

$$\eta_{int} = \gamma r_{sr} q \qquad (2.88)$$

where γ is the ratio of the number of exciton formation happens within the device to the number of electrons following in the external circuit (charge balancing) , r_{sr} is the fraction of excitons(recombination), and q is the efficiency of radiative decay of single excitons (radiative emission) [119].

The charge injection and charge transport processes are extremely connected. The injection process is controlled by charge injection barriers which have been effective between active layers and metal electrodes [116]. Injection barriers cannot be estimate easily from the work function of the metal electrode and the highest and lowest occupied molecular orbitals (HOMO) (LUMO) due to the deviations from chemical reactions between metal and semiconductor. The current flow is limited by the injection of charge in devices with large barriers charge injection [116, 119].

In the recombination charge process which was described earlier, lower mobility of one charge carrier than the other is required in order to have high local charge density which leads to having high efficiency in the device's structure. The device of the photonic structure has an extreme impact on the efficiency of radiative decay. The internal quantum efficiency mentioned above has the necessary components to have favorable efficiency: Charge balancing can lead to high-efficiency. The recombination which has a 25% limitation due to the exciton formation provided one singlet and three triplet states; however, this does not included all devices at the present time. Finally, radiative emission from excitons has shown "under conditions measurements" reaches high-efficiency improvement can be occurred up to 50% [119].

2.6.3 Challenges and applications of OLED

OLED technology has been expanded dramatically recent years. However, as any other technologies, OLEDs have some challenges such as cost, water damage, and limited lifespan of the devices. Moreover, as known before, the efficiency of most OLEDs is high except of blue OLEDs, which particularly have low efficiency and short lifespan.

The improvement of OLEDs technology has led to many applications such as flat-panel displays and solid-state lighting. Flat-panel displays have been divided to large screens as TVs and small screens such as mobile phone, digital cameras, and car radios. Also, using high light produced from OLEDs is significant for sunlight reading. In solid-state lighting, more development with flexible lighting and signs has led to create for example OLED lighting samples [116].

Chapter 3. Methods-Device Fabrication

3.1 Organic device fabrication

3.1.1 Principle of Operation

As mentioned previously in chapter 2, organic light emitting diode (OLED) in general contains seven layers as seen in the fig. 3.1, the principle of OLED can be started with electron injected from cathode and hole from anode as applied particular voltage in between. In between, there are transport layers. Injection processes format is particularly affected by the difference between HOMO, LUMO and electrodes. In the emitting layer, either excited molecules or exciton are generated which lead to electrons-holes recombination which emit light as the concentration distribution of the exciton moves from high to low [120].

The photon diffusion either emitting light through the glass or returning back to cathode and converted energy to heat or transferred [120].
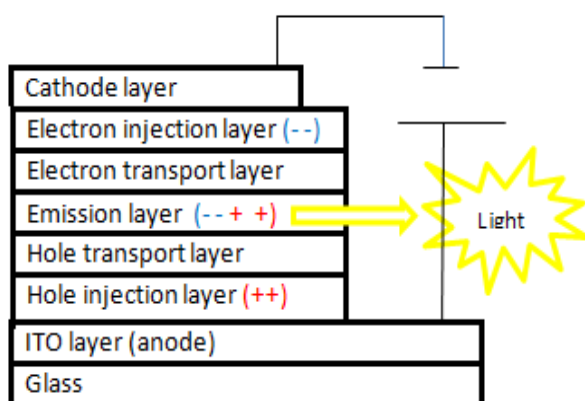
Figure 3.1: The seven layers of an OLED.
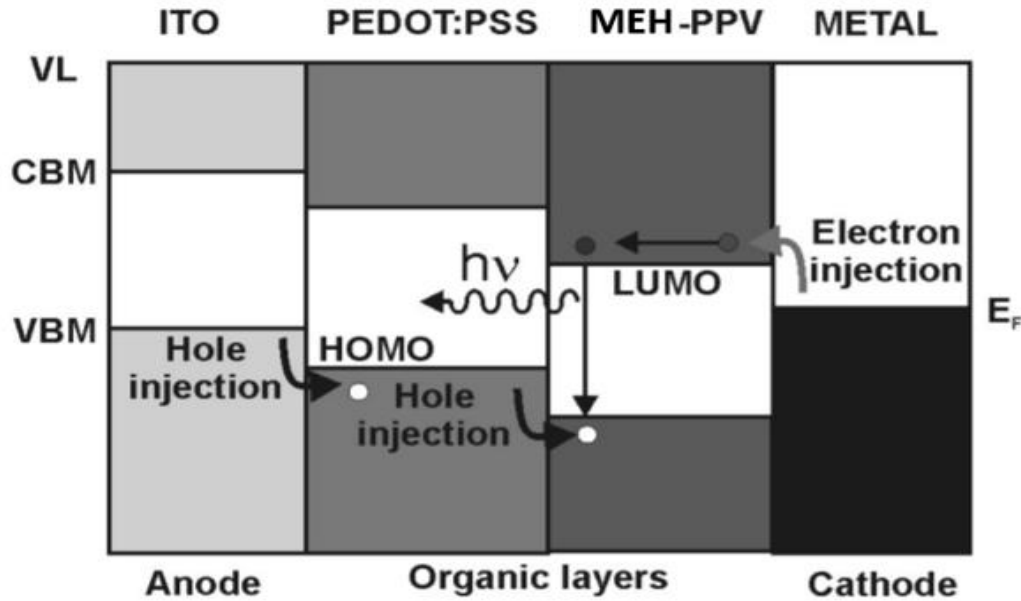
Figure 3.2: A schematic shows the principle work of OLED's bilayers [121]. Reproduced from H. A. Méndez-Pinzón, D. R. Pardo-Pardo, J. P. Cuéllar-Alvarado, J. C. Salcedo-Reyes, R. Vera, and B. Páez-Sierra, "Analysis of the Current-Voltage Characteristics of Polymer-Based Organic Light-Emitting Diodes (OLEDs) Deposited by Spin Coating", Universitas Scientiarum, Vol. 15, no. 1, Jan. pp. 68-76, doi:10.11144/javeriana.SC15-1.aotc (2010).

By looking at fig. 3.2, the device would have bipolar conduction by electrons and holes injection. However, if the different between LUMO and Fermi energy level is high or above 1eV, electron injection is little, then the device has unipolar conduction. Also, the different between HOMO and valence band can be reduced by increasing hole injection, therefore PEDOT: PSS is used for hole injection development [121].

3.1.2 OLED Fabrication processes:

1) Cleaning:

The first step of OLED's devices fabrication is to ensure clean glass substrates (dimensions 70 mm x 3 mm). In fact, there are several steps for cleaning a substrate, started by using UV for 15min, followed by acetone (10 mins), isopropanol (10 mins), distilled water and ultrasonic bathed. After that, baked it overnight, and prepared for spin coating [120].

2) Spin coating:

Before moving to spin coating, device structure as in fig. 3.3 is needed, so the indium tin oxide (ITO) of the substrate is between 100-150 nm, then the PEDOT:PSS 40nm, then MEH-PPV layer between 100-150nm (MEH-PPV), after that 10 nm of calcium ,to ensure good electron injection, and at last 100nm of aluminium [120]. PEDOT: PSS is provided by Heraeus and MEH-PPV by Luminescence Technology Corp and made with toluene.

Thus, the glass is spin coating with PEDOT: PSS at different spin coating speed as seen in table 3.1 for 60s, then the sample has placed on hot plate for 12 hours at 100 °C to ensure the solvent is totally evaporated. After that, MEH-PPV is spin coating with also different spin coating speed for 60s, then place the sample on hot plate for overnight at 60 °C. As seen in fig. 3.4 the PEDOT:PSS and MEH-PPV should be applied on shaded part, but due to lack of spin coating control, it will cover up to lined part [120].
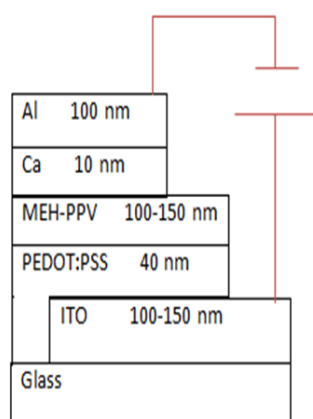
Figure 3.3: OLED device structure.
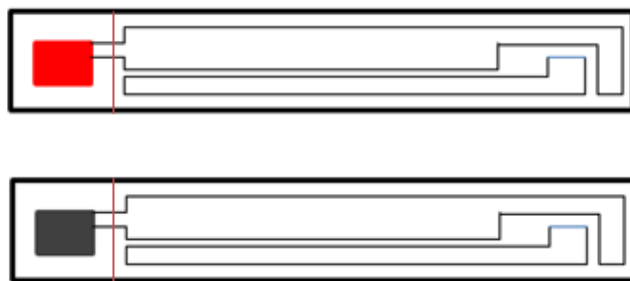
Figure 3.4: Two substrates show the area that PEDOT: PSS (black shaded) and MEH-PPV (red shaded) should be applied and the lined area where both practically been applied.
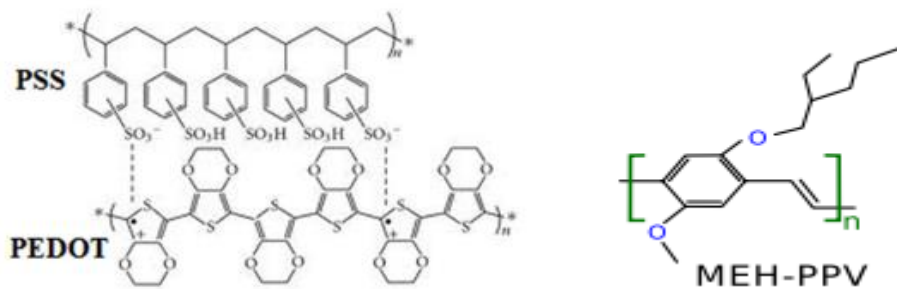
Figure 3.5: PEDOT: PSS and MEH-PPV chemical structure [116, 122].

3) Thermal evaporation:

During thermal evaporation, the efficiency is high enough to provide high flexible multilayer with well controlled and homogeneous films due to the vacuum deposition capability. As mentioned before in chapter 2, the limitations of this process refer to the difficulty and high cost [116]

In thermal evaporation, shadow mask with top cover as in shaded area in fig. 3.6 has been used in order to hold the substrates which been faced up. After that, the mask has been flipped in order to deposit Ca/Al on top of MEH-PPV layer at room temperature [120].

Then the device is applied voltage in the range between 5v-15v after been connected. The light is emitting from the bottom of the device as most of OLEDs [120].

Figure 3.6: A substrate after deposited Ca/Al.

In order to keep the device stable during the measurement, I designed a sample holder and printed in the School of Physics at UNSW as seen in fig 3.7 below.
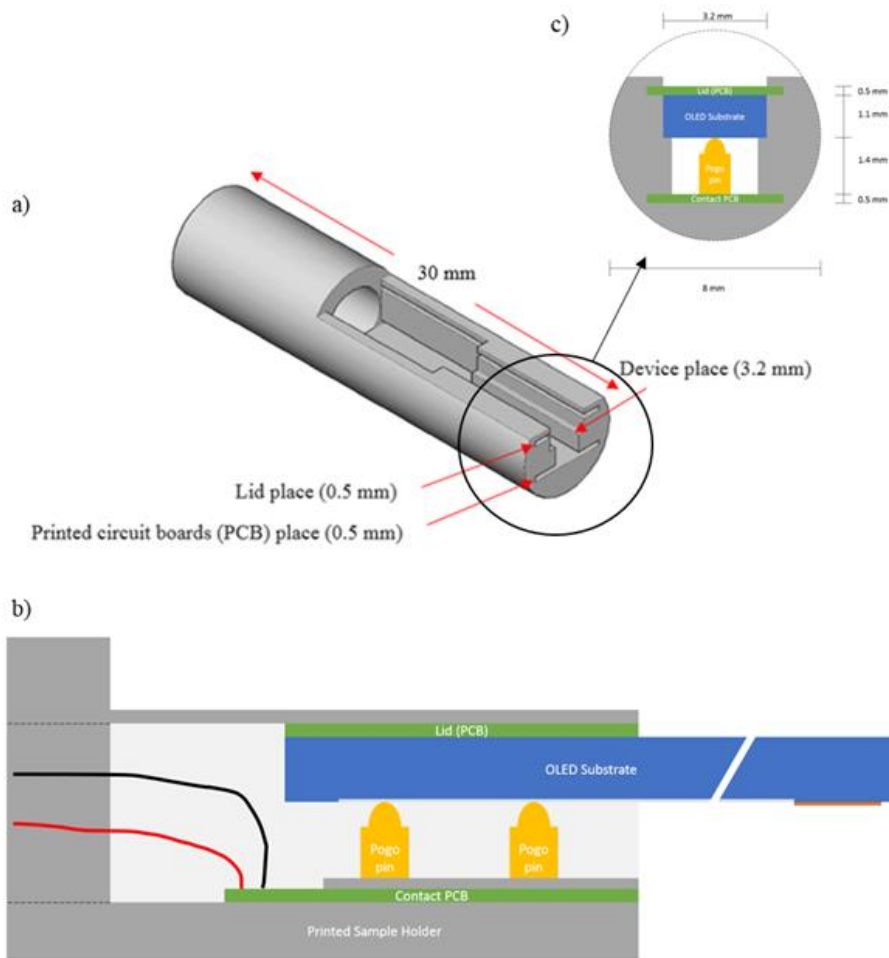
Figure 3.7 A sketch of the sample holder developed during the course of this thesis. The sample holder is 3D printed and provides secure support and well-defined placement, which enables high quality electrical contacts to the device via pogo pins. The holder is attached to the end of a standard EPR sample tube, through which electrical wiring is run to all sample measurement in the resonator.

The sample holder shown in Fig. 3.7 is a single piece with contact pads, and has a number of benefits over previous designs. These advantages include:

- It removes the challenges associated with the very small and often magnetic screws used in previous designs, whilst providing simpler assembly.

- It can be modified easily due to its fabrication via 3D printing, whilst retaining stable sample positioning during electrical measurements

- It has proven to facilitate good electrical contact at low temperature.
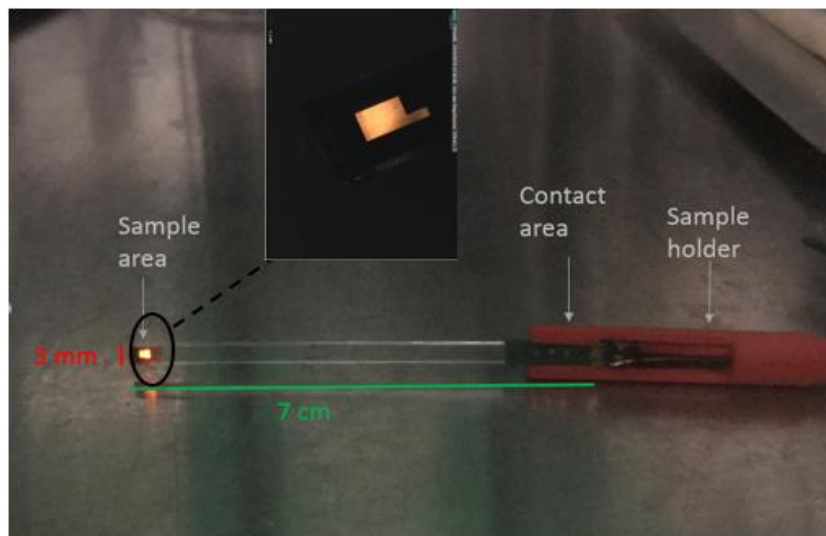
a)   b)

Figure 3.8: a) Photo of OLED device held by EDMR sample holder b) Photo of OLED device encapsulated inside an MD5 EPR tube.

3.2 Device characterization

In OLED's fabrication, two main cases have been considered:

    A. Spin coating PEDOT:PSS inside glovebox which included two incidents:

        1) Different spin coating speed for both PEDOT: PSS and MEH-PPV

        2) Different concentrations of the solution (MEH-PPV)

    B. Spin coating PEDOT:PSS outside glovebox

        1) Different solutions with same concentration

        2) Different cathode layers

A. Spin coating PEDOT:PSS inside glovebox which included two incidents:

3.2.1 Different spin coating speed for both PEDOT: PSS and MEH-PPV

For spin coating PEDOT: PSS inside the glovebox within same MEH-PPV solution concentration (15mg/ml, made with toluene) and different spin coating speeds for both PEDOT:PSS and MEH-PPV, as seen in table 3.1

PEDOT:PSS	MEH_PPV
2000 rpm	800 rpm
2000 rpm	900 rpm
2000 rpm	1000 rpm
3000 rpm	900 rpm
3000 rpm	1000 rpm
3000 rpm	2000 rpm
3000 rpm	3000 rpm

Table 3.1: Different spin speeds for both PEDOT: PSS and MEH-PPV have been used to make OLED's devices.

a)
b)
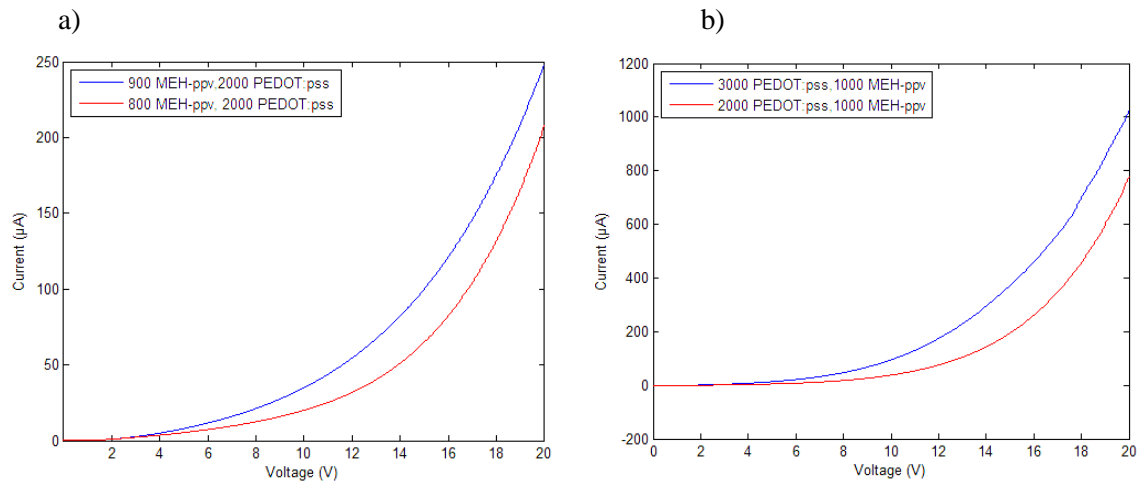
Figure 3.9: Current-voltage (I-V) characteristics of OLED's with different spin coating speeds for both MEH-PPV and PEDOT: PSS

   a. Compare different MEH-PPV active layer with same PEDOT: PSS spin coating speed 2000 RPM

   b. Compare different PEDOT: PSS with same MEH-PPV 1000 RPM

It is clear from Fig. 3.9 that with different spin coating speeds has a reasonable impact on device performance. Increasing spin coating speed leads to a decrease in the thickness of the (film) active layer MEH-PPV or PEDOT: PSS and an increase in the current. Observing higher slopes indicate lower overall ohmic resistances in these devices which implies an increase in pinholes density in thinner films [67, 121]. Because the pinholes are critical to defining the axial and transverse resolutions of the

devices, which affect the light emission of the devices too, higher pinhole density is extended the parasitic currents and short circuit between cathode and anode which affected the device performance [121, 123].

3.2.2 Different concentrations of the solution (MEH-PPV)

From the different spin coating speeds results above, 3000 rpm for both PEDOT: PSS and MEH-PPV has been chosen to be used for all next device fabrication processes. Therefore, within that case, different concentrations of MEH-PPV solution has considered. Note that the MEH-PPV solution here is made with toluene only. Fig 3.10 shows comparison between two groups of devices, both within 3000 rpm for PEDOT:PPV and MEH-PPV, but with different MEH-PPV solution concentrations: 10 mg/ml and 15 mg/ml. Devices average has been taken in each group for better result.

a)   b)
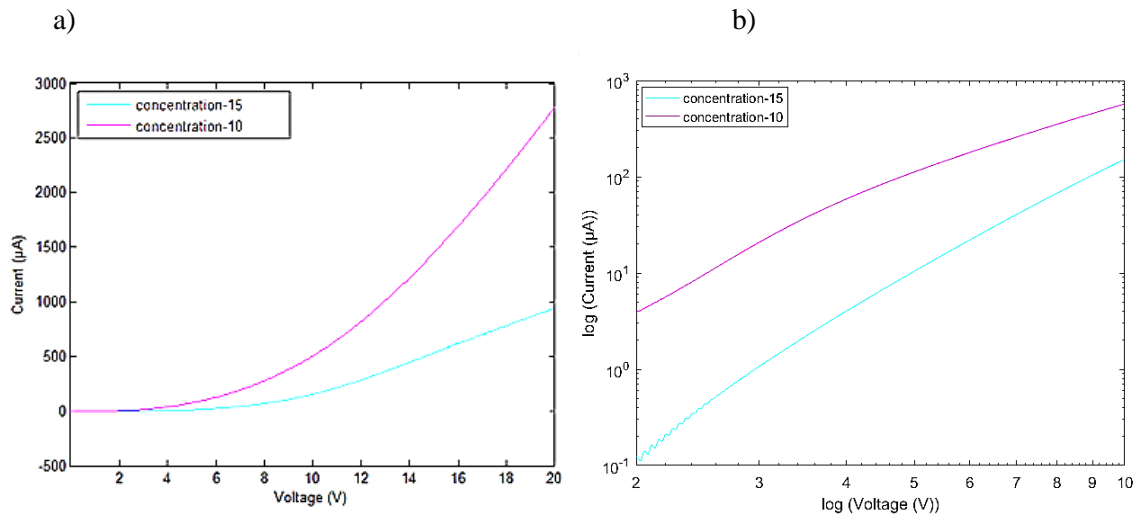
Figure 3.10: Current-voltage (I-V) characteristics of averaged devices with different MEH-PPV solution concentrations and same spin coating speed for both PEDOT: PSS and MEH-PPV.

    a.   Current-voltage (I-V) characteristics
    b.   Log (Current-voltage (I-V)) characteristics

From fig 3.10, the effective of different MEH-PPV solution concentrations is clearly observed, with higher current and lower voltage. Therefore, reducing the concentration of MEH-PPV solution leads to reduce the thickness of organic layer which increase current intensity and thus device performance.

In addition, using fresh MEH-PPV solution (less than one week old) indicates better result as seen in fig 3.11
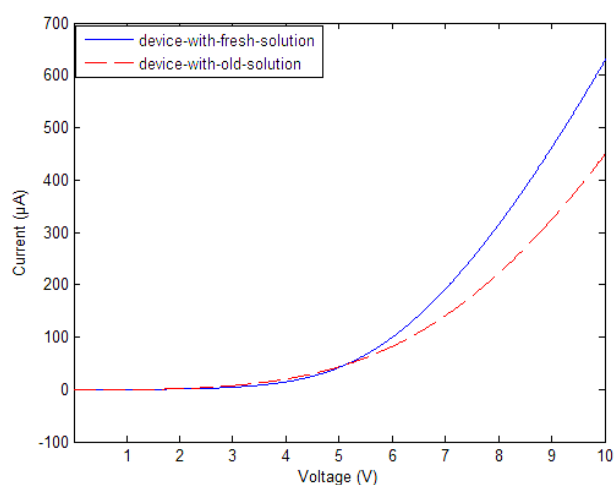
Figure 3.11: Current-voltage (I-V) characteristics of two with fresh and old MEH-PPV solution, same concentrations and same spin coating speed for both PEDOT: PSS and MEH-PPV, then deposit LiF, Ca, and Al.

Fig 3.11 shows comparison between two devices both made with same condition: PEDOT: PSS and MEH-PPV (10 mg/ml, 50% toluene, 50% cyclohexane) spin coating at 3000 RPM, followed by LiF (0.8 nm) at 0° C, Ca and Al at RT, except one made with fresh MEH-PPV solution while the other made solution that prepared 14 days before using it. It is clearly that the device made with fresh solution shows better result than made with old one.

From sections 3.2.1 and 3.2.2 we realized that decreasing the absorption of organic layer and increasing the current intensity both can be reached by reducing the thickness and increasing electroluminescence. The best result of OLED's device with higher current intensity performance at low voltage is achieved when the thickness reduction of electroluminescence layer occurred by increasing the spin coating and/or decreasing the concentration of MEH-PPV solution.

  B. Spin coating PEDOT: PSS outside glovebox

Before moving to different solutions with same concentration, it is critical to compare between spin coating inside and outside under same conditions: PEDOT: PSS and MEH-PPV spin coating speed 3000 RPM, and MEH-PPV solution 10 mg/ml made with toluene only. It can been easily seen from fig 3.12 that spin coating PEDOT: PSS outside the glovebox has higher current intensity at lower voltage compare to inside.
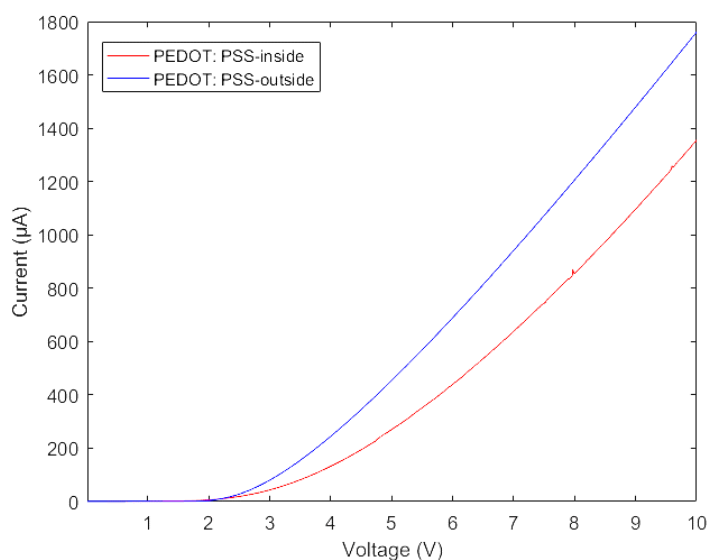
Figure 3.12: Current-voltage (I-V) characteristics of two devices: one with PEDOT: PSS spin coating inside and the other outside the glovebox, both with same MEH-PPV solution concentration and 3000 RPM spin coating speed for PEDOT: PSS and MEH-PPV.

3.2.3 Different solutions with same concentration

For spin coating PEDOT: PSS outside the glovebox within same spin coating speed as MEH-ppv (3000 RPM), and different MEH-PPV solutions: one has made with toluene only and the second with 50% toluene and 50% cyclohexane, both with same concentration (10 mg/ml). The effective of different types of MEH-PPV solution is realized in fig3.13
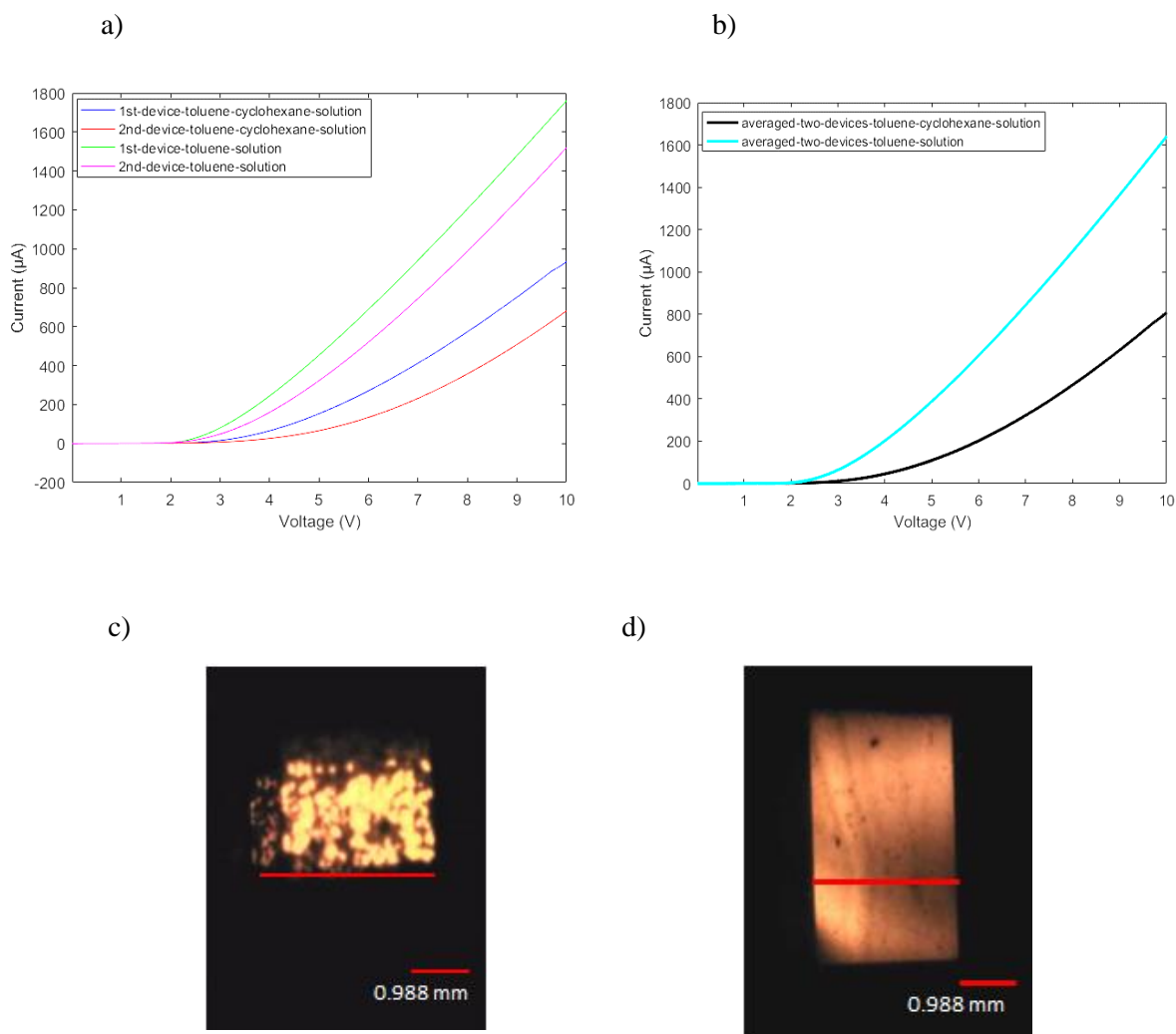
Figure 3.13 The effect of two types of MEH-PPV solution (1.with toluene only, 2. with 50% toluene and 50% cyclohexane) on devices within same solution concentration (10mg/ml) and spin coating speed 3000 RPM for both PEDOT: PSS and MEH-PPV

a) Current-voltage (I-V) characteristics of devices: two with different kinds of solution, both with same concentration and 3000 RPM spin coating speed for PEDOT: PSS and MEH-PPV.

b) Averaged of a).

c) Pixel of OLED device made with 50% toluene and 50% cyclohexane solution.

d) Pixel of OLED device made with 100% toluene solution

From Fig 3.13, higher current intensity has observed at lower voltage on the devices that were made with toluene only compared to the 50% toluene: 50% cyclohexane solution, which lead to increased performance of these devices. Closely look at fig3.13 c) and d) 100 µA with different voltages applied on both OLED's devices, and it is clearly seen that with MEH-PPV solution made with toluene only has almost full pixel producing light, although 50 %toluene and 50% cyclohexane solution presenting more brighter. The dark spots in both devices might be refer to the level of oxygen inside the glovebox which would affect the calcium layer in OLED's devices.

3.2.4 Different cathode layers

In this part we will illustrate different cathode layers by taking the advantage of the brightness of MEH-PPV solution made with 50% toluene and 50% cyclohexane, and 3000 RPM spin coating speed for MEH-PPV and PEDOT: PSS outside. The structure of OLEDs here is: PEDOT: PSS, MEH-PPV 10 mg/ml solution (made with 50%toluene and 50% cyclohexane), then deposit Lithium Fluoride (LiF) with 0.8 nm thickness, Calcium (Ca) 10 nm, and finally Aluminium (Al) 100 nm all at room temperature. The device structure band of principle work in OLED and the thickness are shown in fig 3.14 and 3.15 respectively. The I-V characteristic of this structure is shown in fig.3.16.
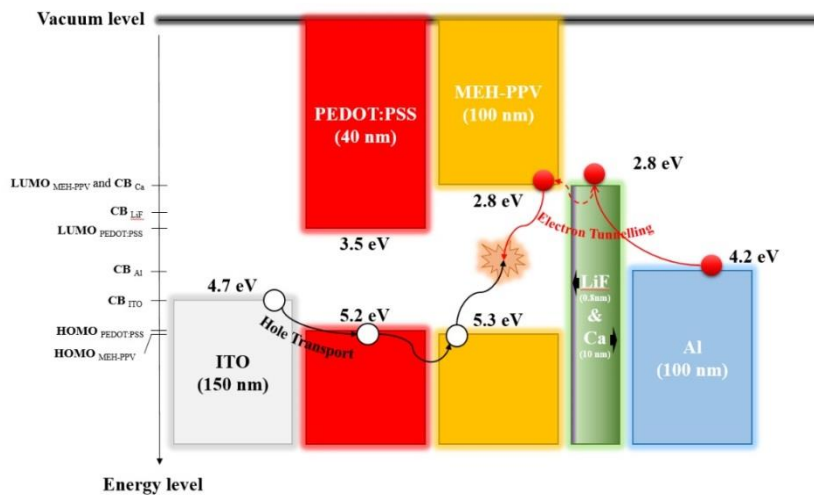
Figure 3.14: OLED device structure band.
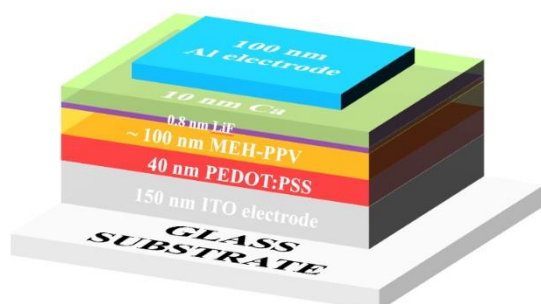
Figure 3.15: OLED device structure with thickness indicated.
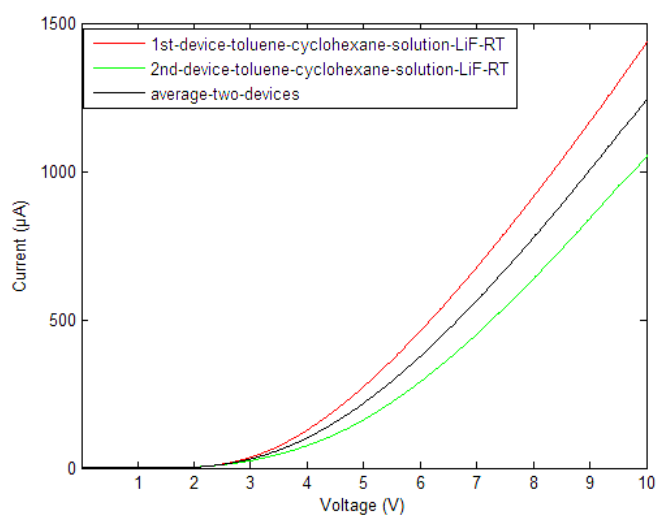
Figure 3.16: Current-voltage (I-V) characteristics of OLEDs devices with 3000 RPM spin coating speed for both PEDOT: PSS and MEH-PPV (50% toluene and 50% cyclohexane), LiF at RT, Ca, and Al.

Then compare that result to devices made with same conditions but without adding LiF layer, fig 3.17
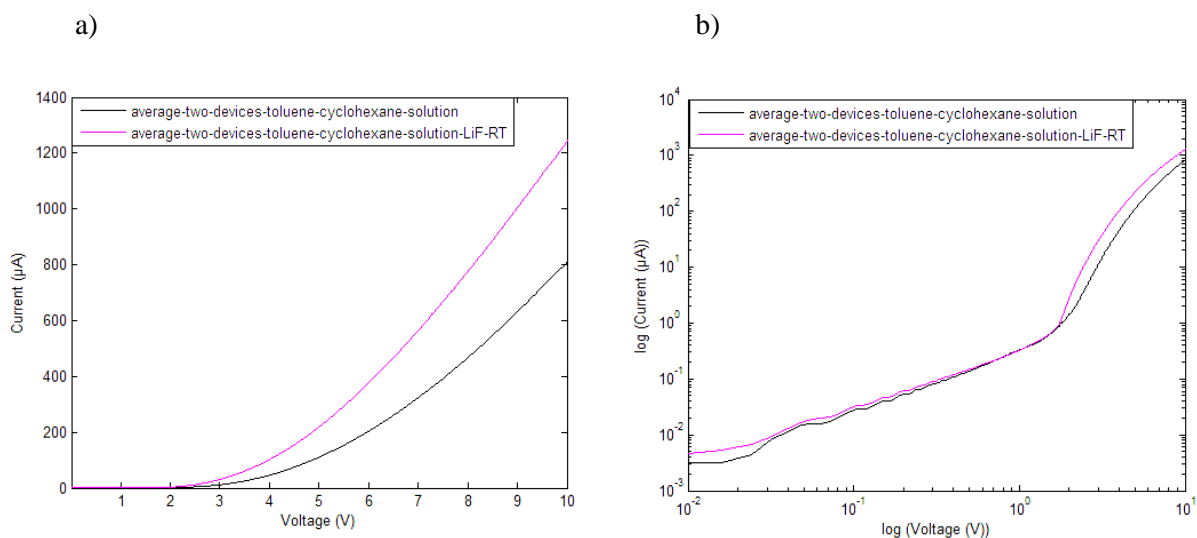
Figure 3.17: Comparing current-voltage (I-V) curves of OLEDs devices with 3000 RPM spin coating speed for both PEDOT: PSS and MEH-PPV (50% toluene and 50% cyclohexane), with and without adding LiF at RT, before Ca, and Al layers.

a. Current-voltage (I-V) characteristics

b. Log (Current-voltage (I-V)) characteristics

It is clear from fig 3.16 that the current increasing gradually when the voltage approximately above 3V in devices with LiF layer, indicating lower resistance than the devices without LiF. This reveals that the devices without LiF layer have less electron injection than with LiF.

In fact, examine adding LiF with 0.8 nm thickness at 0° C instead of RT demonstrate better result than above as seen in fig 3.18, note that Ca and Al both deposit at RT in all cases.

a)
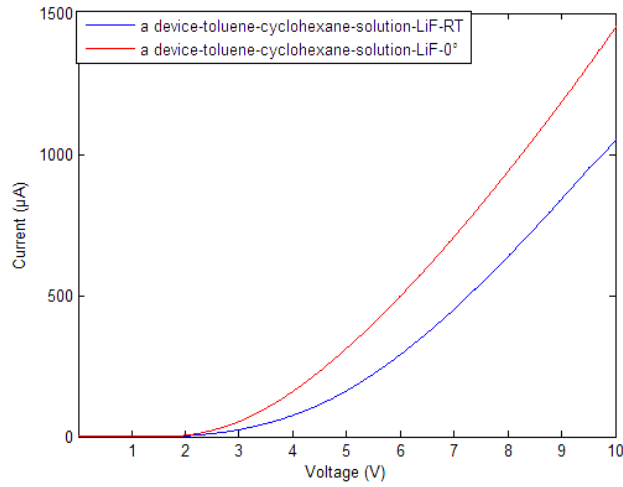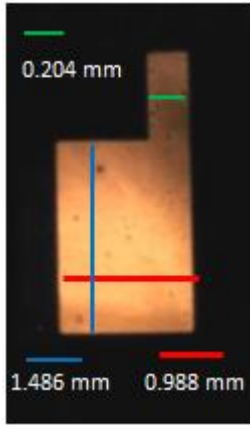
b)   c)   d)

Figure 3.18: Comparing current-voltage (I-V) curves of OLEDs devices with 3000 RPM spin coating speed for both PEDOT: PSS and MEH-ppv (50% toluene and 50% cyclohexane), with one LiF at RT and the other at 0° C , while Ca, and Al both at RT.

a) Current-voltage (I-V) characteristics.

b) Pixel of OLED device with deposit LiF layer at 0° C, when 2.5 V voltage applied at 100 µA.

c) Pixel of OLED device with deposit LiF layer at RT, when 3 V voltage applied at 100 µA.

d) Same device in c) but within increasing the current up to 0.5 mA.

From fig 3.18 a) lower resistance in device with LiF at 0° C indicates higher current at lower voltage compared to device in LiF at RT which enhance the performance of the device. Also, close looking to

fig 3.18 b), c), and d) shows clear and full pixel emission of OLED device in b) compare to c) and even after increasing the current as seen in d).

3.2.5 Conclusion:

Therefore, all the results of OLED's IV characterisation demonstrated above approved that the best device with higher current intensity at lower voltage, and full clear pixel light emission can be reached by 3000 RPM spin coating speed for both PEDOT: PSS and MEH-PPV fresh solution 10 mg/ml (50% toluene and 50% cyclohexane), deposit LiF (0.8 nm) at 0° C, while Ca (10 nm), and Al (100 nm) both at RT. Increasing the spin coating speed or decreasing MEH-PPV solution concentration leads to reduce the thickness which produces higher current intensity at lower voltage and lower resistance which can be connected with higher density of pinholes in theses organic layers. Producing parasitic currents route between cathode and anode due to higher pinholes density leads to increase the device performance with high emission. Devices made to this recipe will be used for measurements in the following chapter.

Chapter 4. Experimental determination of spin properties

Although organic semiconductors have been used for developing a variety of optoelectronic technologies, measuring spin coherence time has remained difficult in these materials. However, measuring spin coherent time allow important awareness to spin relaxation mechanism which is critical for spin dependent transport and recombination with high-level spin mixing included [15, 67].

In this thesis, puled EDMR has been used to drive spin singlet-triplet Rabi oscillation in order to manipulate spin coherent time in OLED. Changing the current through the device leads to determine spin recombination rate and that present spin control of electronic transport and spin coherent time over 0.5 µs [15, 67].

Due to the low atomic number of hydrocarbon atoms in organic semiconductors, weak spin orbit coupling indicate in these materials which would give the ability to transduce spin information into both optical and electrical signals [15, 16].

The observation of the coherent effects when the excitation time is longer than coherent time in organic devices is impossible by ESR technique due to quasi continue microwave fields limitation. To overcome with this issue and thus confirm that the microwave field duration time is shorter than spin excitation dephasing time, pulsed EDMR has used to allow spin coherent elaboration [11, 15, 16, 67].

The aim of the experiment is to manipulate spin coherent of polaron pairs between singlet and triplet and detect the effect of this on the OLED device current.

4.1 The polaron pair model:
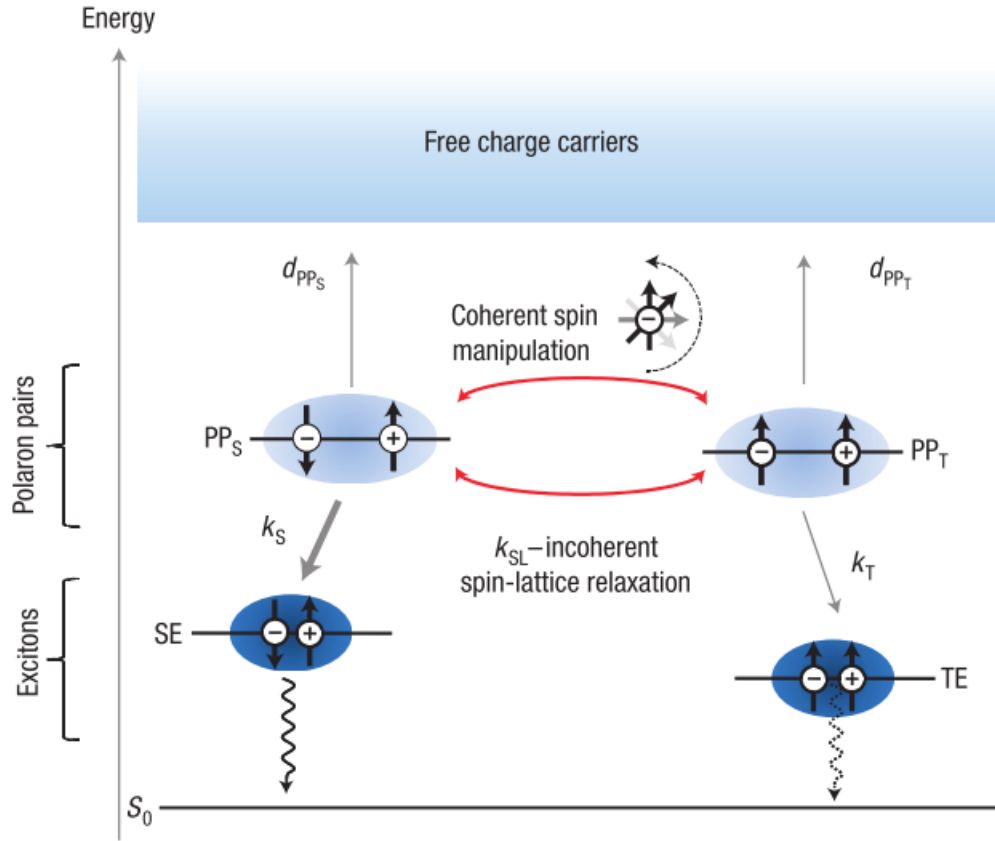
Figure 4.1: Diagram schematic indicates recombination and dissociation processes polaron pairs in organic semiconductors [15]. Reprinted by permission from [D. R. McCamey, H. A. Seipel, S.-Y. Paik, M. J. Walter, N. J. Borys, J. M. Lupton and C. Boehme, "Spin Rabi flopping in the photocurrent of a polymer light-emitting diode", Nature Materials 7, 723 - 728 (2008), [COPYRIGHT] (2008).

The polaron pairs, as presented in the 4th section in ch 2, after formation have three possible transformation processes shown in fig 4.1, which are necessary for the detection of spin coherent manipulation.

The three processes are:

1. Polaron pair can dissociate into free charge carriers with singlet and triplet dissociation constant rate (d_{pp_s} & d_{pp_T}) , and that will increase the photocurrent

2. Polaron pair can combine to produce an exciton formation, which leads to reduce the dissociation into free charge carriers process and that will decrease the photocurrent

3. Polaron pair can transient spin manifold between singlet and triplet states through two procedures:

a) Through incoherent spin lattice relaxation with the rate k_{SL}
b) Through coherent motion resulted between singlet and triplet configuration by using pulsed ESR to manipulate spin coherent control with strong microwave fields applied

[5, 15, 124]

As mentioned previously, a strong magnetic field has resulted in significant changes in the current through the OLED, enabling the spin dependent recombination rates of polaron pairs (exciton formation) to be determined [5]. Therefore, detecting spin nutation between singlet and triplet polaron pairs is based on the dependency of the current to the population of polaron pair singlet and triplet [5, 15, 67]. Singlet and triplet populations return back to their equilibrium state after the transition process, thus the device current these perturbations cause also return to equilibrium [5, 15]. Conductivity changing as a function of time is expected in this experiment and has the form

$$\Delta\sigma(t) = 2\mu e \Delta n (-d_{pp_S} e^{-(k_S + d_{pp_S})t} + d_{pp_T} e^{-(k_T + d_{pp_T})t}$$ (4.1)

$$\Delta n = \Delta n_T = -\Delta n_S$$ (4.2)

where Δn presents the number of polaron pairs moved from singlet to triplet, μ is the average mobility of free charge carrier, and $(k_S + d_{pp_S})$ and $(k_T + d_{pp_T})$ are the two time equilibrium rates [15].

Notice that singlet and triplet transients have an opposite sign and that explained the increasing and decreasing in the current which is observed experimentally. The polaron-pair loss rates (Γ_S) and (Γ_T) are defined in the equations (4.3) and (4.4) below:

$$\Gamma_S = d_S + r_S$$ (4.3)

$$\Gamma_T = d_T + r_T$$ (4.4)

where d_S, d_T are the singlet and triplet dissociation rate, and r_S, r_T are the singlet and triplet recombination rate respectively.

And from [125] the transient solutions to the singlet and triplet rate equations above are:

$$n_s(t) = A_1 e^{(-\Gamma_1 t)} + A_2 e^{(-\Gamma_2 t)} + n_s^0 \tag{4.5}$$

$$n_T(t) = B_1 e^{(-\Gamma_1 t)} + B_2 e^{(-\Gamma_2 t)} + n_T^0 \tag{4.6}$$

where $A_{1,2}$ and $B_{1,2}$ present the amplitude, and n_s^0 and n_T^0 the steady state solutions given by:

$$n_T^0 = \frac{\rho G_S k_{SR} + (\Gamma_S + \rho k_{SR}) G_T}{\Gamma_S \Gamma_T + (1-\rho) k_{SR} \Gamma_S + \rho k_{SR} \Gamma_T} \tag{4.7}$$

$$n_S^0 = \frac{(1-\rho) G_T k_{SR} + (\Gamma_T + (1-\rho) k_{SR}) G_S}{\Gamma_S \Gamma_T + (1-\rho) k_{SR} \Gamma_S + \rho k_{SR} \Gamma_T} \tag{4.8}$$

Where G_S & G_T are singlet and triplet generation rate, k_{SR} is spin relaxation rate, and Γ_1 and Γ_2 are rates given by:

$$\Gamma_1 = \frac{(\Gamma_S + \Gamma_T + k_{SR}) - [(\Gamma_S - \Gamma_T)^2 + 2(2\rho - 1) k_{SR}(\Gamma_S - \Gamma_T) + k_{SR}^2]^{1/2}}{2} \tag{4.9}$$

$$\Gamma_2 = \frac{(\Gamma_S + \Gamma_T + k_{SR}) + [(\Gamma_S - \Gamma_T)^2 + 2(2\rho - 1) k_{SR}(\Gamma_S - \Gamma_T) + k_{SR}^2]^{1/2}}{2} \tag{4.10}$$

4.2 Pulsed EDMR experiment:

Spin coherent manipulation of polaron pairs between singlet and triplet and detect the effect of this on the OLED device current is the main purpose of this experiment.

Although electrically detected magnetic resonance of OLEDs has previously been undertaken [15], the capability had not been demonstrated in our laboratory. As such, we considered it important to reproduce those measurements for several reasons: 1) to provide a level of confidence in the reproducibility of the results obtained previously on devices with different fabrication parameters, 2) to develop the capability to undertake those measurements and in future apply them to other materials, and 3) to enable future measurements in applying adiabatic pulses to OLEDs building on the work in this thesis.

In this experiment, organic semiconductors materials have been used, practically OLED device with MEH-PPV see fig 4.2. The devices, as detailed in chapter 3, were fabricated on a glass substrate with 70 mm X 3 mm dimensions and be formed of ITO (100-150 nm), PEDOT:PSS (40 nm), MEH-PPV (100 nm), LiF (0.8 nm), Ca (50 nm), and Al (100 nm). Figure 4.3 below shows the I-V curve for the OLED device that been used in these experiments.
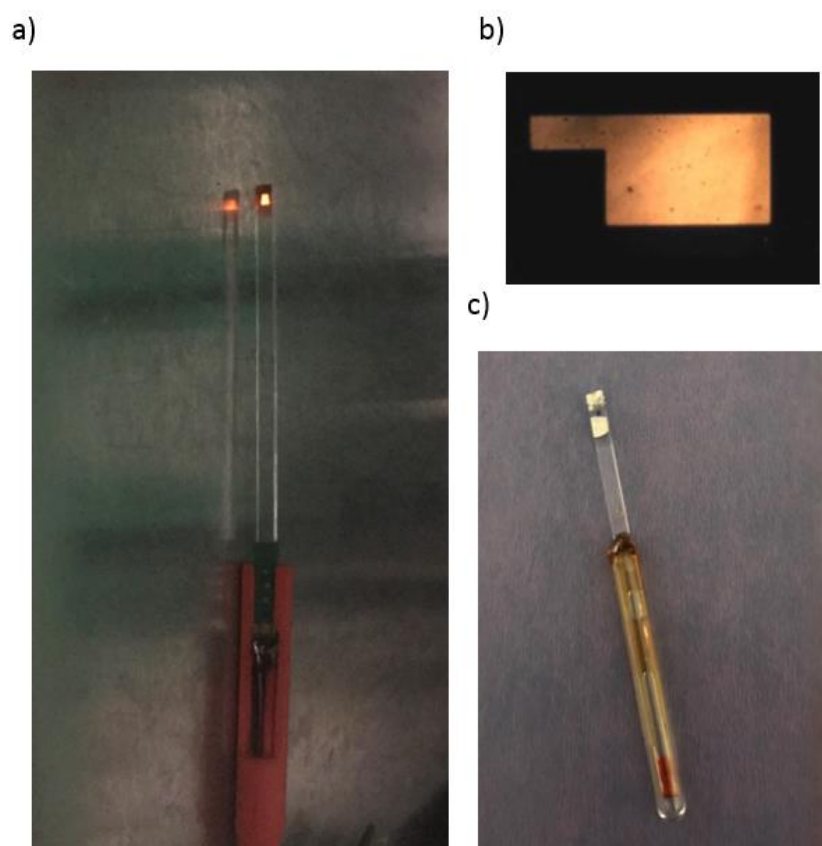
Figure 4.2: a) Organic light emitting diode held by EDMR sample holder

b) OLED pixel showed in a)

c) OLED encapsulated inside MD5 tube.
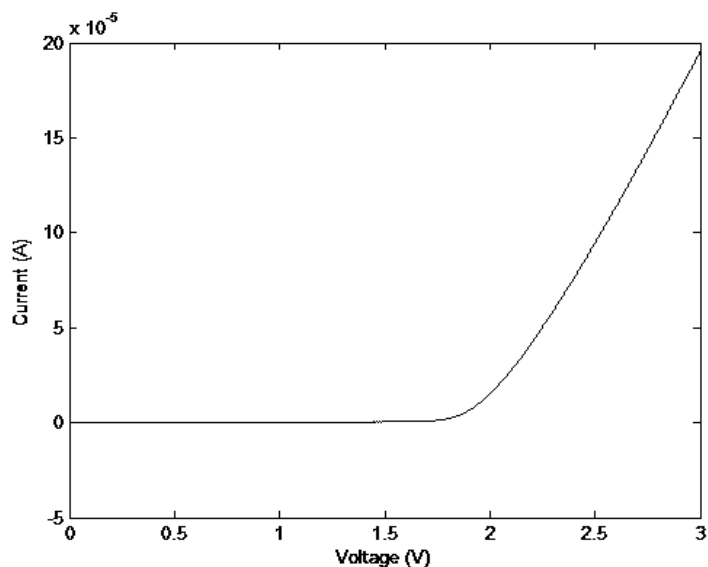
Figure 4.3: Current-voltage (I-V) characteristics of OLEDs devices with 3000 RPM spin coating speed for both PEDOT: PSS and MEH-PPV (50% toluene and 50% cyclohexane), LiF at RT, Ca, and Al.

A Bruker Elexsys E580 pulsed electron paramagnetic resonance system was used in the implementation of the measurements provided with an Oxford continuous flow nitrogen cryostat to maintain the resonator cavity at 80K. Applying voltage to the sample with current about (100) μA produced visible light through a small window in the resonator. A Stanford Research Systems SRS 570 is used to amplify the signal after it was filtered to remove the noise of D.C. component. After that, the amplified signal was observed and averaged by a transient recorder in the Bruker system. See fig 4.4
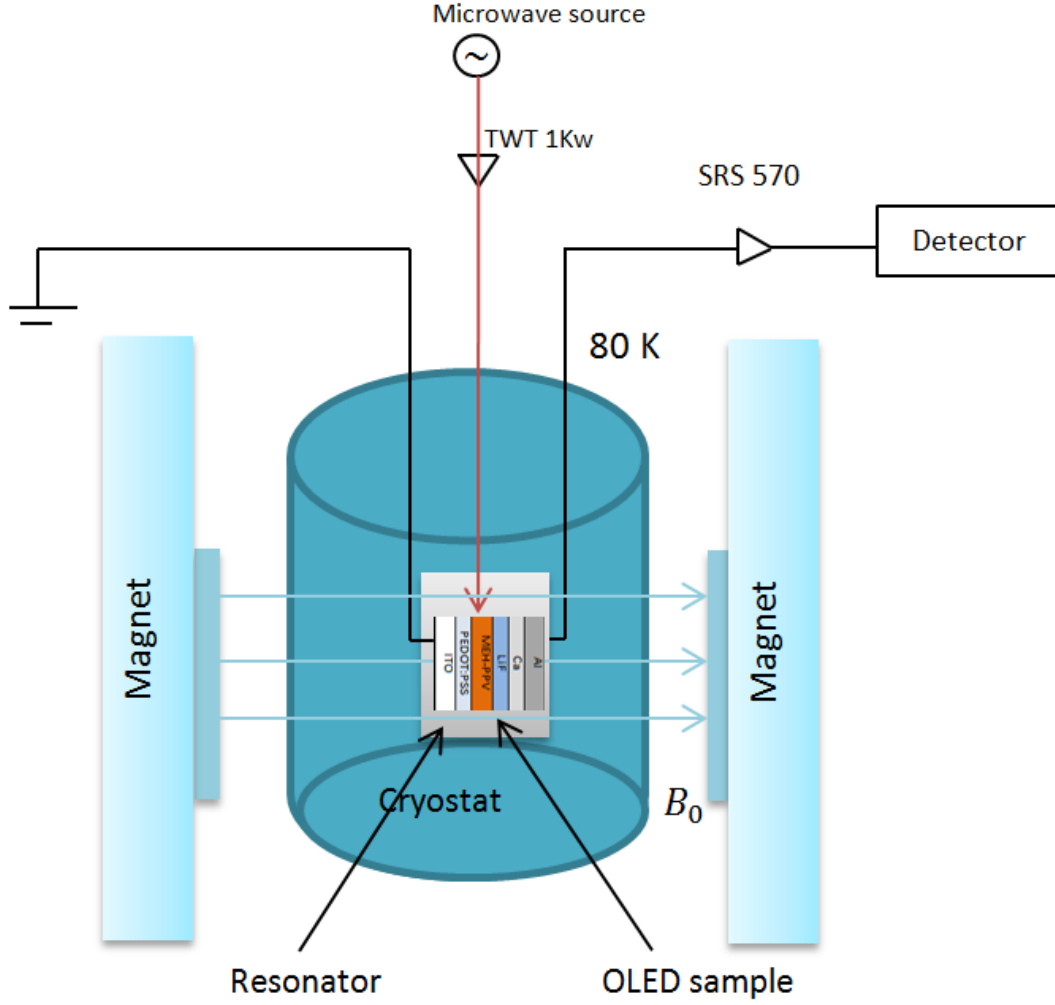
Figure 4.4: EDMR experiment setup.

By applying microwave pulses B_1 to the sample within 20 mw and for 160 ns, which regenerated every 500µs and recording changing current (ΔI), the transient behaviour was determined. By applying an external magnetic field B_0 during the measurement, which causes two Zeeman split eigenstates of each polaron pair spin, orthogonal to B_1 leads to spin polaron pair movement between singlet and triplet configurations [5, 15, 124]. In the measurement, the external magnetic field is increased by 0.1 mT for each scanning time. Also, repeating and averaging the measurement led to a better result. A non-resonant background due to sample magnetoresistance was subtracted.

The microwave frequency can be determined from the spin resonance equation condition below:

$$f = g\mu_B B_0/h \qquad (4.11)$$

Where g is the Lande g-factor, μ_B is the Bohr magneton B_0 is an external magnetic field and h is Planck's constant. This allows spin manipulation where the polaron pairs move between singlet and triplet states owing to either one or both spins flip and produce permutation symmetry of the spins [5, 15, 124].

By assuming that $g_e \neq g_h$ where g_e and g_h are the g factor for electron and hole respectively, which leads to spin polaron pairs mixing states, the fact that $(g_e - g_h)B_0 > B_1$ will allow either electron or hole to be nutated, while this $(g_e - g_h)B_0 < B_1$ will allow both of them to be nutated, with the oscillation of the singlet and triplet population ratio occurs between minimum and maximum in two situations [5, 15, 124].

4.3 Results and discussion:

4.3.1 Transient EDMR:

As seen in fig 4.5 a), the current changes as a function of time at 80 K in OLED through the impact of the applied microwave pulse and static magnetic field.
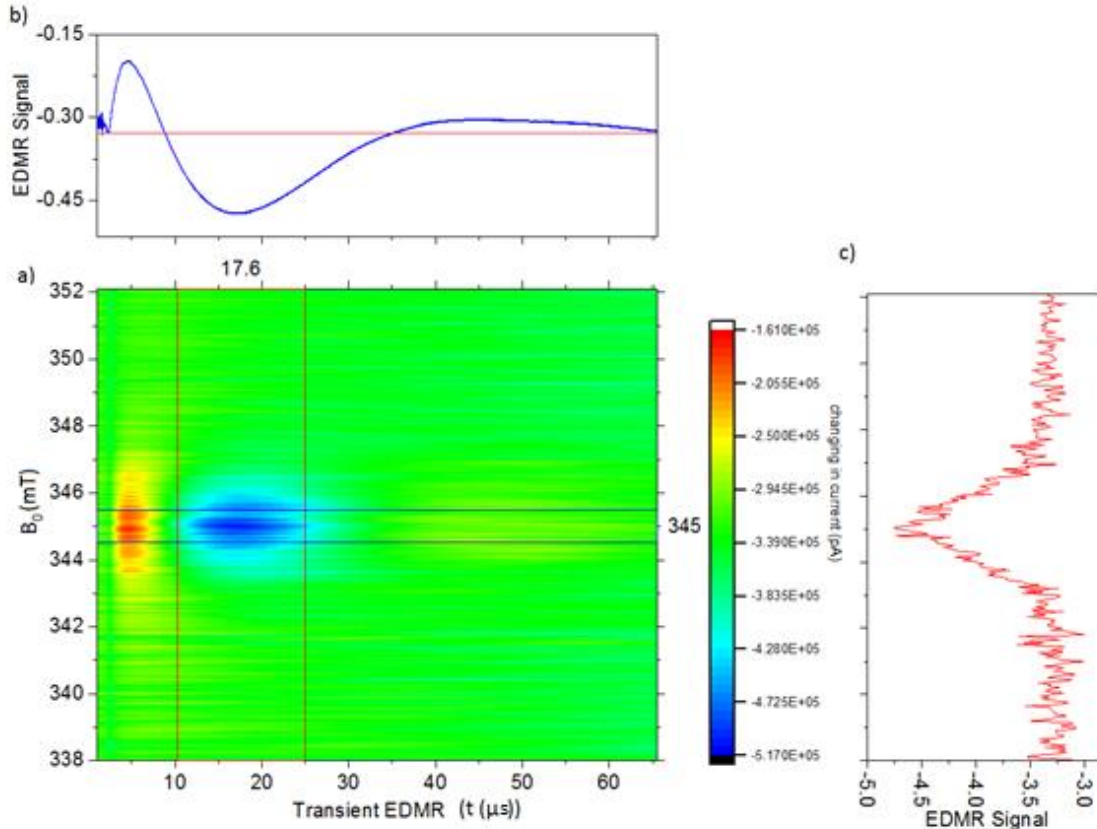
Figure 4.5: a) The changing current in OLED with time and magnetic field following the microwave pulse, the color plot represents a resonance at $B_0 = 345$ mT with a large quenching of the current (blue) and small enhancing (orange).

b) The quenching and enhancing of the current signal from a) as a slice at static field $B_0 = 345$ mT along time in µs.

c) Transient EDMR spectrum shows resonance at 345 mT.

The plot shows a resonance at $B_0 = 345$ mT, with a large quenching of the current (blue) peaked at 17.6 µs after 100 ns duration microwave pulse, and small enhancing of the current (orange) observed before that time (at 5 µs).

In fig 4.5 b), changing the current as a function of time at $B_0 = 345$ mT is observed. Increasing the current above the steady state at about 3 µs (due) is related to the slow triplet population ratio reaching the equilibrium state. Dropping down at 10 µs below the steady state showing the quenching current, followed by slightly increasing above the steady state before reaching the equilibrium level at a later time (~66 µs)

The quenching of current followed by an enhancement signals in transient observation is because the dissociation rate of singlet polaron-pairs is greater than triplets, which is related to the different energy levels of singlet and triplet due to the difference in exchange coupling, as shown in Ref [15].
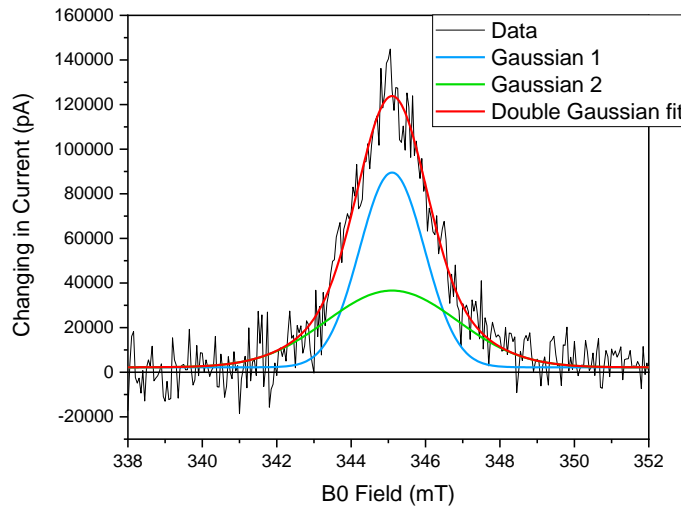
Figure 4.6: The spectra linewidth in organic semiconductors; disorder. 2 spin distributions: polaron pairs. The resonance spectrum of polaron pairs fit with two Gaussians.

From fig 4.6, the spectra linewidth $\Delta B_1 = 2.06$ mT, and $\Delta B_2 = 4.14$ mT for the two spins respectively, and all the below parameters are extracted from the transient EDMR.

Singlet and triplet loss rates are:

$1/\Gamma_S \leq 8.5$ μs

$1/\Gamma_T = 25$ μs

And Spin lattice relaxation time $T_1 \geq 8.5$ μs is extracted from the transient [125].

We used equations 4.5 and 4.6 to get the numerical simulation of the current transient signals as seen in fig 4.7. This was implemented via a script, which solved equations 4.5 and 4.6 simultaneously, then using the curvefit routine of Matlab with time and change in current as fit parameters. In this simulation, we have set the values for n_T^0 and n_S^0 as:

$$n_S^0 = A_3 e^{(-\Gamma_3 t)} \tag{4.12}$$

$$n_T^0 = B_3 e^{(-\Gamma_3 t)} \tag{4.13}$$

with $\Gamma_3 = 64\ \mu s^{-1}$ and $A_3 = -4.1 \times 10^5$ to account for the slight rise at long times (t >35 μs), which is potentially due to the experimental apparatus, particularly the time constant of the constant current source.
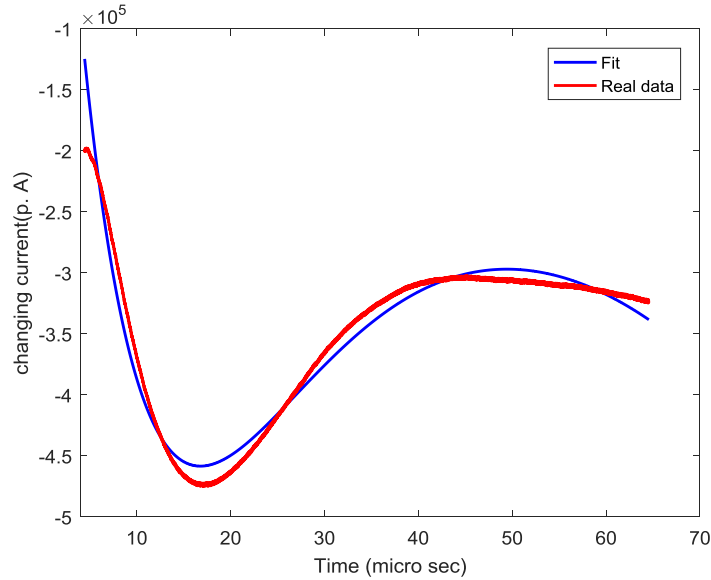
Figure 4.7: Numerical simulation (blue) and experimentally measurement (red) of the current transient. The current transient shows an enhancement-quenching signal. The simulation transient created by using eq. 4.5 and 4.6 with parameters: $\Gamma_1 = 8.9 \times 10^4\ \mu s^{-1}$, $\Gamma_2 = 9.6 \times 10^4\ \mu s^{-1}$, $A_1 = -5.8 \times 10^6$, $A_2 = 6.2 \times 10^6$

4.3.2 Rabi oscillation:

The fundamental examination for spin coherent time manipulation in OLED is demonstrated by the previous results. Figure 4.8 below (taken from [15]) shows the result of the changing of microwave pulse as a function of time. This result allows determining changing spin due to coherent excitation by modulated the total charge in the quenching part of the transient [15]. With different microwave power, the microwave pulse increased in a range between 0 to 500 ns in figure 4.8, and the increase is in conjunction with the absolute value of the total charge |ΔQ|. This measurement allows to electron-hole spin state in OLED to be coherently determined. The fluctuation of the pulse here is related to the spin coherent manipulation; at around 100 ns, the triplet population obtains its maximum and the current is decreased. However, when τ > 100 ns, the spin polaron pair is rotated into transverse plane xy by an angle greater than π, and then returns back to its initial state which leads to reducing the triplet density and increasing the current [15].

The rotating-frame Bloch spheres show the time evolution of spin relative to the microwave field B_1. Spin-coherent manipulation can be described by the quasiperiodic transfer function in equation 4.14 whenever the applied microwave pulse is a spatially homogeneous B_1 field.
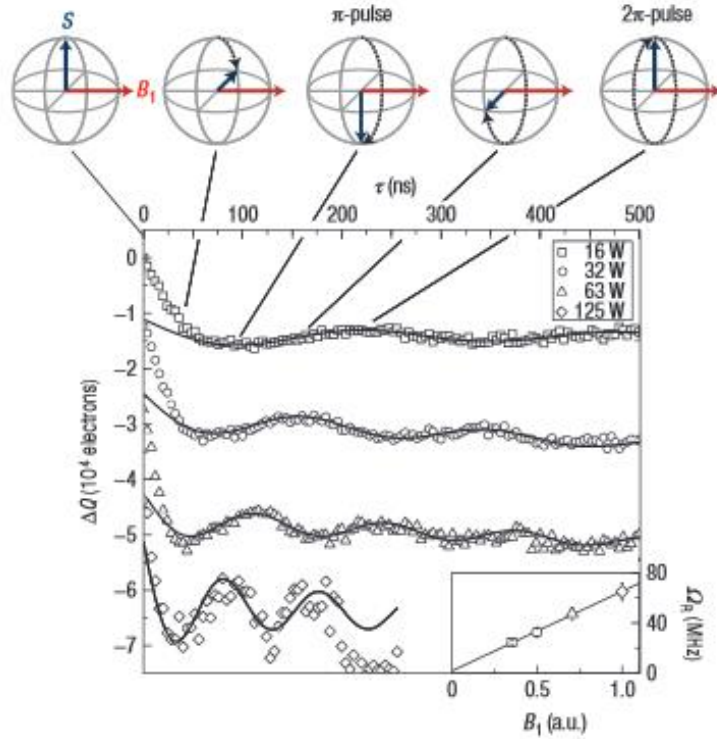
Figure 4.8: Spin coherent control of OLED [15]. Reprinted by permission from [D. R. McCamey, H. A. Seipel, S.-Y. Paik, M. J. Walter, N. J. Borys, J. M. Lupton and C. Boehme, "Spin Rabi flopping in the photocurrent of a polymer light-emitting diode", Nature Materials 7, 723 - 728 (2008), [COPYRIGHT] (2008).

$$T(\alpha) = \pi \int_0^\alpha J_0(2x)\, dx \tag{4.14}$$

where α is a parameter described by $2\alpha = \Omega_R \tau$, where τ is the pulse length and Ω_R is Rabi frequency, and J_0 is the first-order Bessel function. The value of Ω_R for each microwave power used is illustrated as a linear function in the small plot in fig 4.8.

Remarkable points from fig 4.8 mentioned in [15], that the higher microwave power provides noisier than the lower one and this resulted from the sample affected by microwave powers which produce the increasing of electromagnetic background. In addition, $T(\alpha)$ works when the microwave pulse with an excitation width is smaller than the resonance linewidth and this when the pulse length is ~50 ns.

D. McCamey *et al.* have shown in [15] that the phase coherent time $T_2^* > 0.5$ µs as Rabi oscillation observed at this time. They proposed that phase coherent estimated time resulted in [13] occurs at relaxation lower time for all polaron pairs. This point of confinement is the base time in which polaron sets change among singlet and triplet. Therefore, in polaron pair in MEH-PPV, the spin configuration is not changing with the static magnetic field due to long spin coherence time's observation as the spin dynamics for this is far too slow. However, they showed that spin dependent recombination and dissociation, with the two spin configurations determined in the time domain.

They conclude that high sensitivity investigation for spin phase coherence and spin–spin coupling is provided by spin coherent manipulation in macroscopic and nanoscale organic optoelectronic devices by detecting spin coherent manipulation in an OLED through spin-dependent transport mechanism, and demonstrate spin coherent time > 0.5 µs.

In this thesis, Rabi oscillation measurement has different device fabrication with a different voltage applied compared to the one presented by D. McCamey et al [15] previously.
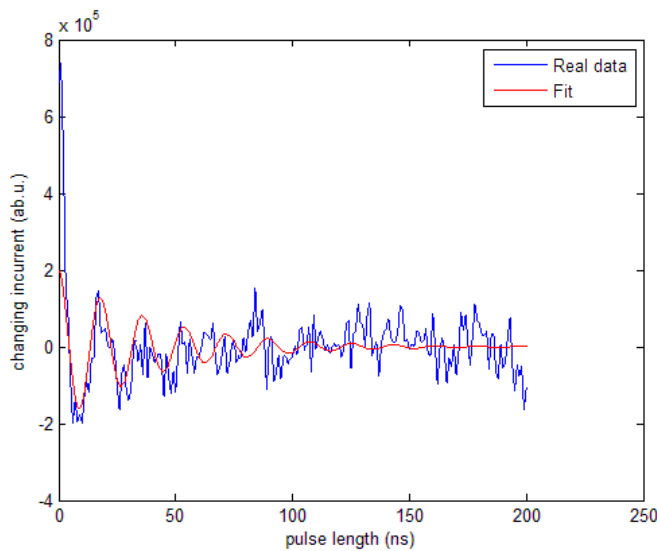
Figure 4.9: Experiment result of integrated charge as a function of microwave pulse length. Rabi oscillation.

The fluctuation of the pulse in fig 4.9 is around 9 ns when the triplet population is reaching its maximum and the current is decreasing. For the pulse length $\tau > 9$ ns , the triplet density is decreasing and the current is increasing due to the rotating of polaron pair to the transverse plane and then return back to the initial state.

The spin coherent manipulation can be described by equation 4.14 as shown previously, and $T(\alpha)$ satisfies at pulse length~ 10 ns when the microwave pulse with an excitation width is smaller than the resonance linewidth.

From Rabi oscillation plot in fig 4.9, the phase coherent time T_2^* determined to be ~ 0.04 µs at the relaxation lower time when the polaron sets change between singlet and triplet. This T_2^* was extracted using fit function consisting of a cosine function with an exponential decay envelope, $\cos(\Omega t)e^{-t/T_2^*}$, as seen in fig 4.9. The low limit of T_2^* comes from Rabi oscillation as seen in fig 4.9, and we know that they are effectively short due to microwave inhomogeneity. Other researchers found T_2^* of a couple of 100 ns using hanh echo approaches. This proves again that the spin configuration in MEH-PPV polaron pair does not change with the static magnetic field because of the observation of long spin coherence time in polaron pair.

The above results demonstrate the reproducible is in agreement with the previous work and demonstrate sufficient measurements to improve the sensitivity of EDMR technique for investigating both spin phase coherent and spin-spin coupling in nanoscale organic optoelectronic devices, in practically OLED's by applying adiabatic pulses as well demonstrated in the following chapter.

Chapter 5. Improving Magnetic Field Sensing in OLED with Adiabatic Pulses

5.1 Theoretical and practical limits of magnetic field sensing

Generally, every measurement method has its limits. From the theoretical point of view, the fundamental barrier for the precision or sensitivity growth of any measurements in the quantum world is the Heisenberg limit. This restriction is based on the well-known quantum-mechanical Heisenberg uncertainty principle and consists of the impossibility of measuring the physical values of the complementary variables or canonically conjugate variables. In magnetometry, this limit can be defined as the field strength at which identifying the magnetic field from the quantum noise is impossible. Thus, the standard quantum noise limit of sensitivity is $\delta_X \sim 1/\sqrt{N}$, where N is the number of independent particles used for measurements as a quantum interferometer. Although this sensitivity limit is determined by the N, the typical absolute values of it are approximately equal to $10^2 - 10^3 \ aT/Hz^{1/2}$. At the present time, various schemes for achieving the Heisenberg limit in magnetic measurements [126, 127, 128], or even go beyond it [129, 130] have been proposed.

In the practical use, the sensitivity limits depend on the method and specific features of the experimental device. For instance, the shot-noise-limited sensitivity of the NV diamond magnetometer [89] is determined by the interrogation time, which, depending on the chosen laser pulse sequence type, should optimally be equal to the ensemble dephasing time or to the intrinsic spin coherence time (see previous sections). In ref. [89] and other papers, researchers have achieved the sensitivity in the range from 120 nT $Hz^{-1/2}$ to 250 aT $Hz^{-1/2}cm^{-3/2}$ for various types of sequences and different numbers (and densities) of the nitrogen-vacancy centres. On the contrary, the sensitivity of the OLED-based magnetometers is smaller and rarely exceeds the 50 nT $Hz^{-1/2}$ [16].

Numerical simulation is an important and useful method for modelling organic systems and understanding the spin dynamics quantitatively. In the next section, we introduce the simulation of pulsed electrical detected magnetic resonance response of organic light-emitting diode with realistic dephasing mechanisms of an ensemble of two spin polaron pairs. Also, we demonstrate the simulation of various pulse schemes on that ensemble in the presence of spin relaxation. We solved the stochastic Liouville equation to describe the dynamics of a statistical ensemble of spins subject to a time-dependent driving field and subject to recombination and decoherence mechanisms. The stochastic Liouville equation allows us to model multiple microscopic reactions using a single framework. Previous work [4, 42] used a simple Liouville equation; here we add the Redfield component in order to include spin lifetime and phase coherence and provide a more realistic simulation of a system in which we know these effects occur on relevant timescale (from our experimental results in Chapter 4) s. Although we initially began with earlier code from the group, the substantial structural and functional

changes required to implement both a Redfield component as well as recombination and dissociation terms mean that the resulting code bears little resemblance to the earlier code. The final version of the code generated and used in this thesis can be found in Appendixes A – D.

5.2 Numerical/ Superoperator simulation:

We solve the stochastic Liouville equation to describe the dynamics of a statistical ensemble of two spin-1/2 polaron-pairs subject to a time-dependent driving field and subject to recombination and decoherence mechanisms. In contrast to earlier work in this group, we now include a Redfield term to explicitly incorporate the impact of spin phase-decoherence and lifetimes, as well as including a spin-dependent recombination and dissociation term. See Appendix A for details of the implementation.

As explained previously in chapter 2, the stochastic Liouville equation [131] used to describe the dynamics of a statistical ensemble of quantum systems whose time evolutions depend on the relevant Hamiltonian is

$$\frac{d\hat{\rho}}{dt} = -\frac{i}{\hbar}[\hat{\rho}, \widehat{H}] + \widehat{S}[\hat{\rho}] + \widehat{R}\{\hat{\rho} - \hat{\rho}_0\} \tag{5.1}$$

where $\hat{\rho} = \hat{\rho}(t)$ is the density matrix operator, $\widehat{S}$ is the stochastic operator and refers to the external changes the ensemble due to generation, spin-dependent recombination, and dissociation of spin pairs, $\widehat{R}$ describes the influence of the spin relaxation, and $\widehat{H}$ is Hamiltonian for the summation time dependent and independent [11, 19, 132, 133]

$$\widehat{H}(t) = \widehat{H}_0 + \widehat{H}_1(t) \tag{5.2}$$

$$\widehat{H}_0 = \mu_B g_e B_{z1} S_e^z + \mu_B g_e B_{z2} S_e^z \tag{5.3}$$

where B_{z1} & B_{z2} are Overhauser field for spin 1 and 2 respectively, and

$$\widehat{H}_1 = \mu_B g_1 [\widehat{S}_{x1} B_x(t) + \widehat{S}_{y1} B_y(t)] + \mu_B g_2 [\widehat{S}_{x2} B_x(t) + \widehat{S}_{y2} B_y(t)] \tag{5.4}$$

Here, I used $g = 2$ which is close to the value seen in MEH-PPV (2.006) and other organic materials [37], although the specific value is not critical for the simulations which follow.

I used equation 2.6 in chapter 2 to define the Hamiltonian. We know from earlier work that the line widths are set by the hyperfine interaction and that the J and $\widetilde{D}_d$ terms are substantially smaller than these [79], and we therefore exclude J and $\widetilde{D}_d$ from the model [37]. We know, again from earlier work,

that there is variation in the hyperfine interaction [134], and we include this in the model. We also note that this detuning will have a similar effect to variations in J and $\widetilde{D}_d$ in the high field limit, giving us further confidence that excluding them from the model will not negatively impact our simulations.

The recombination operator and spin relaxation superoperator have been defined in equations 2.40 and 2.44 and Redfield matrix with coefficients in equation 2.46 in chapter 2.

Note that, in this modelling, we assume singlet and triplet *dissociation* rates are both equal to zero. As addressed in chapter 2, using a superoperator formalism to transfer Hamiltonian, recombination, and density matrices from Hilbert space ($n \times n$) to Liouville equation ($n^2 \times n^2$) leads to enhancement of the calculation precision and speed [19, 132].

Therefore, the recombination (stochastic) superoperator and Super Hamiltonian and observable are as defined as in equations 2.47, 2.48, and 2.49.

Transforming the density matrix is implemented with the following equation:

$$\hat{\rho} = \begin{bmatrix} a_{1,1} & a_{1,2} & \cdots & a_{1,n} \\ a_{2,1} & a_{2,3} & \cdots & a_{2,n} \\ \vdots & \vdots & \ddots & \vdots \\ a_{m,1} & a_{m,2} & \cdots & a_{m,n} \end{bmatrix} \rightarrow \begin{bmatrix} a_{1,1} \\ a_{1,2} \\ a_{1,3} \\ \vdots \\ a_{m,n} \end{bmatrix} \tag{5.5}$$

MATLAB™ has been used to solve the superoperator Liouville equation with a set of 16 x 16 matrix. Starting with defining the density initial state ρ_0 for the two spins polaron pairs in the product base as showed in equation 2.33

$$\rho_0 = C'C = \begin{bmatrix} 1 & 0 & 0 & 0 \\ 0 & 0 & 0 & 0 \\ 0 & 0 & 0 & 0 \\ 0 & 0 & 0 & 0 \end{bmatrix} \tag{5.6}$$

Then convert the density initial state from Hilbert space (4x4) to Liouville density vector (16 x 1). The spin Hamiltonian $\hat{H}_{super}$ is calculated in Liouville space for the two spins with different Overhauser field B_{z1} & B_{z2} and (a constant driving field) applied magnetic field B_x and produces 16 x 16 matrix size.

Also, the recombination $\hat{S}_{super}$ is calculated in Liouville space and given 16 x 16 matrix with singlet and triplet recombination rate r_s =0.1 μS^{-1} , $r_T = 0.001$ μS^{-1} respectively.

The Redfield matrix for one spin (electron) with coefficients is:

$$
\hat{R}_e = \begin{bmatrix} \dfrac{1}{T_{1e}} & 0 & 0 & -\dfrac{1}{T_{1e}} \\ 0 & \dfrac{1}{T_{2e}} & -\dfrac{1}{T_{2e}} & 0 \\ 0 & -\dfrac{1}{T_{2e}} & \dfrac{1}{T_{2e}} & 0 \\ -\dfrac{1}{T_{1e}} & 0 & 0 & \dfrac{1}{T_{1e}} \end{bmatrix}
\tag{5.7}
$$

Then the spin relaxation matrix which is defined before can be written as:

$$
\hat{R}_{super} = \hat{R}_h \otimes \hat{I} + \hat{I} \otimes \hat{R}_e
\tag{5.8}
$$

where $\hat{R}_h$ is the Redfield matrix for the second spin (hole) which is same as $\hat{R}_e$, and $\hat{I}$ is the unitary operator that projects the matrix onto itself. The form of the spin relaxation matrix $\hat{R}_{super}$ (16 x 16) is given below, with additional coefficients T_3 , T_4 , T_5 , T_6 , T_7 , T_8 , T_9 T_{10} where:

$$
\frac{1}{T_3} = \frac{1}{T_{1e}} + \frac{1}{T_{1h}} \quad , \qquad
\frac{1}{T_4} = \frac{1}{T_{1e}} - \frac{1}{T_{1h}} \quad , \qquad
\frac{1}{T_5} = -\frac{1}{T_{2e}} - \frac{1}{T_{2h}} \quad , \qquad
\frac{1}{T_6} = \frac{1}{T_{1e}} - \frac{1}{T_{2h}} \quad ,
$$

$$
\frac{1}{T_7} = \frac{1}{T_{1e}} + \frac{1}{T_{2h}} \quad , \qquad
\frac{1}{T_8} = -\frac{1}{T_{2e}} - \frac{1}{T_{1h}} \quad , \qquad
\frac{1}{T_9} = -\frac{1}{T_{2e}} + \frac{1}{T_{1h}} , \qquad
\frac{1}{T_{10}} = -\frac{1}{T_{2e}} + \frac{1}{T_{2h}}
$$

$$\hat{R}_{super} =$$

$$
\begin{bmatrix}
\frac{1}{T_3} & \frac{1}{T_{1h}} & \frac{1}{T_{1h}} & -\frac{1}{T_4} & \frac{1}{T_{1e}} & 0 & 0 & -\frac{1}{T_{1e}} & \frac{1}{T_{1e}} & 0 & 0 & -\frac{1}{T_{1e}} & \frac{1}{T_4} & -\frac{1}{T_{1h}} & -\frac{1}{T_{1h}} & -\frac{1}{T_3} \\[6pt]
-\frac{1}{T_{1h}} & \frac{1}{T_8} & \frac{1}{T_9} & \frac{1}{T_{1h}} & 0 & \frac{1}{T_{2e}} & -\frac{1}{T_{2e}} & 0 & 0 & \frac{1}{T_{2e}} & -\frac{1}{T_{2e}} & 0 & -\frac{1}{T_{1h}} & \frac{1}{T_9} & \frac{1}{T_8} & \frac{1}{T_{1h}} \\[6pt]
\frac{1}{T_{1h}} & \frac{1}{T_9} & -\frac{1}{T_8} & \frac{1}{T_{1h}} & 0 & -\frac{1}{T_{2e}} & \frac{1}{T_{2e}} & 0 & 0 & -\frac{1}{T_{2e}} & \frac{1}{T_{2e}} & 0 & -\frac{1}{T_{1h}} & \frac{1}{T_8} & -\frac{1}{T_9} & -\frac{1}{T_{1h}} \\[6pt]
-\frac{1}{T_4} & \frac{1}{T_{1h}} & \frac{1}{T_{1h}} & \frac{1}{T_3} & -\frac{1}{T_{1e}} & 0 & 0 & \frac{1}{T_{1e}} & -\frac{1}{T_{1e}} & 0 & 0 & \frac{1}{T_{1e}} & \frac{1}{T_3} & \frac{1}{T_{1h}} & \frac{1}{T_{1h}} & \frac{1}{T_4} \\[6pt]
\frac{1}{T_{1e}} & 0 & 0 & -\frac{1}{T_{1e}} & \frac{1}{T_7} & \frac{1}{T_{2h}} & \frac{1}{T_{2h}} & \frac{1}{T_6} & \frac{1}{T_6} & \frac{1}{T_{2h}} & -\frac{1}{T_{2h}} & \frac{1}{T_7} & \frac{1}{T_{1e}} & 0 & 0 & -\frac{1}{T_{1e}} \\[6pt]
0 & \frac{1}{T_{2e}} & -\frac{1}{T_{2e}} & 0 & \frac{1}{T_{2h}} & \frac{1}{T_5} & \frac{1}{T_{10}} & \frac{1}{T_{2h}} & -\frac{1}{T_{2h}} & \frac{1}{T_{10}} & \frac{1}{T_5} & \frac{1}{T_{2h}} & 0 & \frac{1}{T_{2e}} & -\frac{1}{T_{2e}} & 0 \\[6pt]
0 & -\frac{1}{T_{2e}} & \frac{1}{T_{2e}} & 0 & \frac{1}{T_{2h}} & \frac{1}{T_{10}} & \frac{1}{T_5} & -\frac{1}{T_{2h}} & \frac{1}{T_{2h}} & \frac{1}{T_5} & \frac{1}{T_{10}} & -\frac{1}{T_{2h}} & 0 & -\frac{1}{T_{2e}} & \frac{1}{T_{2e}} & 0 \\[6pt]
-\frac{1}{T_{1e}} & 0 & 0 & \frac{1}{T_{1e}} & \frac{1}{T_6} & \frac{1}{T_{2h}} & \frac{1}{T_{2h}} & \frac{1}{T_7} & \frac{1}{T_7} & \frac{1}{T_{2h}} & -\frac{1}{T_{2h}} & \frac{1}{T_6} & \frac{1}{T_{1e}} & 0 & 0 & \frac{1}{T_{1e}} \\[6pt]
\frac{1}{T_{1e}} & 0 & 0 & -\frac{1}{T_{1e}} & \frac{1}{T_6} & \frac{1}{T_{2h}} & \frac{1}{T_{2h}} & \frac{1}{T_7} & \frac{1}{T_7} & \frac{1}{T_{2h}} & \frac{1}{T_{2h}} & \frac{1}{T_6} & \frac{1}{T_{1e}} & 0 & 0 & -\frac{1}{T_{1e}} \\[6pt]
0 & \frac{1}{T_{2e}} & -\frac{1}{T_{2e}} & 0 & \frac{1}{T_{2h}} & \frac{1}{T_{10}} & \frac{1}{T_5} & \frac{1}{T_{2h}} & -\frac{1}{T_{2h}} & \frac{1}{T_5} & \frac{1}{T_{10}} & \frac{1}{T_{2h}} & 0 & \frac{1}{T_{2e}} & -\frac{1}{T_{2e}} & 0 \\[6pt]
0 & -\frac{1}{T_{2e}} & \frac{1}{T_{2e}} & 0 & \frac{1}{T_{2h}} & \frac{1}{T_5} & \frac{1}{T_{10}} & \frac{1}{T_{2h}} & \frac{1}{T_{2h}} & \frac{1}{T_{10}} & \frac{1}{T_5} & \frac{1}{T_{2h}} & 0 & -\frac{1}{T_{2e}} & \frac{1}{T_{2e}} & 0 \\[6pt]
-\frac{1}{T_{1e}} & 0 & 0 & \frac{1}{T_{1e}} & \frac{1}{T_7} & \frac{1}{T_{2h}} & \frac{1}{T_{2h}} & \frac{1}{T_6} & \frac{1}{T_6} & \frac{1}{T_{2h}} & \frac{1}{T_{2h}} & \frac{1}{T_7} & \frac{1}{T_{1e}} & 0 & 0 & \frac{1}{T_{1e}} \\[6pt]
\frac{1}{T_4} & -\frac{1}{T_{1h}} & -\frac{1}{T_{1h}} & \frac{1}{T_3} & \frac{1}{T_{1e}} & 0 & 0 & -\frac{1}{T_{1e}} & \frac{1}{T_{1e}} & 0 & 0 & -\frac{1}{T_{1e}} & \frac{1}{T_3} & \frac{1}{T_{1h}} & \frac{1}{T_{1h}} & -\frac{1}{T_4} \\[6pt]
\frac{1}{T_{1h}} & -\frac{1}{T_9} & -\frac{1}{T_8} & \frac{1}{T_{1h}} & 0 & \frac{1}{T_{2e}} & -\frac{1}{T_{2e}} & 0 & 0 & \frac{1}{T_{2e}} & -\frac{1}{T_{2e}} & 0 & \frac{1}{T_{1h}} & \frac{1}{T_8} & \frac{1}{T_9} & \frac{1}{T_{1h}} \\[6pt]
-\frac{1}{T_{1h}} & \frac{1}{T_8} & \frac{1}{T_9} & \frac{1}{T_{1h}} & 0 & -\frac{1}{T_{2e}} & \frac{1}{T_{2e}} & 0 & 0 & -\frac{1}{T_{2e}} & \frac{1}{T_{2e}} & 0 & \frac{1}{T_{1h}} & \frac{1}{T_9} & \frac{1}{T_8} & \frac{1}{T_{1h}} \\[6pt]
-\frac{1}{T_3} & -\frac{1}{T_{1h}} & -\frac{1}{T_{1h}} & \frac{1}{T_4} & -\frac{1}{T_{1e}} & 0 & 0 & \frac{1}{T_{1e}} & -\frac{1}{T_{1e}} & 0 & 0 & \frac{1}{T_{1e}} & -\frac{1}{T_4} & \frac{1}{T_{1h}} & \frac{1}{T_{1h}} & \frac{1}{T_3}
\end{bmatrix}
$$

Fig 5.1 and 5.2 show the simulation results of spin density and the magnetization movement for two spins one initially up and one initially down, in the rotating frame, with applied field $B_x= 1$ mT, and singlet and triplet recombination rates $r_s =0.1\ \mu s^{-1}$, $r_T = 0.001\ \mu s^{-1}$ and spin lattice relaxation times $T_{1e} = 1\ \mu s$, $T_{1h} = 1.1\ \mu s$, and spin-spin relaxation times $T_{2e}= 0.2\ \mu s$, $T_{2h}= 0.3\ \mu s$ for both spins respectively, ii) and iii) demonstrate the magnetization movement on Cartesian along the time 400 ns for both spins, v) shows the Fourier transformation of i) along the time axis with a frequency peak at $\sim 28\ MHz$ on resonance (in a), and at $\sim 64\ MHz$ off resonance (in b), and vi)) the spin density decay due to the quenching in triplet density and enhancing in singlet density and decay further in b) due to the detuning, while with spin relaxation the density decay further ,figures in a) when both spins on resonance (both $B_{z1,2} = 0$) while figures b) include detuning at $B_{z1}= 2$ mT.

a) Both spins on resonance in a system with recombination
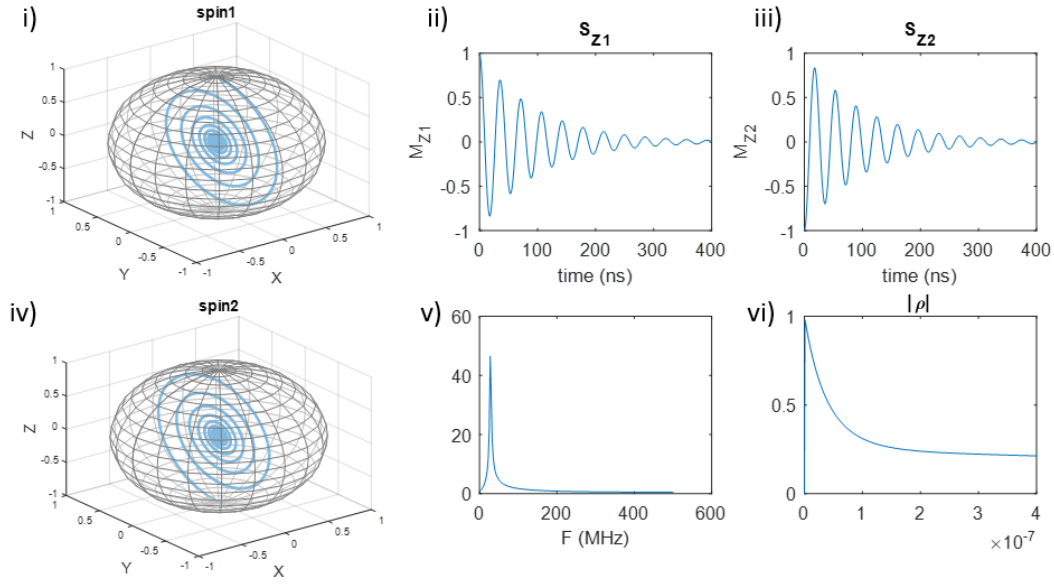
b) One spin on resonance, and one off resonance in a system with recombination
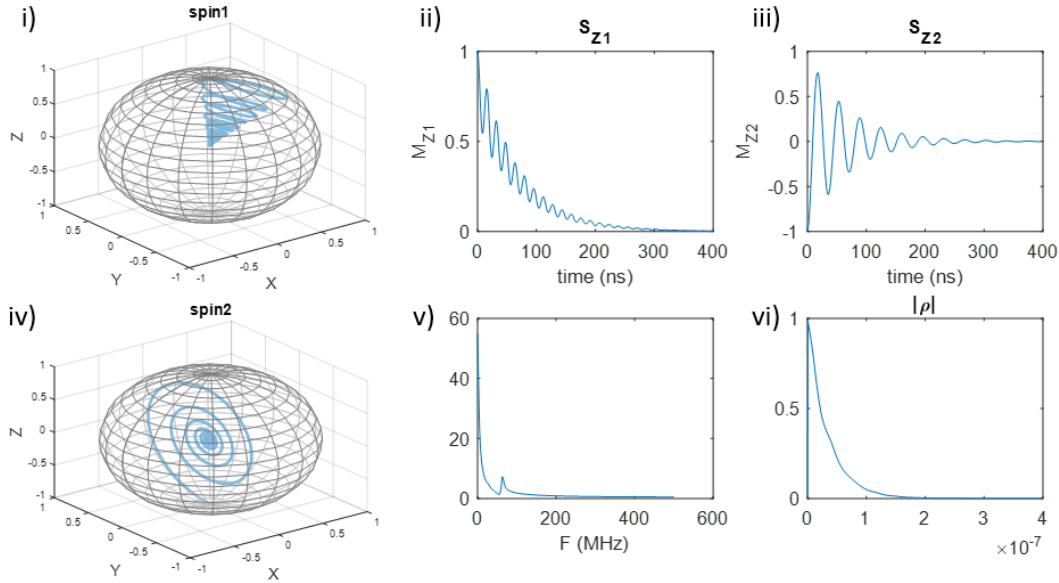
Figure 5.1: The magnetization movement for two spins (one initially up, one initially down) on the Bloch sphere including recombination with singlet and triplet recombination rates r_s =0.1 μs^{-1} , $r_T =$ 0.001/10 e^{-2} μs^{-1} respectively , ii) and iii) Sz1 and Sz2 show the magnetization movement on Cartesian along the time 400 ns, v) shows the Fourier transformation of i) along the time axis with a frequency peak at ~ 28 MHz on resonance, and at ~ 64 MHz off resonance and vi) the decay of spin density due to the recombination, figures in a) when both spins on resonance (both $B_{z1,2} = 0$) while figures b) include detuning at B_{z1}= 2 mT.

a) Both spins on resonance in a system with recombination and relaxation

i)

ii)

iii)

iv)

v)

vi)

b) One spin on resonance, and one off resonance in a system with recombination and relaxation

i)

ii)

iii)

iv)

v)

vi)

Figure 5.2: The magnetization movement for two spins (one initially up, one initially down) on the Bloch sphere including recombination with singlet and triplet recombination rates r_s =0.1 μs^{-1} , $r_T =$ 0.001 μs^{-1} and spin lattice relaxation times $T_{1_e} = 1$ μs , $T_{1_h} = 1.1$ μs , and spin-spin relaxation times $T_{2_e}= 0.2$ μs , $T_{2_h}= 0.3$ μs for both spins respectively , ii) and iii) Sz1 and Sz2 show the magnetization movement on Cartesian along the time 400 ns, v) shows the Fourier transformation of i) along the time axis with a frequency peak at ~ 28 MHz on resonance, and at~ 64 MHz off resonance, and vi) the decay of spin density due to both recombination and spin relaxation, figures in a) when both spins are on resonance (both $B_{z1,2} = 0$) while figures b) include detuning at $B_{z1}= 2$ mT.

Both simulation results in fig 5.1 and 5.2 have the same conditions except adding spin relaxation on fig 5.2. It is clearly seen that when spin are on-resonance, the spin density in both figures never reaches the equilibrium state due to disability to approach to the singlet and triplet manifold for the pair. However, when spin off-resonance, it moves far from the ideal orientation and this leads to bring the triplet population in to combine, thus the spin density decay to reach the equilibrium state. With recombination only, the density of spin decay due to the singlet and triplet enhancing and quenching densities respectively. With recombination and relaxation, the spin density decay further compare with recombination only because the spin relaxation impacts the transient behavior of the recombination rate. The fact of including on/off-resonance is that the recombination rate varies, and that matches the change in the density matrix as the raw goes in and out resonance when we do Rabi oscillation during the pulse. So, if we recombine then the recombination rate is a function of the rotation angle during the pulse. Thus, we need to do a perfect 2π rotation from up-up to up -up. Even if the rotation itself is done with very high fidelity, the fact that going through down-up to some period of time leads to having not a perfect state when going back to start state. Thus, these are the implication of realistic modeling of that.

The equations below taken from [42] have been used in this simulation.

$$B_1(t) = A(t)e^{i\phi(t)} \tag{5.9}$$

$$A(t) = B_{1max}F_1(\tau) \tag{5.10}$$

$$\phi(t) = \phi_0 + 2\Pi \int_0^{T_p} f_{center} + f_{max}F_2(\tau)d\tau \tag{5.11}$$

where $B_1(t)$ is the magnetic field generated by an amplitude, B_{1max} is the maximum signal amplitude, $F_1(\tau)$ and $F_2(\tau)$ are the frequency modulation functions, f_{center} is the carrier frequency of the signal, which is the transition of a fixed frequency that is modified with a signal to transfer information, f_{max} is the maximum frequency sweep amplitude, ϕ_0 is the initial phase, T_p is the pulse length, and τ is the normalized time for t, $\tau = \frac{2t}{T_p} - 1$. And the magnetic field component of the pulse along $\hat{x}$ and $\hat{y}$ can be written as:

$$B_1^x(t) = B_{1max}F_1(\tau)\cos[\Delta\phi(t)] \tag{5.12}$$

$$B_1^y(t) = B_{1max}F_1(\tau)\sin[\Delta\phi(t)] \tag{5.13}$$

Some of the common modulation function F_1 and F_2 used in this simulation taken from [42] are demonstrated in the table 5.1 below.

	$F_1(\tau)$	$F_2(\tau)$
Square	1	-
Gaussian	$e^{-(\frac{\tau-t_0}{\sqrt{2}\sigma})^2}$	-
Chirp	1	τ

Table 5.1: Some of common modulation functions for various pulses, taken from [42].

The below figures shows a comparison of amplitude, frequency, and signal of various pulses used in this simulation with $B_{1max} = 1$ mT, $T_p = 200\ ns$, and $f_{max} = 250$ MHz. The amplitude is $B_{1max}\ F_1(\tau)$, and frequency $f_{max}\ F_2(\tau)$. For chirp pulse we have sweep the frequency in a range between (-250 to +250) MHz in a time of 200 ns.
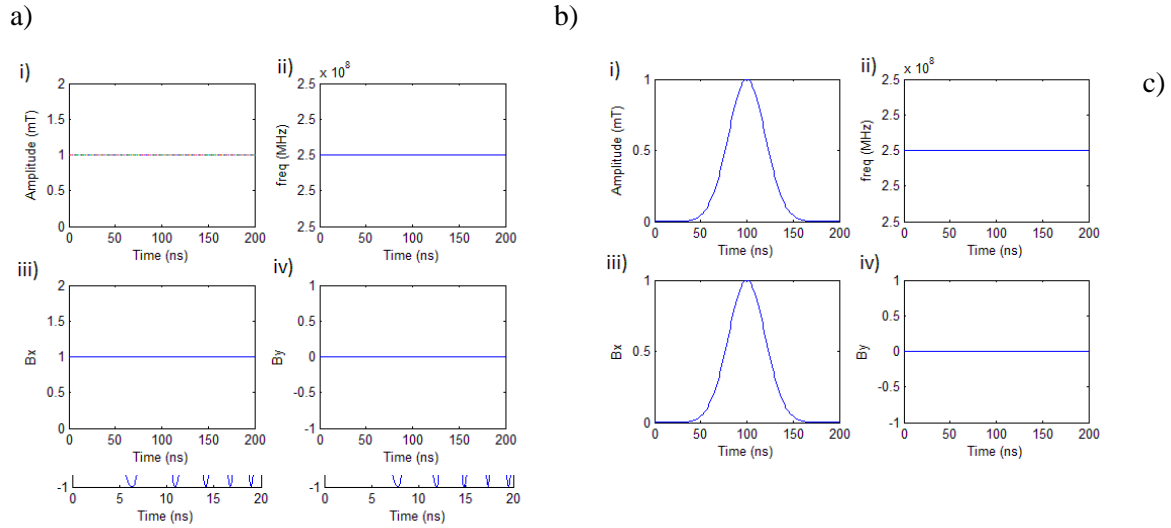
Figure 5.3: The amplitude, the frequency, and B_x and B_y for a) square pulse, b) Gaussian pulse, and c) chirp pulse with pulse amplitude $B_{1max} = 1$ mT, $T_p = 200\ ns$, and $f_{max} = 250$ MHz.

5.2.1 Hahn Echo Simulations – no recombination-no relaxation

The Hahn echo sequence is a significant spin detection method in pulsed EPR spectroscopy and it is used to investigate the decoherence time of the spin system. We will first investigate a system with no relaxation or recombination, to understand the impact of adiabatic pulse in an ideal system.

For all simulations in this section and sections 5.2.2, 5.2.3, 5.2.4, and 5.2.5 we simulated conventional Hahn-echo sequences as

$[\pi/2^{\text{sq},18\text{ns}} : \tau^{200\text{ns}} : \pi^{\text{sq},36\text{ns}} : \tau^{200\text{ns}} : \pi/2^{\text{sq},18\text{ns}}]$, $[\pi/2^{\text{G},71\text{ns}} : \tau^{\text{G},200\text{ns}} : \pi^{\text{G},141\text{ns}} : \tau^{\text{G},200\text{ns}} : \pi/2^{\text{G},71\text{ns}}]$, and

[$\pi/2^{Ch,270ns,400MHz}$: $\tau^{Ch,200ns}$: $\pi^{Ch,540ns,400MHz}$: $\tau^{Ch,100ns}$: $\pi/2^{Ch,270ns,400MHz}$]   for square, Gaussian, and chirp pulses respectively.

In this pulse sequence ($\pi/2$: τ : π : τ : $\pi/2$), the first $\pi/2$ pulse rotates the spins into the xy plane. After that, during the evolution time τ, the spins start to dephase and spins off-resonance with large detuning moves far from the typical orientation. The π-pulse rotates the system around the x-axis and the off-resonance spins with large detuning still moves far from y-direction. After the rephasing process caused by having the same evolution time, the last $\pi/2$ returns the system back into singlet or triplet state. The fidelity of the square pulse will decrease gradually because of the detuning, and the lost fidelity can be fixed by adiabatic pulses. The adiabatic pulses increase the excitation bandwidth and uniformity of spin rotations.

Initial condition:

In a realistic device where singlet recombination is fast, we usually start in a pure triplet state which is equivalent to up-up or down-down. In the simulations below, we will use these interchangeably, but we will not start in the up-down state anymore as it is not the dominant steady-state in OLED. If this work had been focused on photogenerated spins, it would perhaps have been appropriate to address both singlet and triplet initial conditions. Although the product states up-up and down-down are triplet, the products state up-down has both triplet and singlet character. We do not use these as initial states as the singlet component is short lived, and the triplet component dynamics should be reflected in the up-up and down-down triplet results.

Fig 5.4, 5.5 and 5.6 show the spin density and magnetization for simulation results of a conventional Hahn-echo square, Gaussian, and chirp-pulses sequences (see Appendix B) for two spins both initially up with maximum pulse amplitude $B_{1max} = 0.5\ mT$, $\sigma = 70.7$ (used in Gaussian pulse), and $f_{max} = 400\ MHz$ (used in chirp pulse), figure a) shows the detuning at ($B_{z1max} = 2$ mT) through 100 steps (loop over time), b) without detuning ($B_{z1max} = 0\ mT$) through 100 steps, c) when $B_{z1max} = 4\ mT$ through 5 steps where ($B_{z1} = n \times B_{z1max} / (steps\ no.-1)$, $n = 1: steps\ no.$), d) shows the magnetization movement on Cartesian along the time 472, 683, and 1480 ns for square, Gaussian and chirp pulse respectively with some detuning (at $B_{z1max} = 4\ mT$) through 5 steps in i) and without detuning in ii), and iii) shows the spin density.

Figure 5.4: The magnetization movement for two spins (both initially up, on and off resonance) on the Bloch sphere a) with detuning in at ($B_{z1max} = 2\,mT$) through 100 steps, b) without detuning ($B_{z1max} = 0\,mT$) through 100 steps, c) with detuning at ($B_{z1max} = 4\,mT$) through 5 steps where ($B_{z1} = n \times B_{z1max}/\,(steps\,no.-1),\ n = 1\!:\!steps\,no.$), d) Sz1 and Sz2 show the magnetization movement on Cartesian along the time i) with detuning at ($B_{z1max} = 4\,mT$) through 5 steps, ii) without detuning ($B_{z1max} = 0\,mT$) and iii) the spin density for **square** pulse.

88

Figure 5.5: The magnetization movement for two spins (both initially up, on and off resonance) on the Bloch sphere a) with detuning in at $(B_{z1max} = 2\,mT)$ through 100 steps, b) without detuning $(B_{z1max} = 0\,mT)$ through 100 steps, c) with detuning at $(B_{z1max} = 4\,mT)$ through 5 steps where $(B_{z1} = n \times B_{z1max}/(steps\,no.-1),\ n = 1:steps\,no.)$, d) Sz1 and Sz2 show the magnetization movement on Cartesian along the time i) with detuning at $(B_{z1max} = 4\,mT)$ through 5 steps, ii) without detuning $(B_{z1max} = 0\,mT)$ and iii) the spin density for **Gaussian** pulse.

Figure 5.6: The magnetization movement for two spins (both initially up, on and off resonance) on the Bloch sphere a) with detuning in at ($B_{z1max} = 2\ mT$) through 100 steps, b) without detuning ($B_{z1max} = 0\ mT$) through 100 steps, c) with detuning at ($B_{z1max} = 4\ mT$) through 5 steps where ($B_{z1} = n \times B_{z1max} / (steps\ no. -1),\ n = 1: steps\ no.$), d) Sz1 and Sz2 show the magnetization movement on Cartesian along the time i) with detuning at ($B_{z1max} = 4\ mT$) through 5 steps, ii) without detuning ($B_{z1max} = 0\ mT$) and iii) the spin density for **chirp** pulse.

Discussion:

Fig. 5.4 , 5.5 and 5.6 show that where there is no relaxation or recombination, all three pulse schemes tend to produce similar outcomes. However, Gaussian and chirp are very effective and produce higher fidelity and the reason is they have better ability to rotate slightly off resonance spins with higher fidelity than the square pulse which has a faster sequence with low fidelity. Details of the impact of detuning will be discussed in section 5.2.4 below.

5.2.2 Hahn Echo Simulations – with recombination

In this section, we extend the simulations above to consider the impact of recombination. Due to the fact that recombination causes energy loss transitions of electrons and holes, we anticipate that the fidelity of operation will be reduced compared to the ideal case above. We will investigate the impact of recombination on square, Gaussian, and chirp pulse Hahn echo sequences.

Fig 5.7, 5.8 and 5.9 show the spin density and magnetization for simulation results of a conventional Hahn-echo square, Gaussian, and chirp-pulses sequences for two spins both initially with $B_{1max} = 0.5 \, mT$, $\sigma = 70.7$ (used in Gaussian pulse), $f_{max} = 400 \; MHz$ (used in chirp pulse), and singlet and triplet recombination rates $r_s = 0.1 \, \mu s^{-1}$, $r_T = 0.001 \, \mu s^{-1}$ respectively, figure 5.7 a) shows the detuning at ($B_{z1max} = 2 \, mT$) through 100 steps, b) without detuning ($B_{z1max} = 0 \, mT$) through 100 steps, c) when $B_{z1max} = 4 \, mT$ through 5 steps where ($B_{z1} = n \times B_{z1max} / (steps \, no. -1)$, $n = 1 : steps \, no.$), d) shows the magnetization movement on Cartesian along the time 472, 683, and 1480 ns for square, Gaussian and chirp pulse respectively with some detuning (at $B_{z1max} = 4 \, mT$) through 5 steps in i) and without detuning in ii), and iii) shows the spin density.
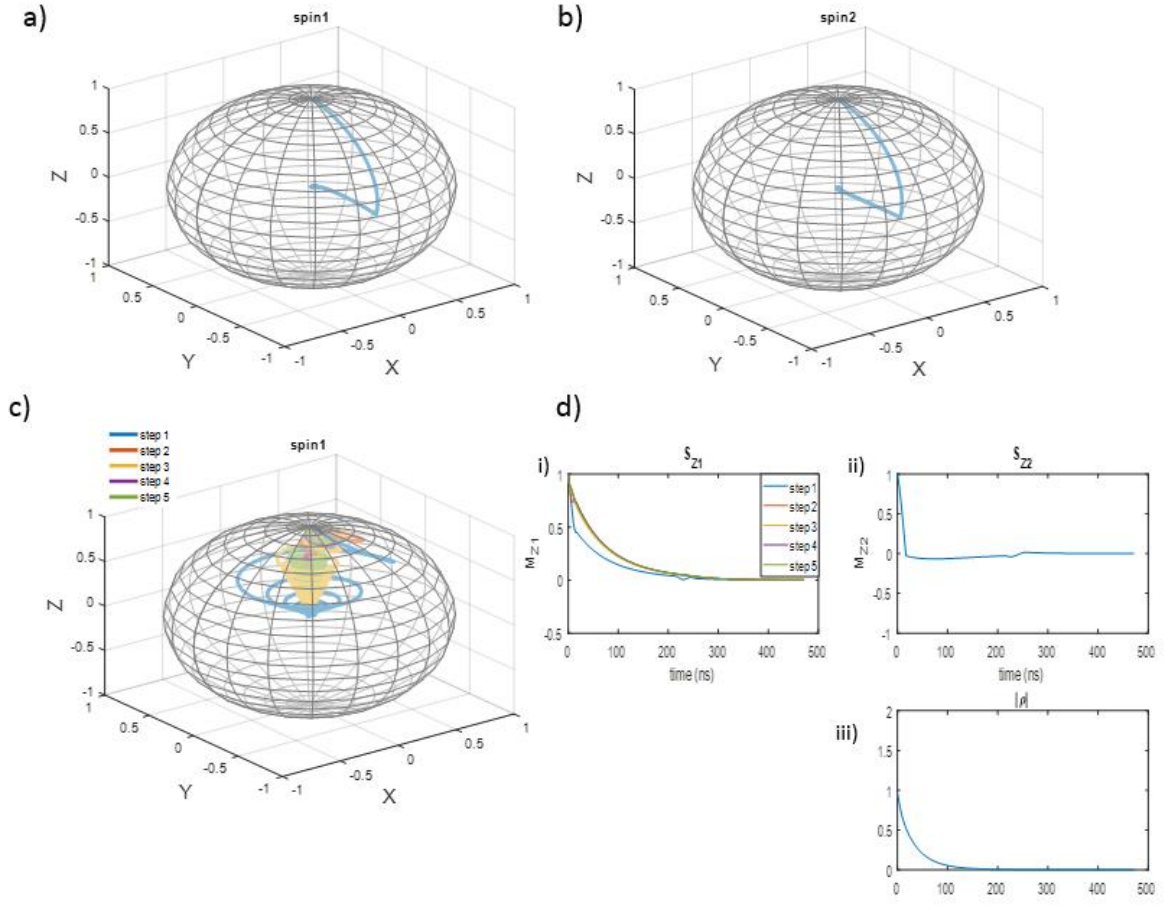
Figure 5.7: The magnetization movement for two spins (both initially up, on and off resonance) on the Bloch sphere including recombination with singlet and triplet recombination rates $r_s =0.1\ \mu s^{-1}$, $r_T = 0.001\ \mu s^{-1}$ respectively. a) with detuning in at $(B_{z1max} = 2\ mT)$ through 100 steps, b) without detuning $(B_{z1max} = 0\ mT)$ through 100 steps, c) with detuning at $(B_{z1max} = 4\ mT)$ through 5 steps where $(B_{z1} = n \times B_{z1max}/(steps\ no. -1),\ n = 1: steps\ no.)$, d) Sz1 and Sz2 show the magnetization movement on Cartesian along the time i) with detuning at $(B_{z1max} = 4\ mT)$ through 5 steps, ii) without detuning $(B_{z1max} = 0\ mT)$ and iii) the spin density for **square** pulse.

92

Figure 5.8: The magnetization movement for two spins (both initially up, on and off resonance) on the Bloch sphere including recombination with singlet and triplet recombination rates $r_S = 0.1\ \mu s^{-1}$, $r_T = 0.001\ \mu s^{-1}$ respectively. a) with detuning in at ($B_{z1max} = 2\ mT$) through 100 steps, b) without detuning ($B_{z1max} = 0\ mT$) through 100 steps, c) with detuning at ($B_{z1max} = 4\ mT$) through 5 steps where ($B_{z1} = n \times B_{z1max}/(steps\ no. - 1)$, $n = 1: steps\ no.$), d) Sz1 and Sz2 show the magnetization movement on Cartesian along the time i) with detuning at ($B_{z1max} = 4\ mT$) through 5 steps, ii) without detuning ($B_{z1max} = 0\ mT$) and iii) the spin density for **Gaussian** pulse.

Figure 5.9: The magnetization movement for two spins (both initially up, on and off resonance) on the Bloch sphere including recombination with singlet and triplet recombination rates $r_s = 0.1 \, \mu s^{-1}$, $r_T = 0.001 \, \mu s^{-1}$ respectively. a) with detuning in at $(B_{z1max} = 2 \, mT)$ through 100 steps, b) without detuning $(B_{z1max} = 0 \, mT)$ through 100 steps, c) with detuning at $(B_{z1max} = 4 \, mT)$ through 5 steps where $(B_{z1} = n \times B_{z1max} / (steps \, no. - 1), \, n = 1 : steps \, no.)$, d) Sz1 and Sz2 show the magnetization movement on Cartesian along the time i) with detuning at $(B_{z1max} = 4 \, mT)$ through 5 steps, ii) without detuning $(B_{z1max} = 0 \, mT)$ and iii) the spin density for **chirp** pulse.

Discussion:

Comparing figures in this section with figures in section 5.2.2, it is clearly seen that the Hahn-echo struggles in this level of recombination time and that will reduce the fidelity operation. When spin on-resonance, the square pulse with recombination works better than Gaussian, however, when spin off-

94

resonance Gaussian is better. Thus, in order to get higher fidelity in a system that includes recombination, a fast and short pulse is required because if the recombination time is similar to the pulse length then the pulse extremely recombine and thesystem decays Section 5.2.4 discussed the impact of detuning.

5.2.3 Hahn Echo Simulations – with recombination and relaxation

In this section, we further extend the simulations above to include the impact of recombination and spin relaxation. Spin relaxation impacts the transient behavior of the recombination rate, so we anticipate that the fidelity of operation will be reduced compared to the two cases above. We will investigate the impact of both recombination and spin relaxation on square, Gaussian, and chirp pulse Hahn echo sequences.

Fig 5.10, 5.11, and 5.12 show the spin density and magnetization for simulation results of a conventional Hahn-echo square, Gaussian, and chirp-pulses sequences for two spins both initially up with $B_{1max} = 0.5\ mT$, $\sigma = 70.7$ (used in Gaussian pulse), $f_{max} = 400\ MHz$ (used in chirp pulse), singlet and triplet recombination rates r_s =0.1 µs^{-1} , $r_T = 0.001$ µs^{-1} respectively, and spin lattice relaxation times are $T_{1_e} = 1$ µs , $T_{1_h} = 1.1$ µs , and spin-spin relaxation times are $T_{2_e} = 0.2$ µs , $T_{2_h} = 0.3$ µs for both spins respectively, figure 5.10 a) shows the detuning at ($B_{z1max} = 2\ mT$) through 100 steps, b) without detuning ($B_{z1max} = 0\ mT$) through 100 steps, c) when $B_{z1max} = 4\ mT$ through 5 steps where ($B_{z1} = n \times B_{z1max}/\ (steps\ no. -1),\ n = 1{:}\ steps\ no.$), d) shows the magnetization movement on Cartesian along the time 472, 683, and 1480 ns for square, Gaussian and chirp pulse respectively with some detuning (at $B_{z1max} = 4\ mT$) through 5 steps in i) and without detuning in ii), and iii) shows the spin density.

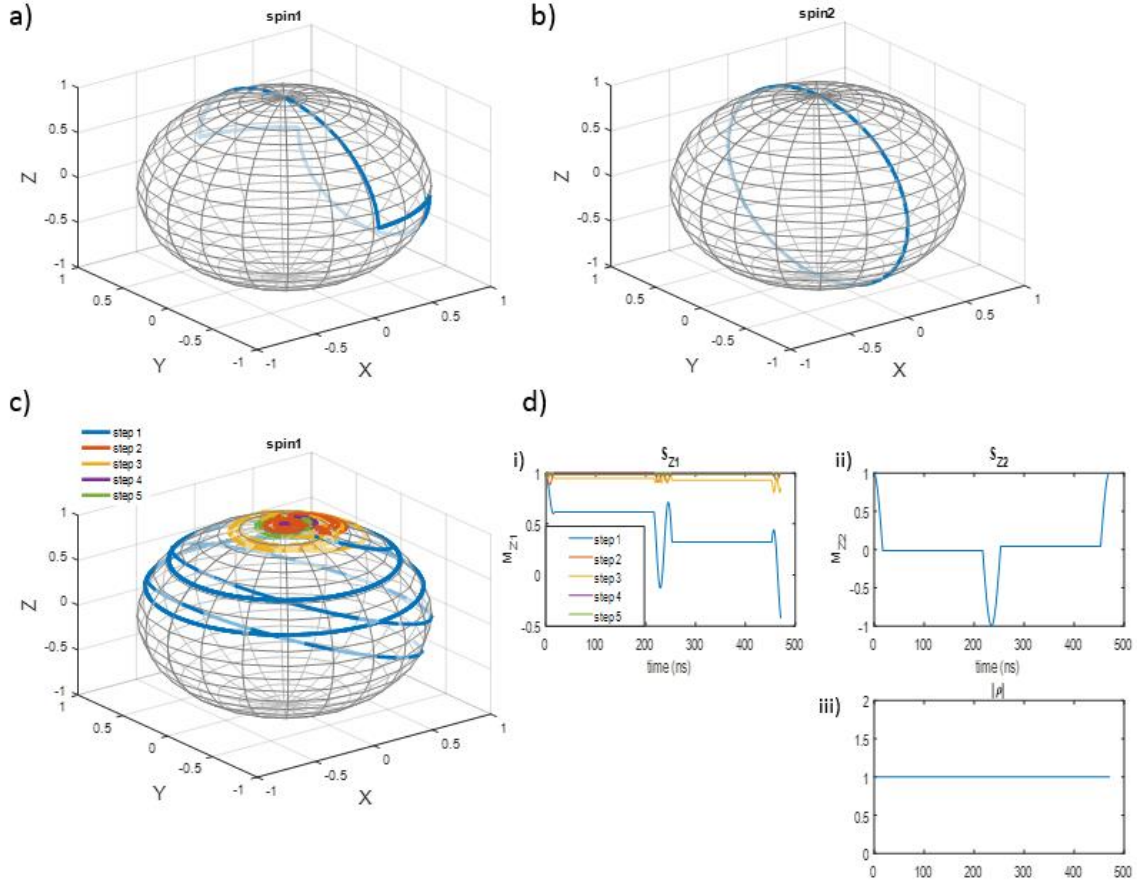**Figure 5.10:** The magnetization movement for two spins (both initially up, on and off resonance) on the Bloch sphere including **recombination and spin relaxation** with singlet and triplet recombination rates r_S =0.1 μs^{-1} , $r_T = 0.001$ μs^{-1} rrespectively, and spin lattice relaxation times $T_{1_e} = 1$ μs , $T_{1_h} = 1.1$ μs , and spin-spin relaxation times $T_{2_e}= 0.2$ μs , $T_{2_h}= 0.3$ μs for both spins respectively. a) with detuning in at $(B_{z1max} = 2\ mT)$ through 100 steps, b) without detuning $(B_{z1max} = 0\ mT)$ through 100 steps, c) with detuning at ($B_{z1max} = 4\ mT)$ through 5 steps where $(B_{z1} = n \times B_{z1max}/(steps\ no.-1),\ n = 1: steps\ no.)$, d) Sz1 and Sz2 show the magnetization movement on Cartesian along the time i) with detuning at ($B_{z1max} = 4\ mT)$ through 5 steps, ii) without detuning ($B_{z1max} = 0\ mT)$ and iii) the spin density for **square** pulse.

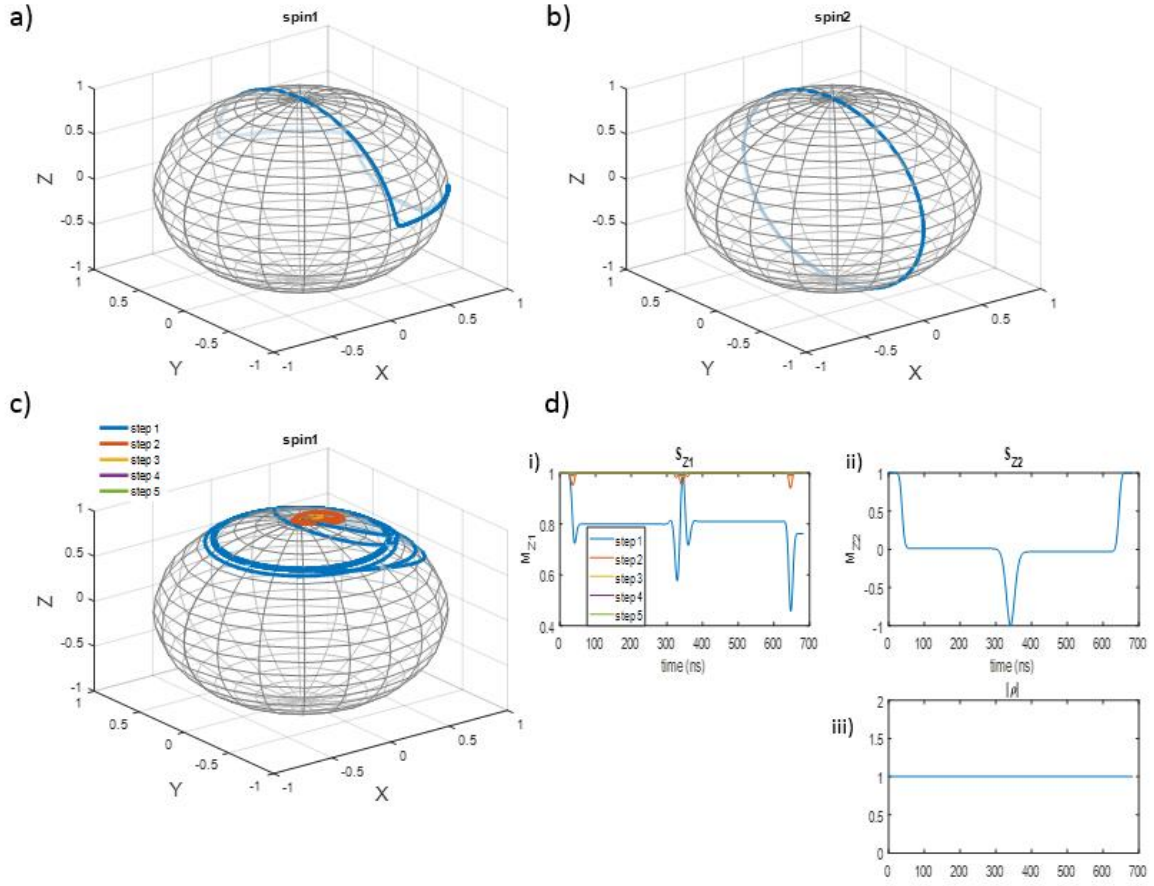**Figure 5.11:** The magnetization movement for two spins (both initially up, on and off resonance) on the Bloch sphere including **recombination and spin relaxation** with singlet and triplet recombination rates r_s =0.1 μs^{-1} , $r_T = 0.001$ μs^{-1} respectively, and spin lattice relaxation times $T_{1_e} = 1$ μs , $T_{1_h} = 1.1$ μs , and spin-spin relaxation times $T_{2_e}= 0.2$ μs , $T_{2_h}= 0.3$ μs for both spins respectively. a) with detuning in at ($B_{z1max} = 2\ mT$) through 100 steps, b) without detuning ($B_{z1max} = 0\ mT$) through 100 steps, c) with detuning at ($B_{z1max} = 4\ mT$)   through 5 steps where ($B_{z1} = n \times B_{z1max}/$ $(steps\ no. - 1)$, $n = 1: steps\ no.$), d) Sz1 and Sz2 show the magnetization movement on Cartesian along the time i) with detuning at ($B_{z1max} = 4\ mT$) through 5 steps, ii) without detuning ($B_{z1max} = 0\ mT$) and iii) the spin density for **Gaussian** pulse.
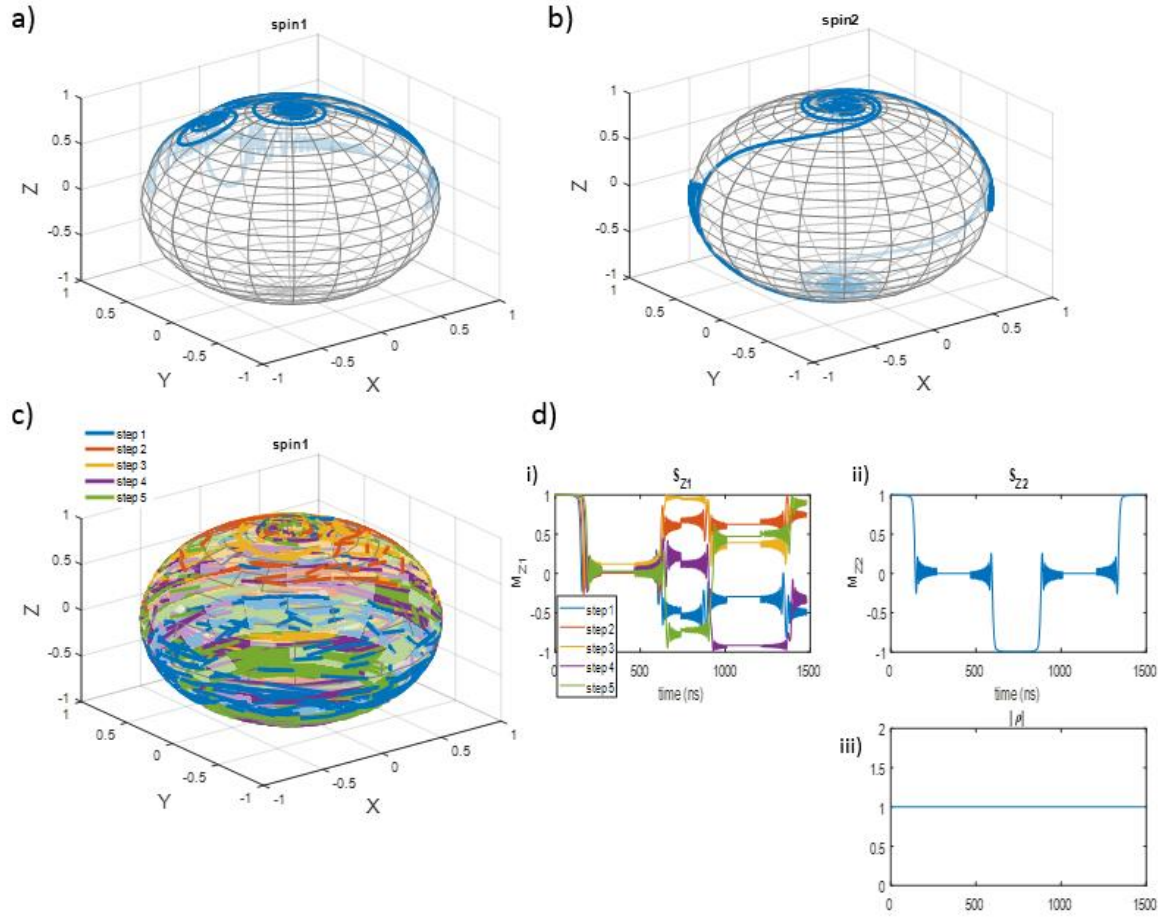
Figure 5.12: The magnetization movement for two spins (both initially up, on and off resonance) on the Bloch sphere including **recombination and spin relaxation** with singlet and triplet recombination rates r_s =0.1 μs^{-1} , $r_T = 0.001$ μs^{-1} respectively, and spin lattice relaxation times $T_{1_e} = 1$ μs , $T_{1_h} = 1.1$ μs , and spin-spin relaxation times $T_{2_e}= 0.2$ μs , $T_{2_h}= 0.3$ μs for both spins respectively. a) with detuning in at ($B_{z1max} = 2\ mT$) through 100 steps, b) without detuning ($B_{z1max} = 0\ mT$) through 100 steps, c) with detuning at ($B_{z1max} = 4\ mT$) through 5 steps where ($B_{z1} = n \times B_{z1max}/$ $(steps\ no. -1),\ n = 1: steps\ no.$), d) Sz1 and Sz2 show the magnetization movement on Cartesian along the time i) with detuning at ($B_{z1max} = 4\ mT$) through 5 steps, ii) without detuning ($B_{z1max} = 0\ mT$) and iii) the spin density for **chirp** pulse.

Discussion:
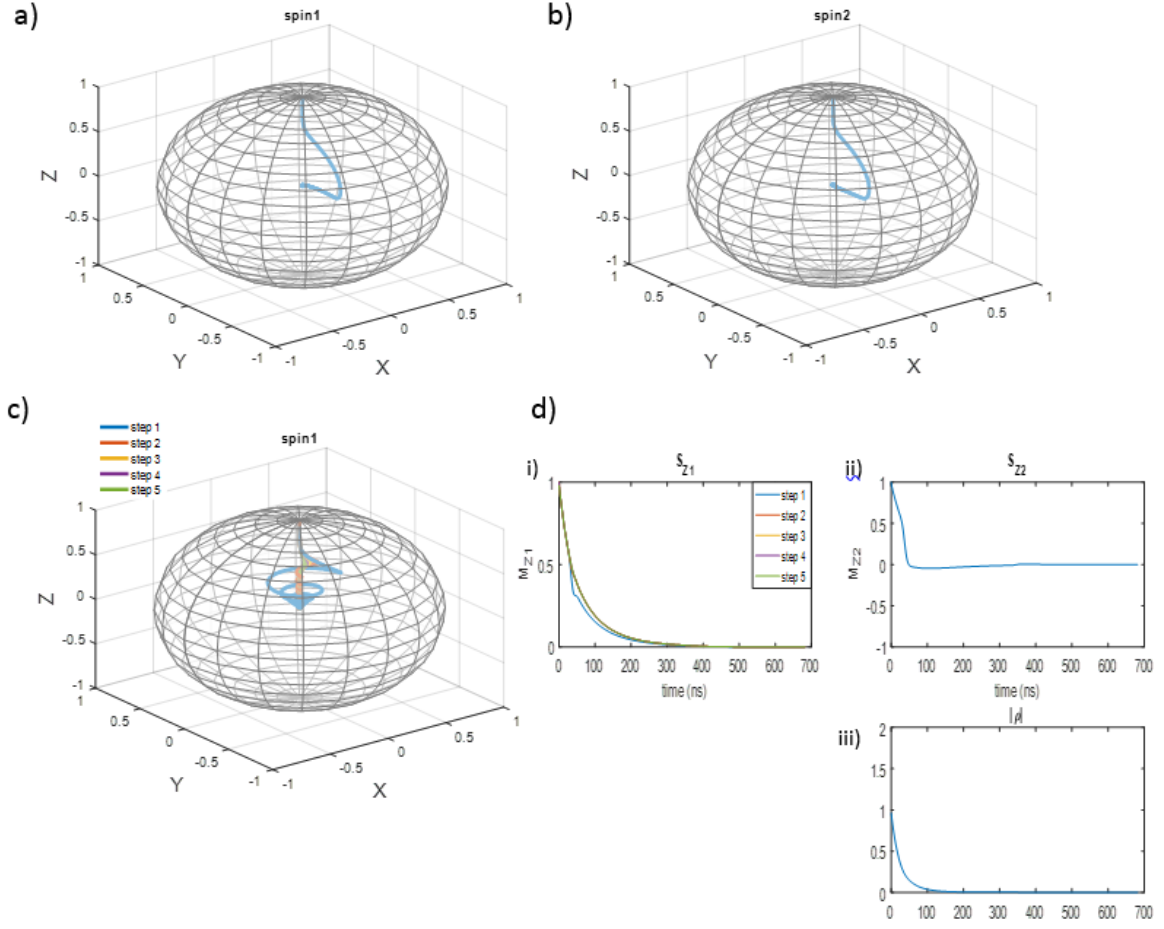
Compare figures in this section with figures in section 5.2.2 and 5.2.3 it is clearly seen that Hahn echo effected by both recombination and relaxation. Spin relaxation impacts the transient behavior of the recombination rates, and that will reduce the fidelity operation more compare to previous cases. When spins are on-resonance, the square pulse with recombination works better than Gaussian and chirp pulses, however when spins are off-resonance Gaussian and chirp are better. Section 5.2.4 discussed the impact of detuning.

5.2.4 Effect of Detuning:

In this section, we will discuss the impact of detuning of spin and compare that with the presence of recombination and spin relaxation for all three pulses.

In figures 5.4 to 5.12 above we showed the ability to model the impact of recombination and relaxation and varies of adiabatic pulses on the dynamic of pulse scheme that we use here. Plots in Fig 5.13 show the simulation signals of the magnetization Mz_1 following a $\pi/2$ pulse (red) and Hahn echo sequence (blue) as a function of detuning, where the detuning $B_{z1max} = 6\ mT$ through 200 steps for square, Gaussian and chirp pulse with singlet and triplet recombination rates $r_s = 0.1\ \mu s^{-1}$, $r_t = 1\ \mu s^{-1}$, and spin lattice and spin-spin relaxation times for both spins $T_{1_e} = 3\ \mu s$, $T_{1_h} = 3\ \mu s$, $T_{2_e} = 0.8\ \mu s$, $T_{2_h} = 1.1\ \mu s$. The red line is the excitation function after $\pi/2$ pulse and the blue after the whole sequence ($\pi/2$, π, $-\pi/2$), where the pulse length is 472, 683, and 1480 ns for square, Gaussian and chirp pulse respectively. This figure shows how that modeling works for a range of different detuning and how well we reach the target state which is 1.

99

a) Ideal pulse　　　　**b) Recombination**　　　　**c) Recombination and Relaxation**

Figure 5.13: Mz_1 following a $\pi/2$ pulse (red) and Hahn echo sequence (blue) $[\pi/2^{\text{sq,18ns}} : \tau^{200\text{ns}} : \pi^{\text{sq,36ns}} : \tau^{200\text{ns}} : -\pi/2^{\text{sq,18ns}}]$, $[\pi/2^{\text{G,71ns}} : \tau^{\text{G,200ns}} : \pi^{\text{G,141ns}} : \tau^{\text{G,200ns}} :- \pi/2^{\text{G,71ns}}]$, and

$[\pi/2^{\text{Ch,270ns,400MHz}} : \tau^{\text{Ch,200ns}} : \pi^{\text{Ch,540ns,400MHz}} : \tau^{\text{Ch,100ns}} : -\pi/2^{\text{Ch,270ns,400MHz}}]$ as a function of detuning for square, Gaussian, and chirp pulses. b) including recombination, c) including recombination and spin relaxation with singlet and triplet recombination rates $r_s = 0.1 \ \mu s^{-1}$, $r_t = 1 \ \mu s^{-1}$, and spin lattice and spin-spin relaxation times for both spins $T_{1_e} = 3 \ \mu s$, $T_{1_h} = 3 \ \mu s$, $T_{2_e} = 0.8 \ \mu s$, $T_{2_h} = 1.1 \ \mu s$ for both spins respectively.

For the ideal pulses in the fig 5.13, it is clearly seen that the Gaussian and chirp pulses work better and has higher fidelity operation compared to square pulse because they are better in rotation off-resonance spins with higher fidelity.

For the case with recombination, square pulses are better and have higher fidelity compared to Gaussian and chirp. When the pulse length is similar to the recombination time, the system starts to decay, thus faster pulse is needed. So, manipulating the system including recombination and producing high fidelity required short pulse length because this fast pulse will not extremely recombine.

For the pulses with recombination and relaxation, it gives similar results as with recombination only. However, spin relaxation has an impact on the transient behaviour recombination rates, thus more reduction of the fidelity is observed.

Therefore, the Gaussian pulse is a reasonable choice when there is no recombination and relaxation or when the length of the pulse sequence is smaller than recombination or relaxation time. The chirp pulse in the ideal case is also effective, however, it is not very good with recombination and relaxation, because the chirp scheme takes longer between pulses and therefore allows more time to recombine and relax. Thus, it depends on the pulse length, square and Gaussian are faster but chirp is longer. Hence, if we are trying to compete with recombination and relaxation processes that on the same time scale, then the faster and shorter sequence with lower fidelity gives a better outcome than the slower and longer sequence with high fidelity. Therefore, a simple pulse sequence is better than a complex pulse.

5.2.5 Modeling experimental data:

In this section, we used the simulations above including the impact of recombination and spin relaxation with the parameters determined in the experiments described in chapter 4. We will investigate the impact of both recombination and spin relaxation on square, Gaussian, and chirp pulse Hahn echo sequences.

Figures below show the simulation results of square, Gaussian and chirp pulse for two spins both up **with real parameters from the experiment:** singlet and triplet recombination rates $r_s = (1/8.5) \, \mu s^{-1}$, $r_T = (1/25) \, \mu s^{-1}$ respectively, and spin lattice relaxation times are $T_{1_e} = 8.5 \, \mu s$, $T_{1_h} = 8.5 \, \mu s$, and spin-spin relaxation times are chosen to satisfy this equation $T_1 > T_2 > T_2^*$, thus, $T_{2_e} = 0.8 \, \mu s$, $T_{2_h} = 1.1 \, \mu s$ for both spins respectively. And $B_{1max} = 0.5 \, mT$, $B_{z1max} = 6 \, mT$ through 200 steps along 472 ns, 683 ns, and 1480 ns for square, Gaussian and chirp pulse respectively.
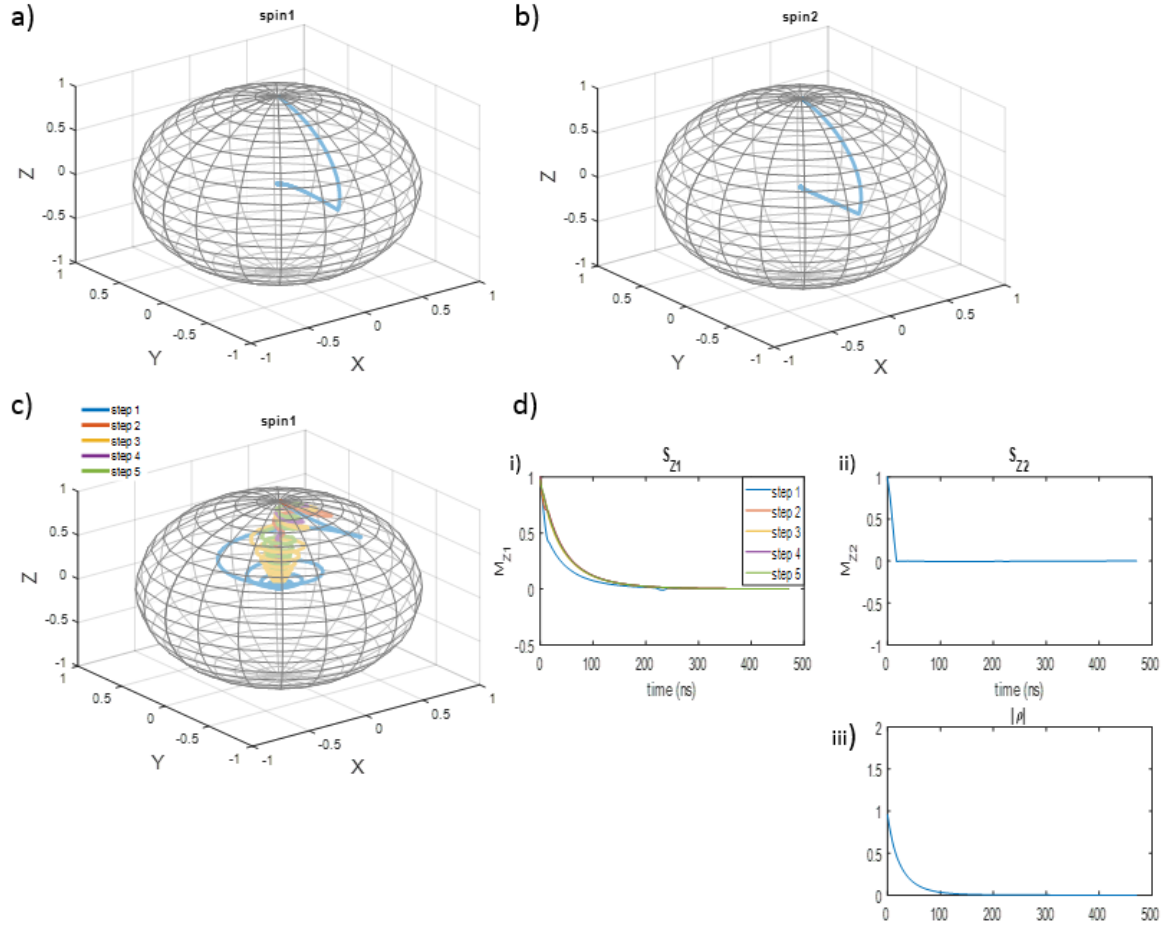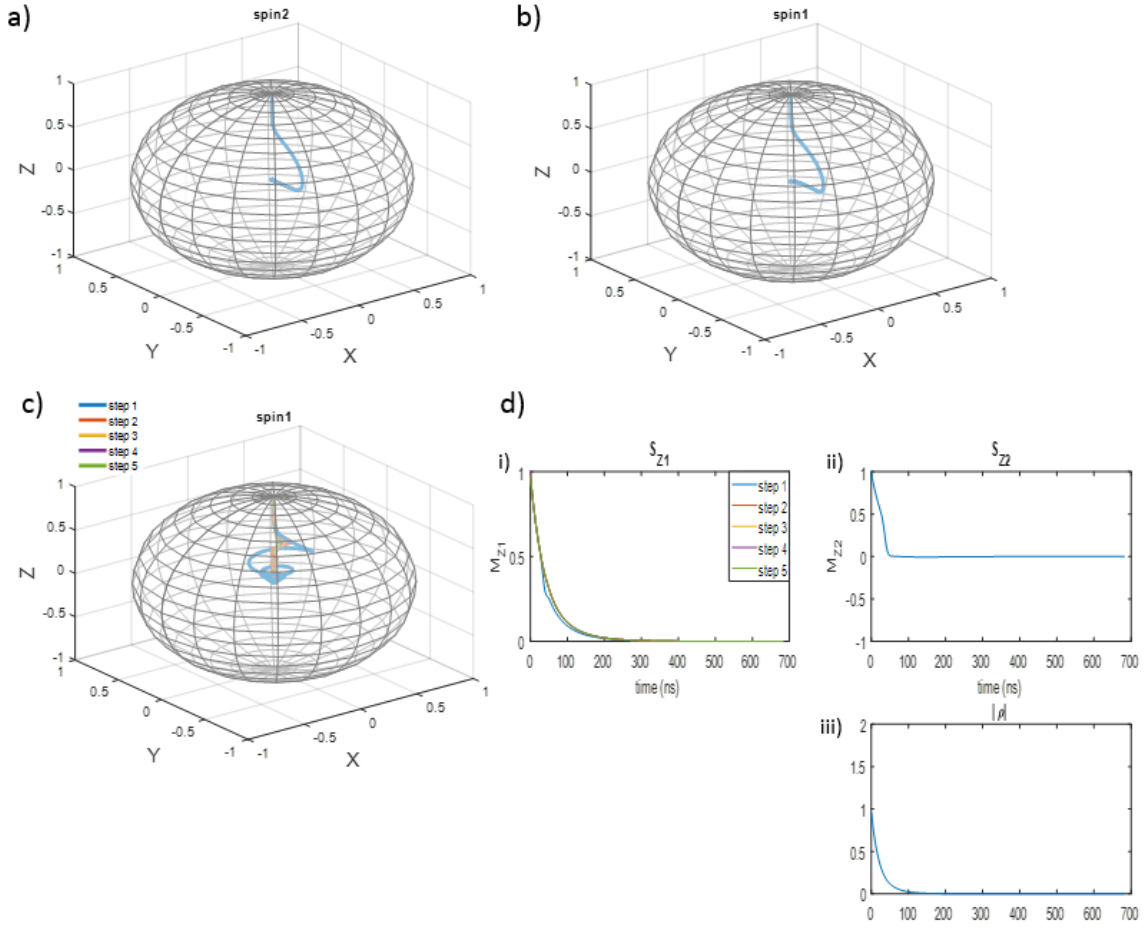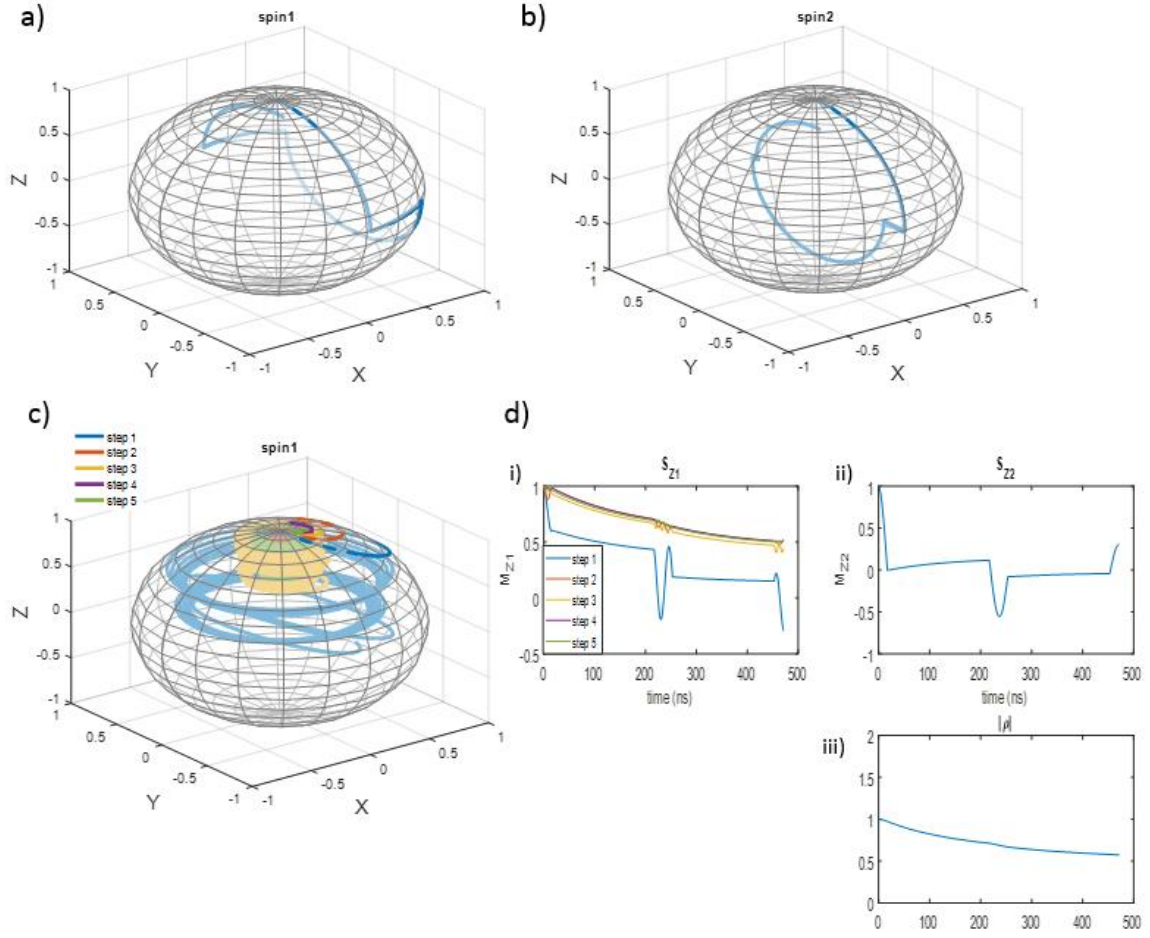
Figure 5.14: The magnetization movement for two spins (both initially up, on and off resonance) on the Bloch sphere including **recombination and spin relaxation** with singlet and triplet recombination rates $r_s = 1/8.5\ \mu s^{-1}$, $r_T = 1/25\ \mu s^{-1}$ respectively, and spin lattice relaxation times $T_{1_e} = 8.5\ \mu s$, $T_{1_h} = 8.5\ \mu s$, and spin-spin relaxation times $T_{2_e} = 0.8\ \mu s$, $T_{2_h} = 1.1\ \mu s$ for both spins respectively. a) with detuning in at ($B_{z1max} = 2\ mT$) through 100 steps, b) without detuning ($B_{z1max} = 0\ mT$) through 100 steps, c) with detuning at ($B_{z1max} = 4\ mT$) through 5 steps where ($B_{z1} = n \times B_{z1max} / (steps\ no. -1),\ n = 1: steps\ no.$), d) Sz1 and Sz2 show the magnetization movement on Cartesian along the time i) with detuning at ($B_{z1max} = 4\ mT$) through 5 steps, ii) without detuning ($B_{z1max} = 0\ mT$) and iii) the spin density for **square** pulse.
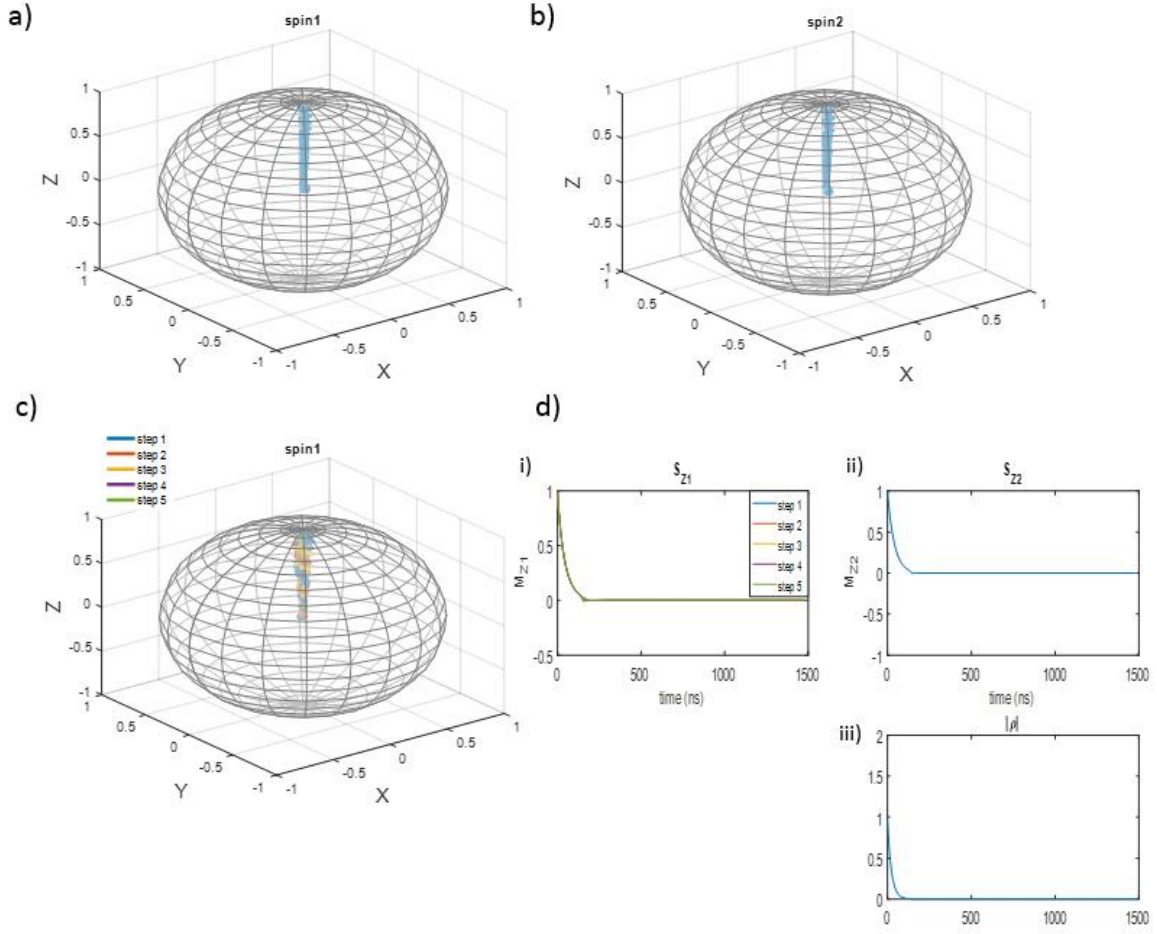
Figure 5.15: The magnetization movement for two spins (both initially up, on and off resonance) on the Bloch sphere including **recombination and spin relaxation** with singlet and triplet recombination rates $r_s = 1/8.5 \, \mu s^{-1}$, $r_T = 1/25 \, \mu s^{-1}$ rrespectively, and spin lattice relaxation times $T_{1_e} = 8.5 \, \mu s$, $T_{1_h} = 8.5 \, \mu s$, and spin-spin relaxation times $T_{2_e} = 0.8 \, \mu s$, $T_{2_h} = 1.1 \, \mu s$ for both spins respectively. a) with detuning in at ($B_{z1max} = 2 \, mT$) through 100 steps, b) without detuning ($B_{z1max} = 0 \, mT$) through 100 steps, c) with detuning at ($B_{z1max} = 4 \, mT$) through 5 steps where ($B_{z1} = n \times B_{z1max} / (steps \, no. - 1), \, n = 1: steps \, no.$), d) Sz1 and Sz2 show the magnetization movement on Cartesian along the time i) with detuning at ($B_{z1max} = 4 \, mT$) through 5 steps, ii) without detuning ($B_{z1max} = 0 \, mT$) and iii) the spin density for **Gaussian** pulse.

Figure 5.16: The magnetization movement for two spins (both initially up, on and off resonance) on the Bloch sphere including **recombination and spin relaxation** with singlet and triplet recombination $r_s = 1/8.5\ \mu s^{-1}$, $r_T = 1/25\ \mu s^{-1}$ respectively, and spin lattice relaxation times $T_{1_e} = 8.5\ \mu s$, $T_{1_h} = 8.5\ \mu s$, and spin-spin relaxation times $T_{2_e} = 0.8\ \mu s$, $T_{2_h} = 1.1\ \mu s$ for both spins respectively. a) with detuning in at ($B_{z1max} = 2\ mT$) through 100 steps, b) without detuning ($B_{z1max} = 0\ mT$) through 100 steps, c) with detuning at ($B_{z1max} = 4\ mT$) through 5 steps where ($B_{z1} = n \times B_{z1max}/ (steps\ no. -1)$, $n = 1:steps\ no.$), d) Sz1 and Sz2 show the magnetization movement on Cartesian along the time i) with detuning at ($B_{z1max} = 4\ mT$) through 5 steps, ii) without detuning ($B_{z1max} = 0\ mT$) and iii) the spin density for **chirp** pulse.

I now turn to investigating the ability of adiabatic pulses to increase the fidelity and uniformity of spin rotations and increase the excitation bandwidth. Figures 5.17 and 5.18 show Mz_1 and My_1 for simulation square, Gaussian, and chirp pulses

a) Ideal pulse   **b) Recombination**   **c) Recombination and Relaxation**
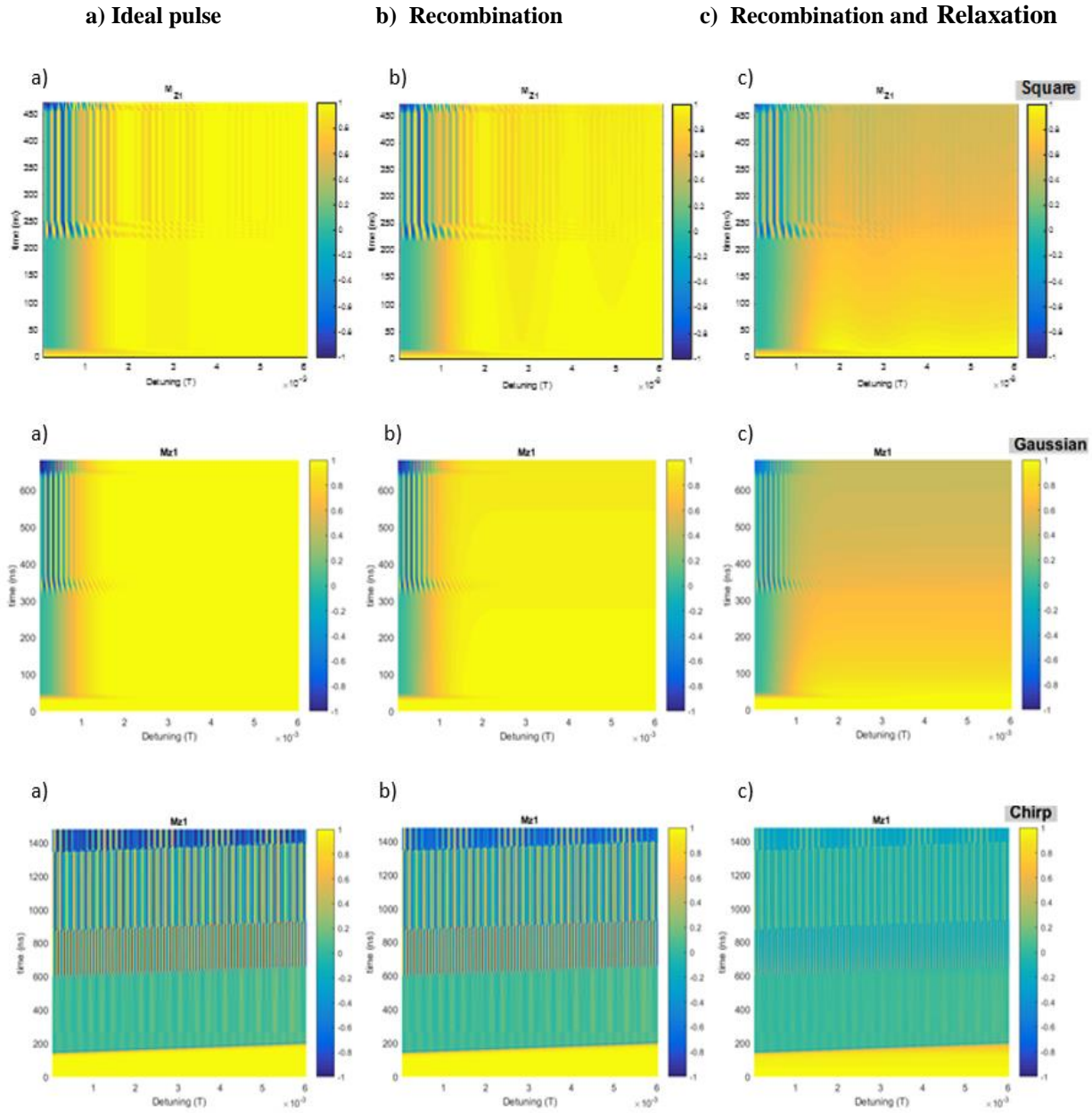
Figure 5.17: Simulations of Mz_1 as a function of time and detuning for **Square, Gaussian and Chirp pulses** including recombination and spin relaxation. a) Hahn echo simulation for square pulse b) with recombination c) with recombination and relaxation where singlet and triplet recombination rates $r_s = 1/8.5 \, \mu s^{-1}$, $r_T = 1/25 \, \mu s^{-1}$ respectively, and spin lattice relaxation times $T_{1_e} = 8.5 \, \mu s$, $T_{1_h} = 8.5 \, \mu s$, and spin-spin relaxation times $T_{2_e} = 0.8 \, \mu s$, $T_{2_h} = 1.1 \, \mu s$ for both spins respectively.

Figure 5.18: Simulations of My_1 as a function of time and detuning for **Square, Gaussian, and Chirp pulses** including recombination and spin relaxation. a) Hahn echo simulation for square pulse b) with recombination c) with recombination and relaxation where singlet and triplet recombination rates $r_s = 1/8.5 \, \mu s^{-1}$, $r_T = 1/25 \, \mu s^{-1}$ respectively, and spin lattice relaxation times $T_{1_e} = 8.5 \, \mu s$, $T_{1_h} = 8.5 \, \mu s$, and spin-spin relaxation times $T_{2_e} = 0.8 \, \mu s$, $T_{2_h} = 1.1 \, \mu s$ for both spins respectively.
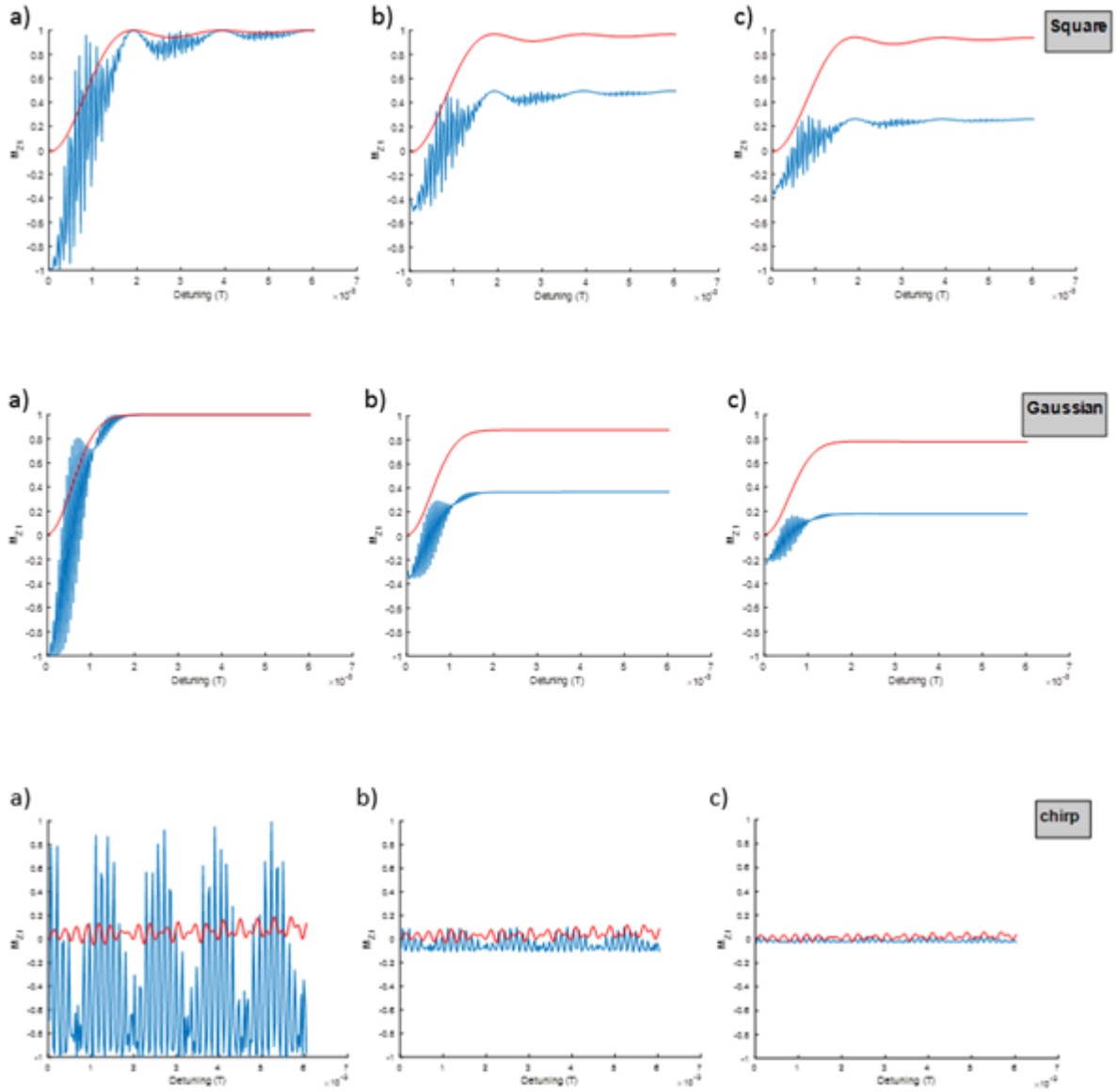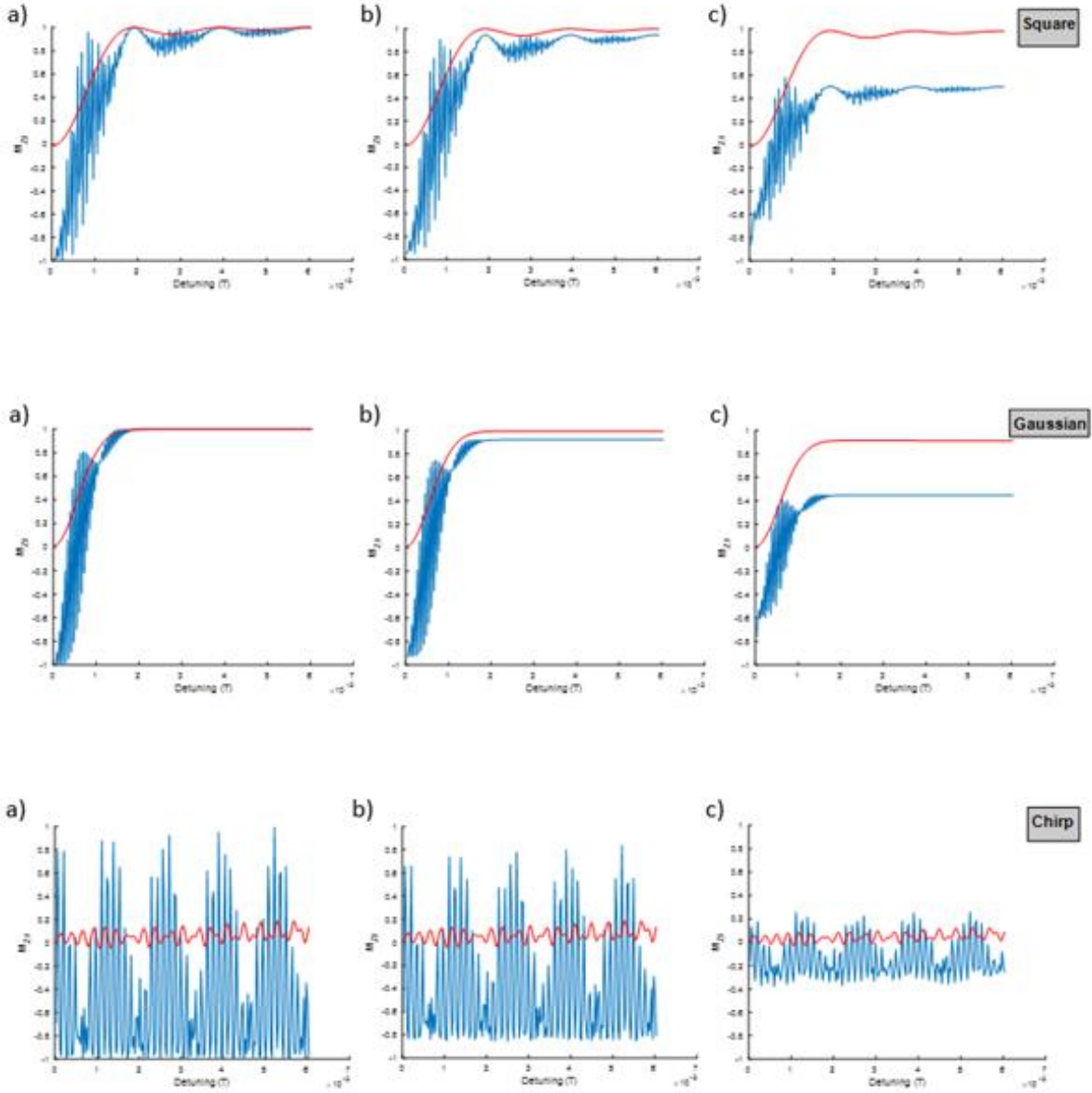
Figure 5.19: Mz_1 following a $\pi/2$ pulse (red) and Hahn echo sequence (blue) $[\pi/2^{\text{sq},18\text{ns}} : \tau^{200\text{ns}} : \pi^{\text{sq},36\text{ns}} : \tau^{200\text{ns}} : -\pi/2^{\text{sq},18\text{ns}}]$, $[\pi/2^{\text{G},71\text{ns}} : \tau^{\text{G},200\text{ns}} : \pi^{\text{G},141\text{ns}} : \tau^{\text{G},200\text{ns}} :- \pi/2^{\text{G},71\text{ns}}]$, and $[\pi/2^{\text{Ch},270\text{ns},400\text{MHz}} : \tau^{\text{Ch},200\text{ns}} : \pi^{\text{Ch},540\text{ns},400\text{MHz}} : \tau^{\text{Ch},100\text{ns}} : - \pi/2^{\text{Ch},270\text{ns},400\text{MHz}}]$ as a function of detuning for **Square, Gaussian, and Chirp pulses** respectively, b) including recombination, c) including recombination and spin relaxation where singlet and triplet recombination rates $r_s = 1/8.5\ \mu\text{s}^{-1}$, $r_T = 1/25\ \mu\text{s}^{-1}$ respectively, and spin lattice relaxation times $T_{1_e} = 8.5\ \mu\text{s}$, $T_{1_h} = 8.5\ \mu\text{s}$, and spin-spin relaxation times $T_{2_e} = 0.8\ \mu\text{s}$, $T_{2_h} = 1.1\ \mu\text{s}$ for both spins respectively.

Fig 5.19 shows the simulation signals of Mz_1 following a $\pi/2$ pulse (red) and Hahn echo sequence (blue) as a function of detuning, where the detuning $B_{z1max} = 6\, mT$ through 200 steps for square, Gaussian and chirp pulse with real parameters, the red line is the excitation bandwidth after $\pi/2$ pulse and the blue after the whole sequence ($\pi/2$, π, $-\pi/2$). It proves the outcome from section 5.2.4 with real parameters from the experiment, if we are trying to compete with recombination and relaxation processes that on the same time scale, then the faster and shorter sequence with lower fidelity gives a better outcome than the slower and longer sequence with high fidelity. Therefore, a simple pulse sequence is better than a complex pulse.

The result from modeling using experimentally determined parameters gives the same outcome demonstrated in sec 5.2.4. Gaussian and chirp pulses work better and produce higher fidelity operation compared to square pulse in the ideal case due to the pulse length. However, a square pulse is better and has higher fidelity for both recombination and recombination with relaxation due to the fact that faster pulse has less recombination which leads to higher fidelity. More reduction in the fidelity has been observed when spin relaxation is included in the simulations due to its impact on the transient behaviour of the pair recombination rate.

5.3 Fidelity on realistic disorder function:

Tables below demonstrate a comparison of the fidelity of square, Gaussian, and chirp pulses including spin recombination and relaxation where singlet and triplet recombination rates $r_s = 1/8.5\ \mu s^{-1}$, $r_T = 1/25\ \mu s^{-1}$ respectively, and spin lattice relaxation times $T_{1_e} = 8.5\ \mu s$, $T_{1_h} = 8.5\ \mu s$, and spin-spin relaxation times $T_{2_e} = 0.8\ \mu s$, $T_{2_h} = 1.1\ \mu s$ for both spins respectively, and $B_{1max} = 0.5\ mT$, $B_{z1max} = 6\ mT$ through 100 steps along 472 ns, 683 ns, and 1480 ns for square, Gaussian and chirp pulse respectively.

As the target state is Mz = -1, we define the fidelity of a pulse on a single spin with a given detuning to be

$$F_z(B_z) = -1/2(M_z(B_z) - 1) \tag{5.14}$$

The fidelity of a single spin operation on the entire ensemble of spins is then calculated by:

$$F^{ens} = \frac{\sum_{B_{z1}} G^{\Delta B_1}(B_{z1}) F_{z1}(B_{z1})}{\sum_{B_{z1}} G^{\Delta B_1}(B_{z1})} \tag{5.15}$$

And for operation on an ensemble of pairs of spins:

$$F^{ens} = \frac{\sum_{B_{z1}} \sum_{B_{z2}} G^{\Delta B_1}(B_{z1})\ F_{z1}(B_{z1})\ G^{\Delta B_2}(B_{z2})\ F_{z2}(B_{z2})}{\sum_{B_{z1}} \sum_{B_{z2}} G^{\Delta B_1}(B_{z1})\ G^{\Delta B_2}(B_{z2})} \tag{5.16}$$

108

where $G^{\Delta B_1}$ and $G^{\Delta B_2}$ are normalised Gaussian functions with the spectra linewidth from the experiment section 4.3.1, $M_{z1}(B_{z1})$ and $M_{z2}(B_{z2})$ are the spin magnetization, F_{z1} and F_{z2} are the fidelity of a pulse on spin 1 and 2 respectively, and B_{z1} and B_{z1} refer to the detuning. Tables below demonstrate a comparison of the fidelity of a single spin operation on the entire ensemble of spins for square, Gaussian and chirp pulses with recombination and relaxation; in table 5.2 we used the spectra linewidth from the experiment, while in tables 5.3 and 5.4 used different assumptions of spectra linewidth.

	Ideal	recombination	Relaxation	recombination + relaxation
Square	0.3203	0.3306	0.4217	0.4262
Gaussian	0.2878	0.3054	0.4133	0.4202
Chirp	0.7507	0.7138	0.5973	0.5827

Table 5.2: The ensemble fidelity F^{ens} of square, Gaussian, and chirp pulses with spin recombination and relaxation at $\Delta B_1 = 2.06$ mT .

	Ideal	recombination	Relaxation	recombination + relaxation
Square	0.9347	0.9133	0.8295	0.8129
Gaussian	0.9892	0.9545	0.8271	0.8033
Chirp	0.7151	0.6871	0.6144	0.5997

Table 5.3: The ensemble fidelity F^{ens} of square, Gaussian, and chirp pulses with spin recombination and relaxation at $\Delta B_1 = 0.206\ mT$.

	Ideal	recombination	Relaxation	recombination + relaxation
Square	0.9811	0.9589	0.8796	0.8616
Gaussian	0.9996	0.9661	0.8485	0.8246
Chirp	0.6753	0.6571	0.6298	0.6152

Table 5.4: The ensemble fidelity F^{ens} of square, Gaussian, and chirp pulses with spin recombination and relaxation at $\Delta B_1 = 0.1\ m\ T$.

From the fidelity tables for ensemble of differnt widths, we see that if $B_{1max} > \Delta B_1$ then the Gaussian pulse is better for the ideal case and for the case with recombination only, while the square pulse scheme is better for situations with recombination and spin relaxation or with spin relaxation only. However, when $B_{1max} < \Delta B_1$, then the chirp pulse is better compared to Gaussian and square pulses. Figure 5.20 demonstrate the compasion of $(G^{\Delta B_1} (B_{z1}) \; F_z(B_{z1}))$ (blue) and normalised Gaussian functions $G^{\Delta B_1}$ (red) with $\Delta B_1 = 2.06$ mT in a) and $\Delta B_1 = 0.1$ mT in b) as a function of detuning for **square, Gaussian, and chirp pulses.** These figures include recombination and spin relaxation where singlet and triplet recombination rates $r_s = 1/8.5 \, \mu s^{-1}$, $r_T = 1/25 \, \mu s^{-1}$ respectively, and spin lattice relaxation times $T_{1_e} = 8.5 \, \mu s$, $T_{1_h} = 8.5 \, \mu s$, and spin-spin relaxation times $T_{2_e} = 0.8 \, \mu s$, $T_{2_h} = 1.1 \, \mu s$ for both spins respectively.
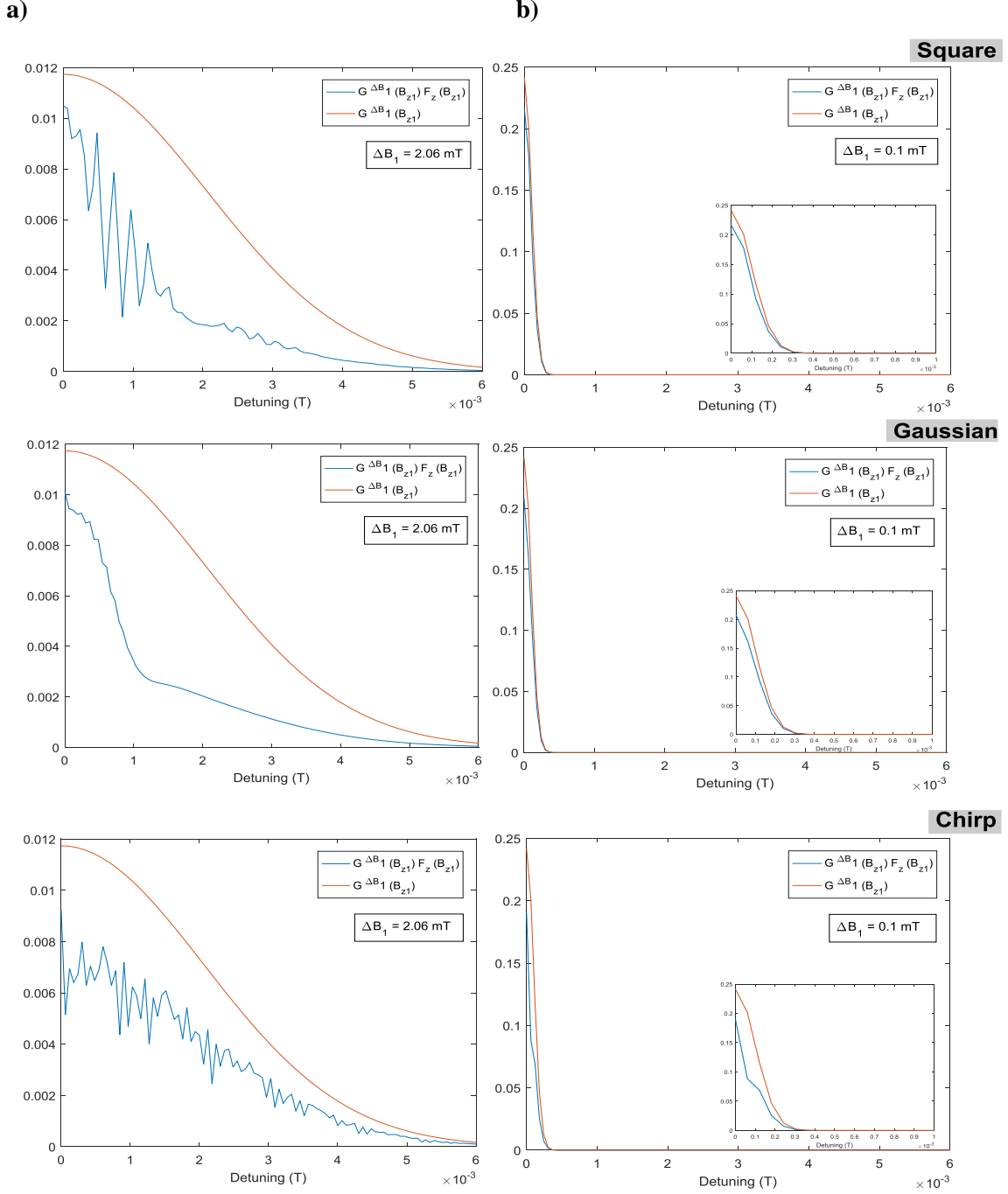
Figure 5.20: Comparison of $(G^{\Delta B_1}(B_{z1})F_z(B_{z1}))$ (blue) and normalised Gaussian functions with the spectra linewidth $(G^{\Delta B_1})$ (red) with different values of ΔB_1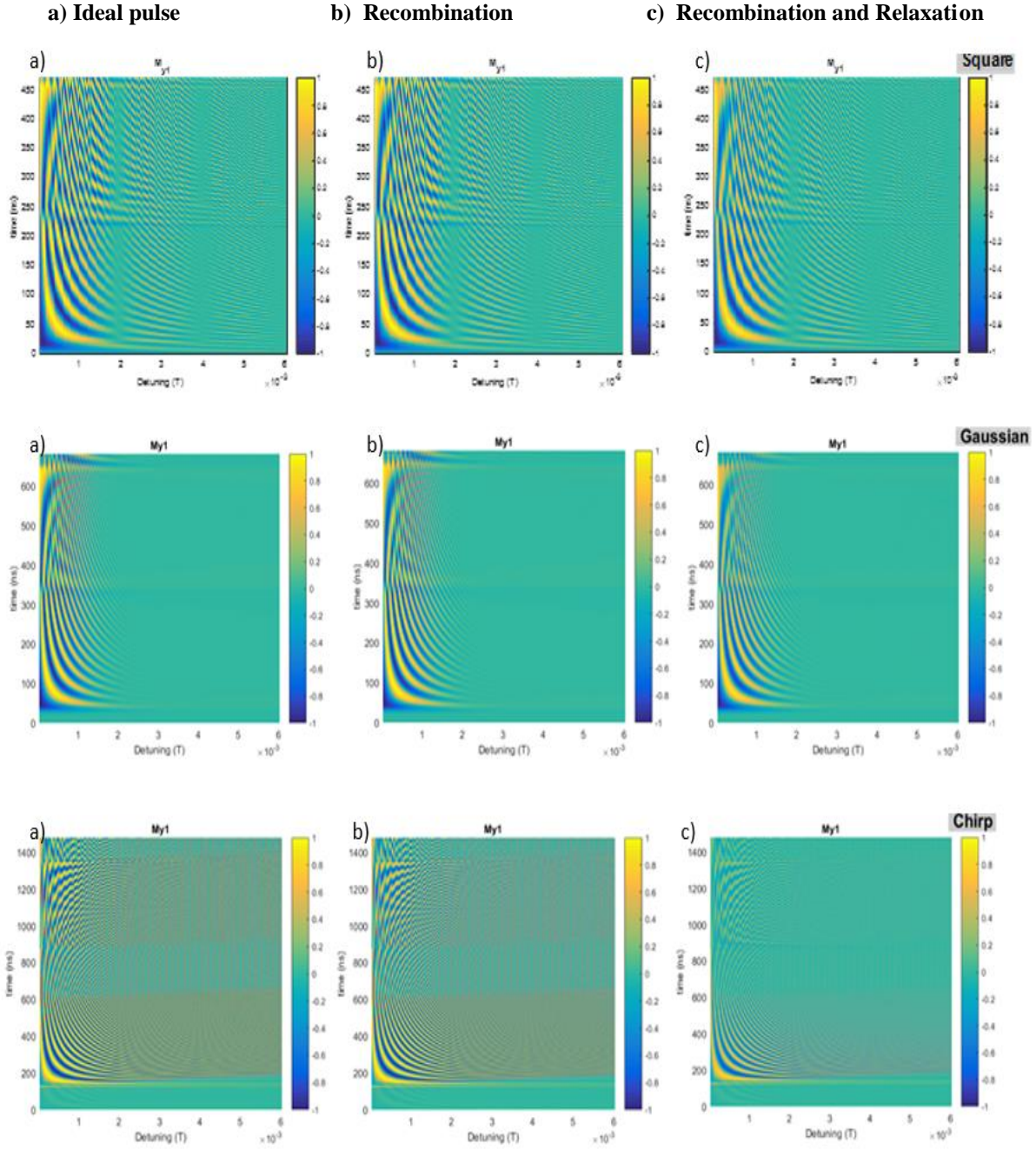 in a) and b) as a function of detuning for **Square, Gaussian, and Chirp pulses** including recombination and spin relaxation where singlet and triplet recombination rates $r_s = 1/8.5 \,\mu s^{-1}$, $r_T = 1/25 \,\mu s^{-1}$ respectively, and spin lattice relaxation times $T_{1_e} = 8.5 \,\mu s$, $T_{1_h} = 8.5 \,\mu s$, and spin-spin relaxation times $T_{2_e} = 0.8 \,\mu s$, $T_{2_h} = 1.1 \,\mu s$ for both spins respectively. A zoom of low detuning when $\Delta B_1 = 0.1$ mT is shown in the inset.

From Fig. 5.20, square pulse produced better shape of $(G^{\Delta B_1}(B_{z1})\,F_z(B_{z1}))$ when $\Delta B_1 = 0.1$ mT while the chirp pulse is better at $\Delta B_1 = 2.06$ mT.

Table 5.5 below demonstrate a comparison of the fidelity for operation on an ensemble of pairs of spins for square, Gaussian and chirp pulses with recombination and relaxation, we used the two spectra linewidth from the experiment. It is clearly seen that the chirp pulse produces better fidelity compared to square and Gaussian in all cases.

	Ideal	recombination	Relaxation	recombination + relaxation
Square	0.0662	0.0711	0.0976	0.1021
Gaussian	0.0497	0.0569	0.0962	0.1027
Chirp	0.5632	0.5220	0.4304	0.4078

Table 5.5: The ensemble fidelity F^{ens} of pairs of spins for square, Gaussian, and chirp pulses with spin recombination and relaxation at $\Delta B_1 = 2.06$ mT and at $\Delta B_2 = 4.14$ mT.

Fig 5.21 provides a comparison of $(G^{\Delta B}(B_z)F_z(B_z))$ and normalised Gaussian functions with the spectra linewidth $(G^{\Delta B})$ for two spins as a function of detuning for **square, Gaussian, and chirp pulses** respectively, at $\Delta B_1 = 2.06$ mT and at $\Delta B_2 = 4.14$ mT . This fig shows the comparison for ideal pulse in a), and pulse including recombination and spin relaxation in b) where singlet and triplet recombination rates $r_s = 1/8.5\ \mu s^{-1}$, $r_T = 1/25\ \mu s^{-1}$ respectively, and spin lattice relaxation times $T_{1_e} = 8.5\ \mu s$, $T_{1_h} = 8.5\ \mu s$, and spin-spin relaxation times $T_{2_e} = 0.8\ \mu s$, $T_{2_h} = 1.1\ \mu s$ for both spins respectively. From that fig. Square pulse produced better shape of $(G^{\Delta B_1}(B_{z1})\,F_z(B_{z1}))$ when $\Delta B_1 = 0.1$ mT while the chirp pulse is better at $\Delta B_1 = 2.06$ mT. From this fig the fidelity operation on an ensemble of pairs of spins is higher in chirp pulse compared to square and Gaussian pulses.
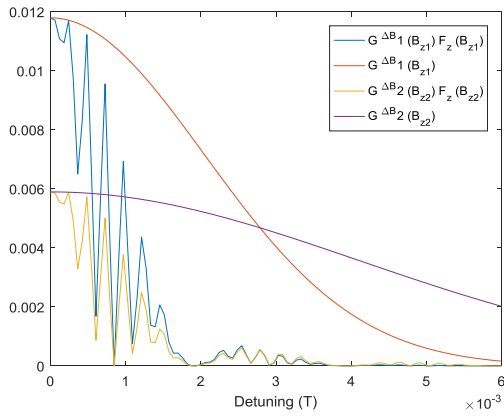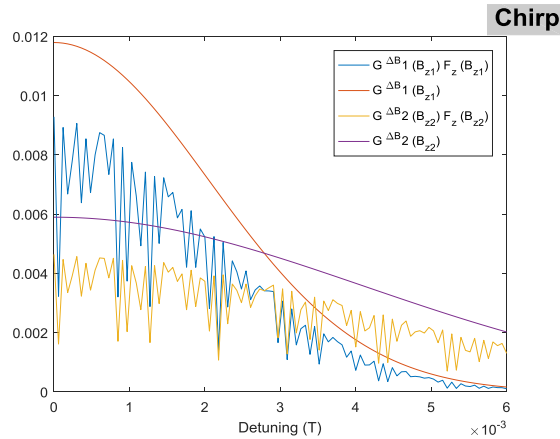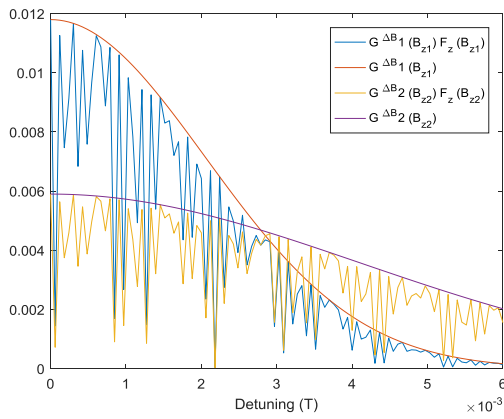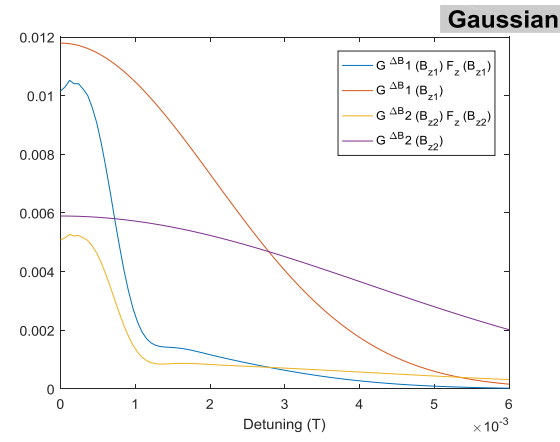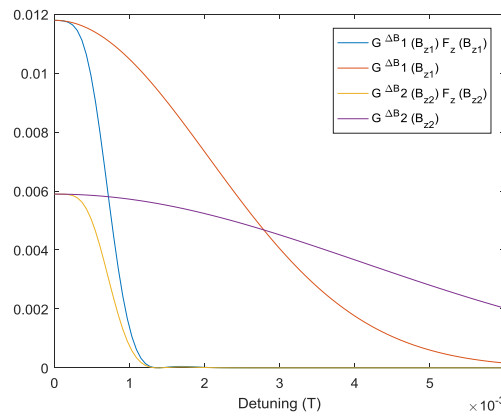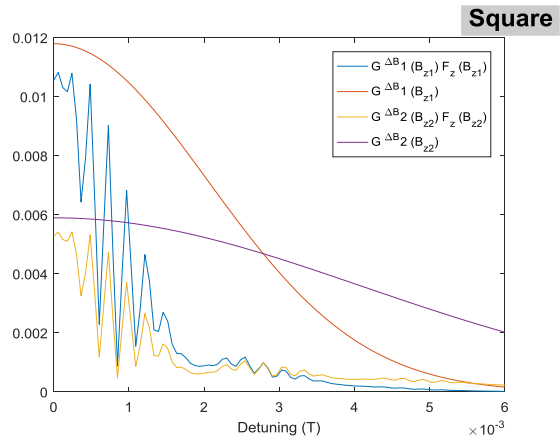
Figure 5.21: Comparison of $(G^{\Delta B}(B_z)F_z(B_z))$ and normalised Gaussian functions with the spectra linewidth $(G^{\Delta B})$ for two spins as a function of detuning for **Square, Gaussian, and Chirp pulses** respectively, a) for ideal pulse, b) pulse including recombination and spin relaxation where singlet and triplet recombination rates $r_s = 1/8.5\,\mu s^{-1}$, $r_T = 1/25\,\mu s^{-1}$ respectively, and spin lattice relaxation times $T_{1_e} = 8.5\,\mu s$, $T_{1_h} = 8.5\,\mu s$, and spin-spin relaxation times $T_{2_e} = 0.8\,\mu s$, $T_{2_h} = 1.1\,\mu s$ for both spins respectively.

113
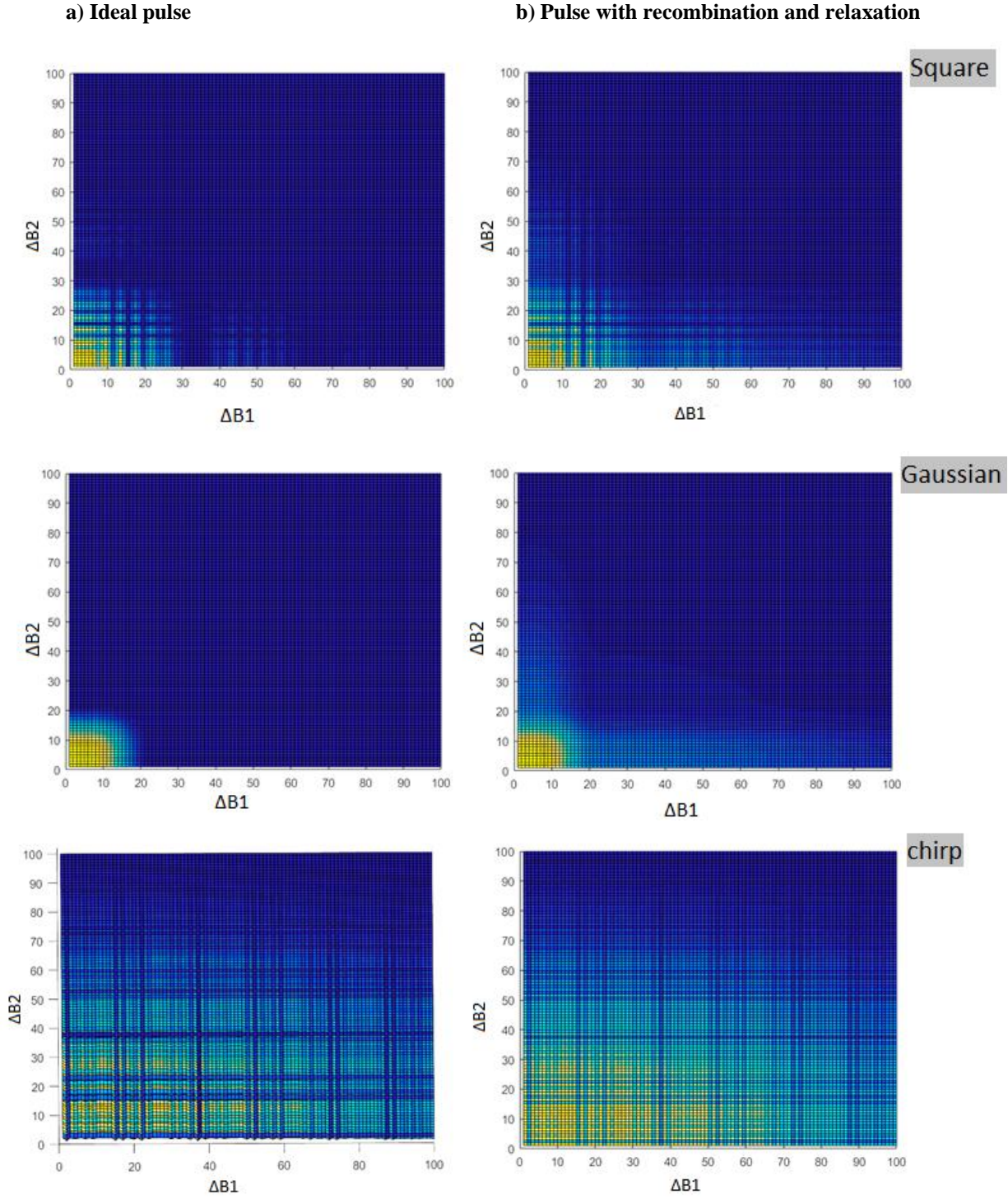
Figure 5.22: Fidelity for two spins as a function of detuning for **Square, Gaussian, and Chirp pulses** respectively, a) for ideal pulse, b) pulse including recombination and spin relaxation where singlet and triplet recombination rates $r_s = 1/8.5\ \mu s^{-1}$, $r_T = 1/25\ \mu s^{-1}$ respectively, and spin lattice relaxation times $T_{1_e} = 8.5\ \mu s$, $T_{1_h} = 8.5\ \mu s$, and spin-spin relaxation times $T_{2_e} = 0.8\ \mu s$, $T_{2_h} = 1.1\ \mu s$ for both spins respectively.

Fig 5.22 demonstrate the fidelity for operation on an ensemble of pairs of spins as a function of detuning where the detuning $B_{z1max} = 6\,mT$ through 100 steps for **square, Gaussian, and chirp** pulses respectively, a) for pure pulse, b) pulse including recombination and spin relaxation where singlet and triplet recombination rates $r_s = 1/8.5\,\mu s^{-1}$, $r_T = 1/25\,\mu s^{-1}$ respectively, and spin lattice relaxation times $T_{1_e} = 8.5\,\mu s$, $T_{1_h} = 8.5\,\mu s$, and spin-spin relaxation times $T_{2_e} = 0.8\,\mu s$, $T_{2_h} = 1.1\,\mu s$ for both spins respectively.

We have shown that using Gaussian shaped pulses or chirp adiabatic pulses leads to improved fidelity response of OLEDs devices with realistic dephasing mechanisms and carrier lifetimes. However, this improvement is the result of increasing pulse length because they have better ability to rotate slightly off resonance spins with higher fidelity than the square pulse which has a faster sequence with low fidelity.. The specific details of the permutation symetry along the trajectory that is traversed during the pulse sequence impacts the resulting fidelity. If we can find a route that minimises the non-triplet states, we maximise the fidelity in systems where the triplet recombination rate is slower than the singelt recombination rate, and where recombination rate is the dominant timescale.

A significant insight provided by this thesis is that there are meaningful differences during spin evolution of spin-pairs compared to single spins, related to the influence of permutation symmetry on recombination. This is seen more strongly during adiabatic pulses, which tend to take longer to apply, and which can lead to non-trivial trajectories and correspondingly non-trivial recombination dynamics.

In retrospect, the insights above could perhaps have been inferred from earlier work on pulse EPR, however, to our knowledge this is the first time that this effect has been described. Previous studies have considered the starting and ending point to be changed in symmetry, but they didn't consider the impact of changes in the symetry during the pulse. This is likely due to the fact that spins in conventional EPR measuremtns generally take similar paths, and the prior work on adiabatic pulses in EPR focused on fidelity of singel spin operations. The work described above is different from the conventionally EPR system, and represents a new insight for systems comprised of spin-pairs. The theoretical results in this chapter are significant for future work which could explore the design and optimisation of trajectories with the aim of minimizing these effects.

Chapter 6. Conclusion and outlook

Conclusion

The significant interest in understanding the underlying spin properties in organic electronics has led to the development of spin-based technologies such as spin resonance-based magnetometers.

In this thesis, we have presented a primarily theoretical investigation of approaches that may be used to overcome challenges such as inhomogeneous disorder in these materials by using suitably designed adiabatic pulses in EDMR techniques. We have also extended previous efforts in this area to include the influence of recombination and spin relaxation on the models investigated. We demonstrated the solution of Liuoville equation for a two spins polaron pair which includes the spin Hamiltonian, charge carrier recombination as well as spin relation characterization.

We have developed OLED device processing recipes, performed device optimization, and undertaken stability measurements. We confirmed that the improved processes lead to increased device performance with high emission.

We have developed a number of magnetic field sensing techniques based on spin OLEDs devices which exploits these advances. We have modelled EDMR response of OLEDs devices with realistic dephasing mechanisms and carrier lifetimes and shown theoretically that using adiabatic pulses improves the sensitivity of pEDMR techniques. The fidelity enhancement and optimized shaped pulses compensate for decoherence pathways and lead to an increase in the gained frequencies precision which effected by Hahn echo large amplitude.

In this thesis, we investigated three different types of pulses, and we have seen that the fidelity of a single spin operation on the entire ensemble of spins and for pair of spins with the spectra linewidth resulted from the experiment is better in chirp pulse compared to square and Gaussian when both recombination and spin relaxation are considered. In particular, using OLEDs devices with MEH-PPV for field sensing with realistic dephasing mechanisms and carrier lifetimes, and one of the challenges is inhomogeneous broadening. Thus, at the end of this thesis, we demonstrate the ability to use adiabatic pulses scheme to improve the fidelity. We have seen that when including recombination and spin relaxation the fidelity of a *single* spin operation on the entire ensemble of spins reached 58 %, 42 %, and 43 % for a chirp, Gaussian, and square pulses respectively. The fidelity for operation on an ensemble of *pairs* of spins reached 41%, 10%, and 10% for chirp, Gaussian, and square pulses respectively. Adiabatic pulses therefore have a larger influence on the fidelity of control in systems consisting of pairs of spins, which are central to electrically and optically detected techniques, and therefore should be considered at lower error thresholds in those systems.

This thesis has provided a clear understanding of differences during spin evolution of spin-pairs compared to single spins, related to the influence of permutation symmetry on recombination. This has a significant impact during adiabatic pulses, which in general take longer to apply. Although earlier work on applying shaped pulses in EPR has demonstrated that fidelities are improved, the application to spin-pairs led to a new insight related to the role that the trajectory of the spins in the pair has on their recombination dynamics. We also illustrate the influence that recombination and spin decoherence has on this fidelity improvement, which differs from conventional EPR experiments.

Finally, we describe a fidelity loss mechanism which arises uniquely in pairs of spins, namely that the joint trajectory of the spins can modify the permutation symmetry of the pairs, and this can lead to modification of the recombination rate for trajectories that would be considered equivalent in isolated spin systems with magnetization readout. The theoretical results are important for future application and should be effective with some experimental implementation of spin based sensing. In particular, by choosing trajectories which result in less recombination, the fidelity of operations on pairs can be enhanced even when the fidelity of equivalent single spin operations are identical.

In the future, this approach may be able to be extended to a range of other systems where spin pair permutation symmetry plays a role. The insights gained in this thesis and the modelling code included below should allow other researchers to extend on this work in those contexts in the future.

Appendix A

Superoperator simulation for two spins ½ system

The superoperator Liouville formalism with a set of 16x16 matrix as discussed in Chapter 5 has been implemented in Matlab. Solving the stochastic Liouville equation to describe the dynamics of a statistical ensemble of two spins polaron pairs ½ particles subject to a time-dependent driving field and subject to recombination and decoherence mechanisms is the aim for this simulation.

The superoperator Liouville equation is:

$$\frac{d\hat{\rho}}{dt} = -\frac{i}{\hbar}[\hat{\rho}, \widehat{H}] + \hat{S}[\hat{\rho}] + \widehat{R}\{\hat{\rho} - \hat{\rho}_0\} \tag{A.1}$$

$\widehat{H}$ is Hamiltonian for the summation time dependent and independent and written as:

$$\widehat{H}(t) = \widehat{H}_0 + \widehat{H}_1(t) \tag{A.2}$$

$\hat{S}$ is the recombination operator:

$$\hat{S} = -r_s . \hat{S}_s - r_t . \hat{T}_s \tag{A.3}$$

Both $\widehat{H}$ and $\hat{S}$ are in Hilbert space 4x4 matrix and need to transform to Liuoville space 16x16 matrix, so the identity operator is used:

The Hamiltonian superoperator is:

$$\widehat{H}_{super} = i\widehat{H} \otimes \hat{I} - i\hat{I} \otimes \widehat{H} \tag{A.4}$$

And the recombination superoperator is:

$$\hat{S}_{super} = \hat{S} \otimes \hat{I} + \hat{I} \otimes \hat{S} \tag{A.5}$$

$\widehat{R}$ is the spin relaxation superoperator:

$$\widehat{R}\{\hat{\rho}(t) - \hat{\rho}_0\} = \widehat{R}_{e/h} \otimes \hat{I} + \hat{I} \otimes \widehat{R}_{e/h} \tag{A.6}$$

$\widehat{R}_e$ has been define in Appendix C.

Starting with defining the density initial state ρ_0 for the two spins polaron pairs in the product base as shown below:

$$| \Psi > = | \Psi_1 > < \Psi_2 | = \begin{pmatrix} 1 \\ 0 \end{pmatrix} \otimes \begin{pmatrix} 1 \\ 0 \end{pmatrix} = C \tag{A.8}$$

$$\rho_0 = C'.C = \begin{bmatrix} 1 & 0 & 0 & 0 \\ 0 & 0 & 0 & 0 \\ 0 & 0 & 0 & 0 \\ 0 & 0 & 0 & 0 \end{bmatrix} \tag{A.9}$$

118

Then convert the density initial state from Hilbert space (4x4) to Liouville density vector to (16 x 1).

The spin Hamiltonian $\hat{H}_{super}$ is calculated in Liouville space for the two spins with different Overhauser field B_{z1} & B_{z2} and (a constant driving field) applied magnetic field B_x and produces 16 x 16 matrix size.

Also, the recombination $\hat{S}_{super}$ is calculated in Liouville space and given 16 x 16 matrix with given values to singlet and triplet recombination rate $r_s = 1/10\,e^{-6}\ S^{-1}$, $r_T = 1/10\,e^{-8}\ S^{-1}$ respectively. where the super observable is:

$$\hat{O}_{super} = Trace(\hat{O}^{\dagger}\rho(t)) \tag{A.10}$$

Transforming the density matrix is implemented with the following equation:

$$\hat{\rho} = \begin{bmatrix} a_{1,1} & a_{1,2} & \cdots & a_{1,n} \\ a_{2,1} & a_{2,3} & \cdots & a_{2,n} \\ \vdots & \vdots & \ddots & \vdots \\ a_{m,1} & a_{m,2} & \cdots & a_{m,n} \end{bmatrix} \rightarrow \begin{bmatrix} a_{1,1} \\ a_{1,2} \\ a_{1,3} \\ \vdots \\ a_{m,n} \end{bmatrix} \tag{A.11}$$

```
%% System
ub=9.274e-24;          %J/T
hbar= 1.0545718e-34;   %J*s
g1=2.0023;             %g factor for spin 1
g2=2.0023;             %g factor for spin 2
dt=01e-9;              %pulse step size in sec


_____
%%  square pulse

 Bmax=0.5e-3;    %microwave field in T
 B1=Bmax;

 [Bxp1,Byp1] = Create_theta_Pulse(Bmax,pi()/2,g1,dt);
 [Wx1,Wy1] = Create_wait_time(200e-9,dt);
 [Bxp2,Byp2] = Create_theta_Pulse(Bmax,pi(),g1,dt);
 [Wx2,Wy2] = Create_wait_time(200e-9,dt);
 [Bxp3,Byp3] = Create_theta_Pulse(Bmax,pi()/2,g1,dt);
 Bx=[Bxp1' Wx1' Bxp2' Wx2' -Bxp3']';
 By=[Byp1' Wy1' Byp2' Wy2' -Byp3']';
 %Bx=[Bxp1' Wx1' Bxp2' Wx2' Bxp3']';  %use for pi/2, pi, pi/2 pulse
sequence
 %By=[Byp1' Wy1' Byp2' Wy2' Byp3']';  %use for pi/2, pi, pi/2 pulse
sequence

 steps = length(Bx);
 t=linspace(0, steps-1, steps)*dt;


_____
%% Gaussian Pulse

 Bmax=0.5e-3;    %microwave field in T
 B1=Bmax;
```

```matlab
[Bxp1,Byp1] = Create_Gauss_Pulse(Bmax,pi()/2,g1,dt);   %pi()/4
[Wx1,Wy1] = Create_wait_time(200e-9,dt);
[Bxp2,Byp2] = Create_Gauss_Pulse(Bmax,pi(),g1,dt);
[Wx2,Wy2] = Create_wait_time(200e-9,dt);
[Bxp3,Byp3] = Create_Gauss_Pulse(Bmax,pi()/2,g1,dt);
Bx=[Bxp1' Wx1' Bxp2' Wx2' -Bxp3']';
By=[Byp1' Wy1' Byp2' Wy2' -Byp3']';
%Bx=[Bxp1' Wx1' Bxp2' Wx2' Bxp3']'; %use for pi/2, pi, pi/2 pulse sequence
%By=[Byp1' Wy1' Byp2' Wy2' Byp3']'; %use for pi/2, pi, pi/2 pulse sequence

steps = length(Bx);
t=linspace(0, steps-1, steps)*dt;


%_____
%% Chirp pulse

Bmax=0.5e-3;    %microwave field in T
B1=Bmax;


[Bxp1,Byp1,phi_d] = Create_Chirp_Pulse(Bmax,pi()/2,g1,dt);
[Wx1,Wy1] = Create_wait_time(200e-9,dt);
[Bxp2,Byp2] = Create_Chirp_Pulse(Bmax,pi(),g1,dt);
[Wx2,Wy2] = Create_wait_time(200e-9,dt);
[Bxp3,Byp3] = Create_Chirp_Pulse(Bmax,pi()/2,g1,dt);
Bx =[Bxp1 Wx1' Bxp1 Bxp1 Wx2' -Bxp3]';
By =[Byp1 Wy1' Byp1 Byp1 Wy2' -Byp3]';
%Bx=[Bxp1' Wx1' Bxp2' Wx2' Bxp3']'; %use for pi/2, pi, pi/2 pulse sequence
%By=[Byp1' Wy1' Byp2' Wy2' Byp3']'; %use for pi/2, pi, pi/2 pulse sequence

steps = length(Bx);
t=linspace(0, steps-1, steps)*dt;

%%_____

%% Pauli matrices
Sx=[0,1; 1,0];      %sigma x
Sy=[0,-1i; 1i,0];   %sigma y
Sz=[1,0; 0,-1];     %sigma z
I=[1,0;0,1];

Sx1=kron(Sx,I);
Sy1=kron(Sy,I);
Sz1=kron(Sz,I);
Sx2=kron(I,Sx);
Sy2=kron(I,Sy);
Sz2=kron(I,Sz);

Sztot=kron(Sz,I)+kron(I,Sz);
Sxtot=kron(Sx,I)+kron(I,Sx);
Sytot=kron(Sy,I)+kron(I,Sy);
Sys.Z=kron(Sz,Sz);
Sys.X=kron(Sx,Sx);
Sys.Y=kron(Sy,Sy);
I4=eye(4);

%%_____
%% Recombination
```

```matlab
% Rs=1/10e-4;  %invers sec
% Rt=1/1e-6;


% Rs=1/10e-6;  %invers sec
% Rt=1/10e-8;


%%real parameters
Rs=1/8.5e-6;  %invers sec
Rt=1/25e-6;


% Singlet subspace
subspaceS=[0,0,0,0; ...
           0,1/2,-1/2,0; ...
           0,-1/2,1/2,0; ...
           0,0,0,0];


% Triplet subspace
subspaceT=[1,0,0,0; ...
           0,1/2,1/2,0; ...
           0,1/2,1/2,0; ...
           0,0,0,1];


Is=eye(4);
S=-Rs*subspaceS-Rt*subspaceT;

SSuper=kron(S,Is)+kron(Is,S);
SSuper=0;

%%_____
%% Relaxation



% T2e=200e-9;    %sec
% T1e=1000e-9;
% T2h=300e-9;
% T1h=1100e-9;


% T2e=800e-9;    %sec
% T1e=3000e-9;
% T2h=1100e-9;
% T1h=3000e-9;


 %%real parameters in second
T1e=8500e-9;      %sec
T1h=8500e-9;
T2e=800e-9;
T2h=1100e-9;


[RSuper,Re]=two_spins_RELAX(T1e,T2e,T1h,T2h);
RSuper=0;
%%_____
%% Loop over detuning

det_steps= 5;
 for j = [1:1:det_steps];
Bz1max=4e-3;
%Bz1 = (j-1)*Bz1max/(det_steps-1);
Bz1 = j*Bz1max/(det_steps-1);
```

```matlab
Bz1store(j)=Bz1;
% Bz2 =(j-1)*Bz1max/(det_steps-1);
Bz2 = 0*j*Bz1max/(det_steps-1);
Bz2store(j)=Bz2;
%% define Static Hamiltonian
Hzee=0.5*ub/hbar*(g1*Bz1*Sz1+g2*Bz2*Sz2);

%% Define initial state
M1=[0, 0, 1];
M2=[0, 0, 1];
[phi,theta,R]=cart2sph(M1(1),M1(2),M1(3));
[phi2,theta2,R2]=cart2sph(M2(1),M2(2),M2(3));
Th=-1*(theta-pi/2);
Th2=-1*(theta2-pi/2);
psi1=[cos(Th/2); exp(1i*phi)*sin(Th/2)];
psi2=[cos(Th2/2); exp(1i*phi2)*sin(Th2/2)];


PSI=kron(psi1, psi2);        %composite state |w>
rho0=PSI*PSI';               %4*4 density matrix rho


p0=vec2mat(rho0,1);          %16*1 Liouville density vector

%define equilibrium
p_eq=p0;
%define initial state
p_t=p0;

%observable
Mx1(1,:)=real(trace(ctranspose(vec2mat(Sx1,1))*p_t));
My1(1,:)=real(trace(ctranspose(vec2mat(Sy1,1))*p_t));
Mz1(1,:)=real(trace(ctranspose(vec2mat(Sz1,1))*p_t));
Mx2(1,:)=real(trace(ctranspose(vec2mat(Sx2,1))*p_t));
My2(1,:)=real(trace(ctranspose(vec2mat(Sy2,1))*p_t));
Mz2(1,:)=real(trace(ctranspose(vec2mat(Sz2,1))*p_t));


%% loop over time
h=waitbar(0, 'looping over t');
 for ii=1:length(t)

%define time dependant Hamiltonian
HRF=0.5*ub/hbar*(g1*(Bx(ii)*Sx1+By(ii)*Sy1)+g2*(Bx(ii)*Sx2+By(ii)*Sy2));
Htot=Hzee+HRF;    %4*4
Hsuper=kron(Htot,I4)-kron(I4,transpose(Htot));

Gs=1i*Hsuper+SSuper+RSuper;
Gss=1./Gs;
G=RSuper*hbar*1./Gs;
G(isnan(G))=0;               %replace all NaN with 0 assuming 0*a/0
p_ss=G*p_eq;                 % steady state

%% Evolve the density
%Evolve for H only
% L=-1i*Hsuper;
% Usuper=expm(L*dt);
% p_t=Usuper*p_t;

%Evolve for H and S
```

```matlab
% L=-1i*Hsuper+SSuper;
% Usuper=expm(L*dt);
% p_t=Usuper*p_t;

%Evolve for H,S and R
L=-1i*Hsuper+SSuper-RSuper;
p_t=p_ss+expm(L*dt)*(p_t-p_ss);

%% calculate observable
Mx1(ii,j)=real(trace(ctranspose(vec2mat(Sx1,1))*p_t));
My1(ii,j)=real(trace(ctranspose(vec2mat(Sy1,1))*p_t));
Mz1(ii,j)=real(trace(ctranspose(vec2mat(Sz1,1))*p_t));
Mx2(ii,j)=real(trace(ctranspose(vec2mat(Sx2,1))*p_t));
My2(ii,j)=real(trace(ctranspose(vec2mat(Sy2,1))*p_t));
Mz2(ii,j)=real(trace(ctranspose(vec2mat(Sz2,1))*p_t));


rho_normalization(ii)=p_t'*p_t;

waitbar(ii/length(t))
  end
close(h)

 end
```

Appendix B

Defining shape and adiabatic pulses

In this appendix, we present the definition for each pulse that has been used in the simulation in Appendix A. As demonstrated in ch5, the magnetic field component of the pulse along $\hat{x}$ and $\hat{y}$ can be written as:

$$B_1^x(t) = B_{1max}F_1(\tau)\cos[\Delta\phi(t)] \qquad\qquad (B.1)$$

$$B_1^y(t) = B_{1max}F_1(\tau)\sin[\Delta\phi(t)] \qquad\qquad (B.2)$$

where

$$\phi(t) = \phi_0 + 2\Pi \int_0^{T_p} f_{center} + f_{max}F_2(\tau)d\tau \qquad\qquad (B.3)$$

These equations with different modulation function F_1 and F_2 (shown in table 5.1)have been used to define the pulses.

B.1. Square pulse

```
function [Bx,By] = Create_theta_Pulse(B1,theta,g1,dt)

ub=9.274e-24;  %J/T
hbar= 1.0545718e-34; %J*s
s=2*pi()/(theta);
tau = 2*pi()*hbar/(s*g1*ub*B1); %4 for pi/2
steps = round(tau/dt);

Bx=1*ones(steps, 1)*B1;    %T
By=0*ones(steps, 1)*B1;    %T
end
```

B.2. Gaussian pulse

```
function [Bx,By] = Create_Gauss_Pulse(B1,theta,g1,dt)

ub=9.274e-24;  %J/T
hbar= 1.0545718e-34;
cut = 10;
FWHM=28e-9*theta*0.505e-3/(B1*pi()); %ns
sigma = FWHM/(2*dt);
length=sigma*cut;
steps = round(length);
x = 0:1:steps-1;

Bx = B1*(gaussmf(x,[sigma, steps/2])'); %B1*F1(t)
By=0*ones(steps, 1)*B1;
end
```

B.3. Chirp pulse

```
function [Bx,By,phi_1] = Create_Chirp_Pulse(B1,theta,g1,dt)

ub=9.274e-24;    %J/T
hbar= 1.0545718e-34;  %J*s
sweep=400e6;          %frequency sweep in MHz
length=540*theta/pi();
steps = round(length);
t=linspace(0, steps-1, steps)*dt;
phi_1=2*pi*sweep*((t.*t/t(end))-t);

Bx=B1*ones(1,steps).*cos(phi_1);
By=B1*ones(1,steps).*sin(phi_1);

end
```

B.4. Waiting time between pi and pi/2 pulses

After defining the pulses, Hanh echo sequence is used as a spin detection method. As we simulated conventional Hahn-echo sequences as $[\pi/2 : \tau^{200\text{ns}} : \pi: \tau^{200\text{ns}} : \pi/2]$
we define the waiting time to be same for all pulses.

```
function [Bx,By] = Create_wait_time(wait,dt)

steps = round(wait/dt);

Bx=0*ones(steps, 1);    %T
By=0*ones(steps, 1);    %T

End
```

Appendix C

Determine Spin relaxation matrix

We used Redfield theory to define spin relaxation matrix as a set of 4x4 matrix.

The Redfield matrix for one spin (electron) with coefficients is:

$$\hat{R}_e = \begin{bmatrix} \frac{1}{T_{1e}} & 0 & 0 & -\frac{1}{T_{1e}} \\ 0 & \frac{1}{T_{2e}} & -\frac{1}{T_{2e}} & 0 \\ 0 & -\frac{1}{T_{2e}} & \frac{1}{T_{2e}} & 0 \\ -\frac{1}{T_{1e}} & 0 & 0 & \frac{1}{T_{1e}} \end{bmatrix} \tag{C.1}$$

Then it has been transformed to superoperator by unitary operator

$$\hat{U}_e = \begin{bmatrix} 1\,1\,1\,1 \\ 1\,1\,1\,1 \\ 1\,1\,1\,1 \\ 1\,1\,1\,1 \end{bmatrix} \tag{C.2}$$

```
function [ Rij_t,Re]=two_spins_RELAX(T1e,T2e,T1h,T2h)

Re(1,1)=1/T1e;
Re(2,2)=1/T2e;
Re(3,3)=1/T2e;
Re(4,4)=1/T1e;

Re(1,2)=0;
Re(2,1)=0;
Re(1,3)=0;
Re(3,1)=0;
Re(3,4)=0;
Re(2,4)=0;
Re(4,2)=0;
Re(4,3)=0;
Re(1,4)=-1/T1e;
Re(4,1)=-1/T1e;
Re(2,3)=real(-1/T2e);
Re(3,2)=real(-1/T2e);

Rh(1,1)=1/T1h;
Rh(2,2)=1/T2h;
Rh(3,3)=1/T2h;
Rh(4,4)=1/T1h;

Rh(1,2)=0;
Rh(2,1)=0;
Rh(1,3)=0;
Rh(3,1)=0;
Rh(3,4)=0;
Rh(2,4)=0;
Rh(4,2)=0;
Rh(4,3)=0;
Rh(1,4)=-1/T1h;
Rh(4,1)=-1/T1h;
Rh(2,3)=real(-1/T2h);
```

```matlab
Rh(3,2)=real(-1/T2h);


Ue=[1,1,1,1;...          %Unitary matrix for spin 1
    1,1,1,1;...
    1,1,1,1;...
    1,1,1,1];

Uh=[1,1,1,1;...          %Unitary matrix for spin 2
    1,1,1,1;...
    1,1,1,1;...
    1,1,1,1];

Rij_t=kron(Rh,Ue)+kron(Uh,Re);

 End
```

Appendix D

Calculating the fidelity

The fidelity of a single spin operation on the entire ensemble of spins and for operation on operation on an ensemble of pairs of spins has been calculated in this simulation.

```
calculate the fidelity
%%real data
deltaB1=2.06e-3;    %T
deltaB2=4.14e-3;    %T

%%assumption values used for deltaB1
%deltaB1=2.06e-4;    %T
%deltaB1=0.1e-3;    %T

%%use for fidelity of a single spin operation on the entire ensemble of
spins and ignore the loop
y = normpdf(Bz1store,0,deltaB1);
Mz1weighted=-1/2*(Mz1-1).*y*Bz1max/(det_steps-1);  %Fz(Bz1)*G(Bz1)
perfect = -1*ones(length(t),length(Bz1store));
perfectweighted=-perfect.*y*Bz1max/(det_steps-1);  %G(Bz1)for deltaB1
perfectfidelity = sum(perfectweighted(length(t),:))*2 -
perfectweighted(length(t),1); %2 for the half gaussian
fidelity = sum(Mz1weighted(length(t),:))/sum(perfectweighted(length(t),:));


%%use the loop for fidelity for operation on operation on an ensemble of
pairs of spins
  i=0;
  FIDELITY=zeros(40,40);
  for deltaB1 = [0:0.5e-4:deltaB1]
     i=i+1;
     k=0;
     for deltaB1 = [0:0.5e-4:deltaB2]
          k=k+1;

 %%for spin 1
y = normpdf(Bz1store,0,deltaB1);
Mz1weighted=-1/2*(Mz1-1).*y*Bz1max/(det_steps-1);  %Fz(Bz1)*G(Bz1)
perfect = -1*ones(length(t),length(Bz1store));
perfectweighted=-perfect.*y*Bz1max/(det_steps-1);  %G(Bz1)for deltaB1
perfectfidelity = sum(perfectweighted(length(t),:))*2 -
perfectweighted(length(t),1);%2 for the half gaussian
fidelity = sum(Mz1weighted(length(t),:))/sum(perfectweighted(length(t),:));

 %%for spin 2
y2 = normpdf(Bz2store,0,deltaB2);
Mz2weighted2=-1/2*(Mz2-1).*y2*Bz1max/(det_steps-1);   %Fz(Bz2)*G(Bz2)
perfect2 = -1*ones(length(t),length(Bz2store));
perfectweighted2=-perfect2.*y2*Bz1max/(det_steps-1);%G(Bz2)for deltaB2
perfectfidelity2 = sum(perfectweighted2(length(t),:))*2 -
perfectweighted2(length(t),1);%2 for the half gaussian
fidelity2 =
sum(Mz2weighted2(length(t),:))/sum(perfectweighted2(length(t),:));
```

```matlab
 %%for two spins
FID=Mz1weighted(length(t),:);
FID2=Mz2weighted2(length(t),:);
a=FID'*FID2;
b=perfectweighted(length(t),:)'*perfectweighted2(length(t),:);
FIDELITY(i,k)=sum(sum(FID'*FID2))/(sum(sum(b)));
end
end
FIDELITY(end)
```

References:

[1] R. Geng, T. T. Daugherty, K. Do, H. M. Luong, & T. D. Nguyen, "A review on organic spintronic materials and devices: I. Magnetic field effect on organic light emitting diodes", Journal of Science: Advanced Materials and Devices, 1(2), 128-140, (2016).

[2] V. Shrotriya, "Polymer power", Nature Photonics, 3, 447. doi:10.1038/nphoton.2009.130, (2009).

[3] L. Meng, Y. Zhang, X. Wan, C. Li, X. Zhang, Y. Wang, & H. L. Yip, "Organic and solution-processed tandem solar cells with 17.3% efficiency", Science, 361(6407), 1094-1098, (2018).

[4] C. Boehme, D. R. McCamey, "6 Investigating Spin-Dependent Processes in Organic Semiconductors", Organic Spintronics, 257 (2010).

[5] T. L. Keevers, "Spin Dynamics in Organic Optoelectronic Devices", Diss., University of New South Wales (2016).

[6] F. Dimroth, T. N. Tibbits, M. Niemeyer, F. Predan, P. Beutel, C. Karcher, & A. W. Bett, "Four-junction wafer-bonded concentrator solar cells", IEEE Journal of Photovoltaics, 6(1), 343-349, (2015).

[7] M. Jørgensen, K. Norrman, & F. Krebs, "Stability/degradation of polymer solar cells", Solar Energy Materials and Solar Cells, 92(7), 686-714, (2008).

[8] S. Savagatrup, A. D. Printz, T. F. O'Connor, A. V. Zaretski, D. Rodriquez, E. J. Sawyer, & D. J. Lipomi, "Mechanical degradation and stability of organic solar cells: molecular and microstructural determinants", Energy & Environmental Science, 8(1), 55-80, (2015).

[9] C. Boehme, & J. M. Lupton, "Challenges for organic spintronics", Nature Nanotechnology, 8(9), 612, (2013).

[10] V. Dediu, M. Murgia, F. C. Matacotta, C. Taliani, & S. Barbanera, "Room temperature spin polarized injection in organic semiconductor", Solid State Communications, *122*(3-4), 181-184, (2002).

[11] W. J. Baker, T. L. Keevers, J. M. Lupton, D. R. McCamey, & C. Boehme, "Slow Hopping and Spin Dephasing of Coulombically Bound Polaron Pairs in an Organic Semiconductor at Room Temperature", Physical Review Letters, 108, 267601, (2012).

[12] S. M. McMurry, "Quantum Mechanics", Oxford, University of Dublin (1994)

[13] R. Fisher, "Optimal control of multi-level quantum systems", Diss. Technische Universität München, (2010).

[14] C. Arenz, G. Gualdi, & D. Burgarth, "Control of open quantum systems: case study of the central spin model", New Journal of Physics, 16(6), 065023 (2014).

[15] D. R. McCamey, H. A. Seipel, S.-Y. Paik, M. J. Walter, N. J. Borys, J. M. Lupton and C. Boehme, "Spin Rabi flopping in the photocurrent of a polymer light-emitting diode", Nature Materials 7, 723 - 728 (2008).

[16] W. J. Baker, K. Ambal, D. P. Waters, R. Baarda, H. Morishita, K. van Schooten, D. R. McCamey, J. M. Lupton, and C. Boehme, "Robust absolute magnetometry with organic thin-film devices", Nature Communications 3, 898 (2012).

[17] A. Doll, "Frequency-Swept Microwave Pulses for Electron Spin Resonance", Diss. ETH Zurich (2016).

[18] B. M. Weckhuysen, R. Heidler, and R. A. Schoonheydt, "Electron spin resonance spectroscopy", In Characterization I, pp. 295-335, Springer, Berlin, Heidelberg, (2004).

[19] J.R. Maze, P.L. Stanwix, J.S. Hodges, S. Hong, J.M. Taylor, P. Cappellaro, L. Jiang, M.G. Dutt, E. Togan, A.S. Zibrov, and A. Yacoby, "Nanoscale magnetic sensing with an individual electronic spin in diamond", Nature 455, 644-647 (2008).

[20] J. A. Weil, J. R. Bolton, "Electron paramagnetic resonance: elementary theory and practical applications", John Wiley & Sons (2007).

[21] A. Abragam, B. Bleaney, "Electron paramagnetic resonance of transition ions", OUP Oxford (2012).

[22] J.Brossel, S. Geschwind, & A.L. Schawlow, "Optical detection of paramagnetic resonance in crystals at low temperatures", Physical Review Letters, 3(12), 548, (1959).

[23] S. Geschwind, R. J. Collins, & A. L. Schawlow, "Optical detection of paramagnetic resonance in an excited state of Cr 3+ in Al 2 O 3", Physical Review Letters, 3(12), 545 (1959).

[24] M. Guéron, & I. Solomon, "Effect of spin resonance on hot electrons by spin-orbit coupling in n-type InSb", Physical Review Letters, 15(16), 667, (1965).

[25] R. Maxwell, & A. Honig, "Neutral-impurity scattering experiments in silicon with highly spin-polarized electrons", Physical Review Letters, 17(4), 188, (1966).

[26] C. Boehme, H. Malissa, "Electrically Detected Magnetic Resonance Spectroscopy", eMagRes, 83-100.13 (2017).

[27] J. Orenstein, Z. Vardeny, G. L. Baker, G. Eagle, & S. Etemad, "Mechanism for photogeneration of charge carriers in polyacetylene", Physical Review B, 30(2), 786 (1984).

[28] D. R. McCamey, G. W. Morley, H. A. Seipel, L. C. Brunel, J. van Tol, & C. Boehme, "Spin-dependent processes at the crystalline Si-SiO 2 interface at high magnetic fields", Physical Review B, 78(4), 045303 (2008).

[29] Z. V. Vardeny, & X. Wei, "On the Excitonic Nature of the Photoluminescence in Polythiophene Revealed by ODMR Spectroscopy", Molecular Crystals and Liquid Crystals, 256(1), 465-472 (1994).

[30] M. Wohlgenannt, K. Tandon, S. Mazumdar, S. Ramasesha, & Z. V. Vardeny, "Formation cross-sections of singlet and triplet excitons in π-conjugated polymers", Nature, 409(6819), 494 (2001).

[31] M. Reufer, M. Walter, P. Lagoudakis, A. Hummel, J. Kolb, H. Roskos, J. Lupton, "Spin-conserving carrier recombination in conjugated polymers", Nature Materials, 4(4), 340-346 (2005).

[32] M. Segal, M. A. Baldo, R. J. Holmes, S. R. Forrest, & Z. G. Soos, "Excitonic singlet-triplet ratios in molecular and polymeric organic materials", Physical Review B, 075211 (2003).

[33] F. Verstraete, V. Murg, &J. I. Cirac, "Matrix product states, projected entangled pair states, and variational renormalization group methods for quantum spin systems", *Advances in Physics*, *57*(2), 143-224 (2008).

[34] A. J. Daley, C. Kollath, U. Schollwöck, & G. Vidal, "Time-dependent density-matrix renormalization-group using adaptive effective Hilbert spaces", Journal of Statistical Mechanics: Theory and Experiment, P04005, 04(2004).

[35] N. Wagner-Rundell, "Electron spin relaxation effects on radical recombination reactions in weak magnetic fields", Diss. University of Oxford (2008).

[36] J. Keeler, "Understanding NMR Spectroscopy" (2004).

[37] C. Boehme, K. Lips, "Theory of Time-Domain Measurement Of Spin-Dependent Recombination With Pulsed Electrically Detected Magnetic Resonance", Physical Review B 68.24 (2003).

[38] P. N. Argyres, P. L. Kelley, "Theory of Spin Resonance and Relaxation", Physical Review 134.1A, A98-A111 (1964).

[39] A. Isar, A. Sandulescu, H. Scutaru, E. Stefanescu, W. Scheid,"Open quantum systems", International Journal of Modern Physics E, 3.02, 635-714 (1994).

[40] H. Weimer, "Quantum many-body physics with strongly interacting Rydberg atoms" Verlag Dr. Hut (2010).

[41] D. M. Murphy, "EPR (Electron Paramagnetic Resonance) spectroscopy of polycrystalline oxide systems", Metal Oxide Catalysis (2008): 1-50.

[42] J. A. Guse, "Developing microwave probes for investigating opto-electronic processes in photovoltaic materials", Diss., University of New South Wales (2018).

[43] M. Garwood and L. DelaBarre, "The return of the frequency sweep: designing adiabatic pulses for contemporary NMR", *Journal of Magnetic Resonance* **153,**155-177 (2001).

[44] F. M. Hrubesch, G. Braunbeck, A. Voss, M. Stutzmann, M.S. Brandt, "Broadband electrically detected magnetic resonance using adiabatic pulses", *Journal of Magnetic Resonance* **254,** 62–69 (2015).

[45] E. Kupce, R. Freeman, "Adiabatic pulses for wideband inversion and broadband decoupling" Journal of Magnetic Resonance, Series A 115.2, 273-276 (1995).

[46] A. Tannús M. Garwood, "Adiabatic pulses", NMR in Biomedicine, 10.8, 423-434 (1997).

[47] U. E. Steiner, and T Ulrich, "Magnetic field effects in chemical kinetics and related phenomena." *Chemical Reviews* 89, no. 1 (1989): 51-147.

[48] K. L. Purvis, S. P. Wiemelt, T. Maras, M. Blue, V. Melkonian, P. D. Ashby & A. M. Nishimura, "Spin-echo in the phosphorescent triplet state of crystalline 2-indanone", Journal of luminescence, 71(3), 199-205, (1997).

[49] V. Weis, K. Möbius, & T. Prisner, "Optically detected electron spin echo envelope modulation on a photoexcited triplet state in zero magnetic field—A comparison between the zero-field and high-field limits", Journal of Magnetic Resonance, 131(1), 17-24, (1998).

[50] D. J. Lepine, "Spin-dependent recombination on silicon surface", Physical Review B, 6(2), 436, (1972).

[51] T. Eickelkamp, S. Roth, & M. Mehring, "Electrically detected magnetic resonance in photoexcited fullerenes", Molecular Physics, 95(5), 967-972, (1998).

[52] I. Hiromitsu, Y. Kaimori, & T. Ito, "Photovoltaic effect and electrically detected electron spin resonance of a H2-phthalocyanine/C60 heterojunction", Solid state communications, 104(9), 511-515, (1997).

[53] P. Kanschat, K. Lips, & W. Fuhs, W., "Identification of non-radiative recombination paths in microcrystalline silicon"" (μc-Si: H). *Journal of non-crystalline solids*, *266*, 524-528, (2000).

[54] M. Stutzmann, M. S. Brandt, & M. W. Bayerl, "Spin-dependent processes in amorphous and microcrystalline silicon: a survey". Journal of non-crystalline solids, 266, 1-22, (2000).

[55] K. Lips, & W. Fuhs, "Transport and recombination in amorphous p-i-n-type solar cells studied by electrically detected magnetic resonance", Journal of applied physics, 74(6), 3993-3999, (1993).

[56] R. Müller, P. Kanschat, S. Von Aichberger, K. Lips, & W. Fuhs, "Identification of transport and recombination paths in homo-and heterojunction silicon solar cells by electrically detected magnetic resonance", Journal of Non-Crystalline Solids, 266, 1124-1128, (2000).

[57] C. Bohme, "Dynamics of spin-dependent charge carrier recombination", (2002).

[58] C. Boehme, & K. Lips, K.," Electrical detection of spin coherence in silicon", Physical review letters, 91(24), 246603, (2003).

[59] I. Hiromitsu, Y. Kaimori, M. Kitano, & T. Ito, "Spin-dependent recombination of photoinduced carriers in phthalocyanine/C 60 heterojunctions", Physical Review B, 59(3), 2151, (1999).

[60] C. Boehme, & K. Lips," Investigation of electronic transitions in semiconductors with pulsed electrically detected magnetic resonance". *Applied Magnetic Resonance*, *27*(1-2), 109(2004).

[61] C. Boehme, & K. Lips, "Time domain measurement of spin-dependent recombination". Applied Physics Letters, 79(26), 4363-4365, (2001).

[62] M. Dobers, K. V. Klitzing, J. Schneider, G. Weimann, & K. Ploog, "Electrical Detection of Nuclear Magnetic Resonance in GaAs− Al x Ga 1− x As Heterostructures", Physical review letters, 61(14), 1650, (1988).

[63] A. Honig," Neutral-impurity scattering and impurity zeeman spectroscopy in semiconductors using highly spin-polarized carriers", Physical Review Letters, 17(4), 186, (1966).

[64] D. Sun,K. J. Van Schooten, M. Kavand, H. Malissa, C. Zhang, M. Groesbeck & Z. V. Vardeny, "Inverse spin Hall effect from pulsed spin current in organic semiconductors with tunable spin–orbit coupling", Nature materials, 15(8), 863, (2016).

[65] K. Ando, S. Takahashi, J. Ieda, H. Kurebayashi, T. Trypiniotis, C. H. W. Barnes, ... & E. Saitoh, "Electrically tunable spin injector free from the impedance mismatch problem", Nature materials, 10(9), 655, (2011).

[66] K. Ando, S. Watanabe, S. Mooser, E. Saitoh, & H. Sirringhaus, "Solution-processed organic spin–charge converter", Nature materials, 12(7), 622, (2013).

[67] W. J. Baker, D. R. McCamey, K. J. Van Schooten, J. M. Lupton, & C. Boehme, "Differentiation between polaron-pair and triplet-exciton polaron spin-dependent mechanisms in organic light-emitting diodes by coherent spin beating", Physical Review B, 84(16), 165205, (2011).

[68] T. L. Keevers, & D. R. McCamey, "Role of incoherent dynamics in determining the electrical response of exciton-polaron complexes in pulsed magnetic resonance", Physical Review B, 91(24), 245208, (2015).

[69] T. L. Keevers, W. J. Baker, & D. R. McCamey, " Theory of exciton-polaron complexes in pulsed electrically detected magnetic resonance", Physical Review B, 91(20), 205206, (2015).

[70] E. Saitoh, M. Ueda, H. Miyajima, & G. Tatara, "Conversion of spin current into charge current at room temperature: Inverse spin-Hall effect", Applied physics letters, 88(18), 182509, (2006).

[71] S. Watanabe, K. Ando, K. Kang, S. Mooser, Y. Vaynzof, H. Kurebayashi, ... & H. Sirringhaus, "Polaron spin current transport in organic semiconductors". Nature Physics, 10(4), 308, (2014).

[72] M.A. Anders, P. M. Lenahan,C. J. Cochrane, & A. J. Lelis, " Relationship between the 4H-SiC/SiO 2 interface structure and electronic properties explored by electrically detected magnetic resonance", IEEE Transactions on Electron Devices, 62(2), 301-308, (2015).

[73] C. J. Cochrane, & P. M. Lenahan, "Spin counting in electrically detected magnetic resonance via low-field defect state mixing", Applied Physics Letters, 104(9), 093503, (2014).

[74] J. Shinar, "Optically detected magnetic resonance studies of luminescence-quenching processes in π-conjugated materials and organic light-emitting devices", Laser & Photonics Reviews, 6(6), 767-786, (2012).

[75] G. B. Silva, L. F. Santos, R. M. Faria, & C. F. O. Graeff, "Edmr of Meh-Ppv LEDs", Physica B: Condensed Matter, 308, 1078-1080, (2001).

[76] S. Y. Lee, S. Paik, D. R. McCamey, & C. Boehme, "Modulation frequency dependence of continuous-wave optically/electrically detected magnetic resonance", Physical Review B, 86(11), 115204, (2012).

[77] K. J. Van Schooten, D. L. Baird, M. E. Limes, J. M. Lupton, & C. Boehme, "Probing long-range carrier-pair spin–spin interactions in a conjugated polymer by detuning of electrically detected spin beating", Nature communications, 6, 6688, (2015).

[78] D. P. Waters, G. Joshi, M. Kavand, M. E. Limes, H. Malissa, P. L. Burn, ... & C. Boehme, "The spin-Dicke effect in OLED magnetoresistance". Nature Physics, 11(11), 910, (2015).

[79] G. Joshi, R. Miller, L. Ogden, M. Kavand, S. Jamali, K. Ambal, ... & C. Boehme, "Separating hyperfine from spin-orbit interactions in organic semiconductors by multi-octave magnetic resonance using coplanar waveguide microresonators", Applied Physics Letters, 109(10), 103303, (2016).

[80] M. Xiao, I. Martin, E. Yablonovitch, & H. W. Jiang, "Electrical detection of the spin resonance of a single electron in a silicon field-effect transistor", Nature, 430(6998), 435, (2004).

[81] C. Boehme, & K. Lips, "The ultra-sensitive electrical detection of spin-Rabi oscillation at paramagnetic defects", Physica B: Condensed Matter, 376, 930-935, (2006).

[82] W. J. Baker, "Coherently controlled spin-dependent charge carrier transitions in organic semiconductors: properties and applications", Dissertation, Utah, USA: Department of Physics and Astronomy of the University of Utah, (2012).

[83] L. Dreher, F. Hoehne, H. Morishita, H. Huebl, M. Stutzmann, K. M. Itoh, & M. S. Brandt, "Pulsed low-field electrically detected magnetic resonance", Physical Review B, 91(7), 075314, (2015).

[84] F. Hoehne, L. Dreher, J. Behrends, M. Fehr, H. Huebl, K. Lips, ... & M. S. Brandt, "Lock-in detection for pulsed electrically detected magnetic resonance", Review of Scientific Instruments, 83(4), 043907, (2012).

[85] I. Katz, M. Fehr, A. Schnegg, K. Lips, & A. Blank, "High resolution in-operando microimaging of solar cells with pulsed electrically-detected magnetic resonance", Journal of Magnetic Resonance, 251, 26-35, (2015).

[86] J. R. Kirtley, "Fundamental studies of superconductors using scanning magnetic imaging", Reports on Progress in Physics, 126501 (2010).

[87] D. Budker, & M. Romalis, "Optical magnetometry", Nature Physics, 227–234 (2007).

[88] S. Heinze, M. Bode, A. Kubetzka, O. Pietzsch, X. Nie, S. Blügel, & W. R., "Real-Space Imaging of Two-Dimensional Antiferromagnetism on the Atomic Scale", Science, 1805-1808 (2000).

[89] J. M. Taylor, P. Cappellaro, L. Childress, L. Jiang, D. Budker, P. R. Hemmer, A. Yacoby, R. Walsworth, and M. D. Lukin, "High-sensitivity diamond magnetometer with nanoscale resolution", *Nature Physics* **4,** 810-816 (2008).

[90] S. Meiboom, & D. Gill, "Modified spin-echo method for measuring nuclear relaxation times", Review of Scientific Instruments, 688 (1958).

[91] T. Wolf, P. Neumann, K. Nakamura, H. Sumiya, T. Ohshima, J. Isoya & W. J., "Subpicotesla Diamond Magnetometry", Physical Review X, 041001 (2015).

[92] G. Chatzidrosos, A. Wickenbrock, L. Bougas, N. Leefer, T. Wu, K. Jensen, D. Budker, "Miniature Cavity-Enhanced Diamond Magnetometer", Physical Review Applied, 044019 (2017).

[93] J. Schloss, J. Barry, M. Turner, & R. Walsworth, "Simultaneous Broadband Vector Magnetometry Using Solid-State Spins", Physical Review Applied, 034044 (2018).

[94] J. Burroughes, D. Bradley, A. Brown, R. Marks, K. Mackay, R.Friend, A. Holmes, "Lightemitting-diodes based on conju-gated polymers", Nature, 539-541 (1990).

[95] B. W. D'Andrade, & S. R. Forrest, "White organic light-emitting devices for solid-state lighting", Advanced Materials, 1585-1595 (2004).

[96] A. Heeger, "25th anniversary article: bulk heterojunction solar cells: understanding the mechanism of operation", Advanced Materials, 10-28 (2014).

[97] C. Tang, "Two-layer organic photovoltaic cell", Applied Physics Letters, 183 (1986).

[98] C. Dimitrakopoulos, & P. Malenfant, "Organic thin film transistors for large area electronics", Advanced Materials, 99-117 (2002).

[99] A. Tsumura, H. Koezuka, & T. Ando, "Macromolecular electronic device: field-effect transistor with a polythiophene thin film", Applied Physics Letters, 1210-1212 (1986).

[100] J. Kalinowski, J. Szmytkowski, & W. Stampor, "Magnetic hyperfine modulation of charge photogeneration in solid films of Alq 3", Chemical Physics Letters, 380-387 (2003).

[101] O. Mermer, G. Veeraraghavan, T. Francis, & M. Wohlgenannt, "Large magneto-resistance at room-temperature in small-molecular weight organic semi-conductor sandwich devices", Solid State Communications, 631-636 (2005).

[102] P. A. Bobbert, T. D. Nguyen, F. W. A. Van Oost, van B. Koopmans, and M. Wohlgenannt. "Bipolaron mechanism for organic magnetoresistance." *Physical Review Letters* 99, no. 21 (2007): 216801.

[103] N. Harmon, & M. Flatte, "Spin-flip induced magnetoresistance in positionally disordered organic solids", Physical Review Letters, 186602-186605 (2012).

[104] R. Mahato, H. Lülf, M. Siekman, S. Kersten, P. Bobbert, M. de Jong, W. van der Wiel, "Ultrahigh magnetoresistance at room tem-perature in molecular wires", Science, 257-260 (2013).

[105] T. Nguyen, B. Gautam, E. Ehrenfreund, & Z. Vardeny, "Magneto-conductance response in unipolar and bipolar organic diodes at ultrasmall fields", Physical Review Letters, 166804 (2010).

[106] V. Prigodin, J. Bergeson, D. Lincoln, & A. Epstein, "Anomalous room temperature magnetoresistance in organic semiconductors", Synthetic Metals, 757-761 (2006).

[107] P. Desai, P. Shakya, T. Kreouzis, W. Gillin, N. Morley, & M. Gibbs, "Magnetoresistance and efficiency measurements of Alq3-based OLEDs", Physical Review B, 094423 (2007).

[108] B. Hu, & Y. Wu, "Tuning magnetoresistance between positive and negative values in organic semiconductors", Nature Materials, 985-991 (2007).

[109] A. H. Devir-Wolfman, B. Khachatryan, B. R. Gautam, L. Tzabary, A. Keren, N. Tessler, Z. V. Vardeny, E. Ehrenfreund, "Short-lived charge-transfer excitons in organic photovoltaic cells studied by highfield magneto-photocurrent", Nature Communications, 4529 (2014).

[110] F. Wang, H. Bassler & Z. Vardeny, "Magnetic field effects in p-conjugated polymer-fullerene blends: evidence for multiple components", Physical Review Letters, 236805 (2008).

[111] J. Li, N. Sun, Z. X. Guo, C. Li, Y. Li, L. Dai, L. Fan, "Photovoltaic Devices with Methanofullerenes as Electron Acceptors", Journal of Physical Chemistry B, 11509-11514 (2002).

[112] F. Macià, F. Wang, N. Harmon, A. Kent, M. Wohlgenannt, & M. Flatté, "Organic magnetoelectroluminescence for room temperature transduction between magnetic and optical information", Nature Communications, 3609 (2014).

[113] N. Sariciftci, D. Braun, C. Zhang, V. Srdanov, A. Heeger, G. Stucky, & F. Wudl, "Semiconducting polymer-buckminsterfullerene heterojunctions: Diodes, photodiodes, and photovoltaic cells", Applies Physics Letters, 585-587 (1993).

[114] H. Malissa, R. Miller, D. Baird, S. Jamali, G. Joshi, M. Bursch, C. Boehme, "Revealing weak spin-orbit coupling effects on charge carriers in a π-conjugated polymer", Physical Review B, 161201 (2018).

[115] D. Waters, G. Joshi, M. Kavand, M. Limes, H. Malissa, P. Burn, C. Boehme, "Nature Physics Letters", 910-914 (2015).

[116] M.Cai, "Organic Light-Emitting Diodes (OLEDs) and Optically-Detected Magnetic Resonance (ODMR) studies on organic materials", (2011).

[117] J.Cornil, D. Beljonne, J.P. Calbert, J.L. Brédas. "Interchain interactions in organic π-conjugated materials: impact on electronic structure, optical response, and charge transport", Advanced materials, 13.14, 1053-1067 (2001).

[118] S.L. Hung, C. H. Chen,"Recent progress of molecular organic electroluminescent materials and devices", Materials Science and Engineering: R: Reports 39.5, 143-222 (2002).

[119] R. H. Friend, R.W. Gymer, A.B.Holmes, J.H. Burroughes, R.N. Marks, C.D.D.C. Taliani, D.D.C. Bradley, D.A. Dos Santos, J.L. Bredas, M. Lögdlund, W.R. Salaneck,"Electroluminescence in conjugated polymers", Nature 397.6715,121-128 (1999).

[120] S. Suppiah, M. Mohamad Shahimin, and N. Juhari, "Fabrication of MEH-PPV based organic light emitting diode and transistor", Micro and Nanoelectronics (RSM), 2011 IEEE Regional Symposium on, IEEE, (2011).

[121] H. A. Méndez-Pinzón, D. R. Pardo-Pardo, J. P. Cuéllar-Alvarado, J. C. Salcedo-Reyes, R. Vera, and B. Páez-Sierra, "Analysis of the Current-Voltage Characteristics of Polymer-Based Organic Light-Emitting Diodes (OLEDs) Deposited by Spin Coating", Universitas Scientiarum, Vol. 15, no. 1, Jan. pp. 68-76, doi:10.11144/javeriana.SC15-1.aotc (2010).

[122] A. Sperlich, "Electron paramagnetic resonance spectroscopy of conjugated polymers and fullerenes for organic photovoltaics", (2013).

[123] M. H. Suhail, et al. "ITO/PEDOT: PSS/MEH: PPV/Alq3/LiF/Au as a schottky diode." International Journal of Application or Innovation in Engineering & Management 2.1: 130-136 (2013).

[124] J. M. Lupton, D. R. McCamey and C. Boehme, "Coherent spin manipulation in molecular semiconductors: getting a handle on organic spintronics", *ChemPhysChem* **11,** 3040-3058 (2010).

[125] D.R. McCamey, S. Y. Lee, S. Y. Paik, J. M. Lupton, & C. Boehme, "Spin-dependent dynamics of polaron pairs in organic semiconductors", Physical Review B, 82(12), 125206 (2010).

[126] Z. Lei-Ming, D. Yang, & S. Fang-Wen, "Magnetic Field Measurement with Heisenberg Limit Based on Solid Spin NOON State", Chinese Physics Letters, 067601 (2015).

[127] I. Kominis, T. Kornack, J. C. Allred, & M. Romalis, "A subfemtotesla multichannel atomic magnetometer", Nature, 596-599 (2003).

[128] Y.L. Zhang, H. Wang, L. Jing, L. Z. Mu, &H. Fan, "Fitting magnetic field gradient with Heisenberg-scaling accuracy", Scientific Reports, 7390 (2014).

[129] F. Albarelli, M. Rossi, M Paris, & M. Genoni, "Ultimate limits for quantum magnetometry via time-continuous", New Journal of Physics, 123011 (2017).

[130] J. Geremia, J. Stockton, A.Doherty, & H. Mabuchi,"Quantum Kalman Filtering and the Heisenberg Limit in Atomic Magnetometry", Physical Review Letters, 250801 (2003).

[131] H. Hübl, "Coherent manipulation and electrical detection of phosphorus donor spins in silicon", Diss. Technische Universität München, Garching: Walter Schottky Institut, Technische Universität München (2007).

[132] M. Knupfer, "Exciton binding energies in organic semiconductors", Applied Physics A, 77, 623–626 (2003).

[133] G. W. Morley, D. R. McCamey, H. A. Seipel, L. C. Brunel, J. van Tol, & C. Boehme, "Long-Lived Spin Coherence in Silicon with an Electrical Spin Trap Readout", Physical Review Letters, 101(20), 207602 (2008).

[134] D. R. McCamey, K.J. Van Schooten, W.J. Baker, S. Y. Lee, S. Y. Paik, J. M. Lupton & C. Boehme, "Hyperfine-field-mediated spin beating in electrostatically bound charge carrier pairs", Physical review letters, 104(1), 017601 (2010).